

UNIVERSITY OF OKLAHOMA

GRADUATE COLLEGE

ELECTRON PROBE MICRO-ANALYSIS OF THE WOODFORD SHALE,
SOUTH CENTRAL OKLAHOMA

A THESIS

SUBMITTED TO THE GRADUATE FACULTY

in partial fulfillment of the requirements for the

Degree of

MASTER OF SCIENCE

By

MATTHEW W. TOTTEN JR.

Norman, Oklahoma

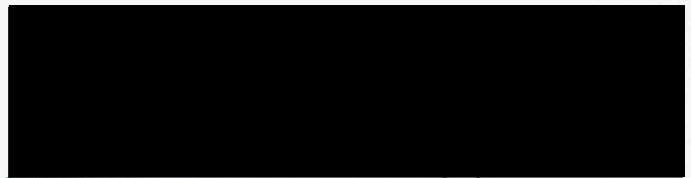
2011

00
THESIS
TOT
cop.2

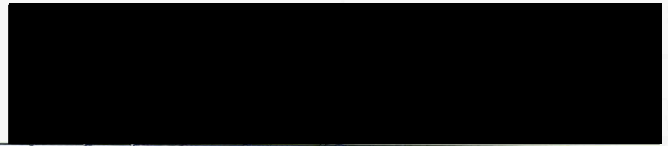
ELECTRON PROBE MICRO-ANALYSIS OF THE WOODFORD SHALE,
SOUTH CENTRAL OKLAHOMA

A THESIS APPROVED FOR THE
CONOCOPHILLIPS SCHOOL OF GEOLOGY AND GEOPHYSICS

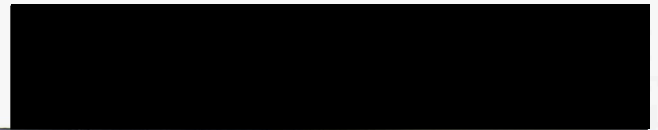
BY



Dr. Roger M. Slatt, Chair ✓



Dr. George Morgan ✓



Dr. R. Douglas Elmore

ACKNOWLEDGEMENTS

The author wishes to thank the following individuals for their assistance and support in the completion of this project. The author is indebted to the following individuals for their assistance and support in the completion of this project. The author is indebted to the following individuals for their assistance and support in the completion of this project.

The author wishes to thank the following individuals for their assistance and support in the completion of this project. The author is indebted to the following individuals for their assistance and support in the completion of this project. The author is indebted to the following individuals for their assistance and support in the completion of this project.

Special thanks go to Dr. George Mason for his valuable reading and helping me in writing the abstract manuscript as the main instrument of investigating for this work. His support, patience, and assistance over the course of this research has been invaluable, and it has been a great pleasure to have worked with him.

I also wish to thank Dr. R. Douglas Brown for both serving as my thesis supervisor and offering his advice, making them all possible.

Many thanks go to Robert Brown and Andrew Brown for their assistance in the laboratory. Thanks also to my family and friends for their support and encouragement throughout this project. Finally, thank you to my mother for her love and support.

© Copyright by MATTHEW W. TOTTEN JR. 2011
All Rights Reserved.

ACKNOWLEDGEMENTS

This study would not have been possible without the generous help and support of several individuals. My graduate research experience has been very rewarding and I would like to thank all of the faculty, staff, and students in the ConocoPhillips School of Geology and Geophysics for their time, inspiration, and guidance during my tenure at the University of Oklahoma.

Very special thanks go to Dr. Roger M. Slatt for directing and overseeing my research. His encouragement, help, and considerable wisdom regarding gas shales was extremely valuable to me during the different stages of this project. I feel very fortunate to have had the opportunity to work with him and am most grateful to be associated with his extensive and exceptional network of graduate students.

Special thanks go to Dr. George Morgan VI for critically reading this manuscript and helping me to employ the electron microprobe as the main instrument of investigation for this work. His support, patience, and assistance over the course of this research has been invaluable and it has been a great pleasure to have worked with him.

I also wish to thank Dr. R. Douglas Elmore for both serving on my thesis committee and offering his outstanding class on clastic sedimentology.

Many thanks go to Rafael Sierra and Andrea Miceli for their time and help with the Woodford Shale, Wyche-1 well core samples and data sets as well as helping me to integrate my research into the greater body of knowledge built around the Wyche-1 well, OU-Devon-Schlumberger research project.

Special thanks go to Dr. Ze'ev Reches for mentoring me while I was a teaching assistant for his Structural Geology and Introduction to Field Methods classes. It was a

great privilege to have worked with him and I feel very fortunate to have had the opportunity to emulate his exceptional teaching style.

Finally, my most heartfelt thanks go to my parents Matt and Iris Totten and Karen Parsons for all of their support during my pursuit of higher education as well as any of the crazy dreams I've set my mind to over the years. I'm so very fortunate to have brothers and sisters like Nate, Louise, Becky, Cody, and Wyatt that are always looking out for me and always have my back. My family is a rich source of happiness for me and I will always be grateful for their enduring support.

1.1	Geologic Setting	5
1.1.1	Regional Geology	5
1.1.2	Woodford Shale	11
1.2	Objectives	17
2	Methodology	19
2.1	Study Area and Sampling Methodology	19
2.2	Thin Section Sample Preparation	20
2.3	Energy Dispersive X-Ray Analyzer	22
2.4	Energy Dispersive X-Ray Analysis (EDXA)	22
2.5	Wavelength Dispersive X-Ray Spectroscopy (WDX)	24
2.6	Backscattered Electron (BSE) Imaging	25
2.7	Microanalogue Micro Imaging	27
2.7.1	Micro-Mineralogy Log Calculations	29

TABLE OF CONTENTS

Acknowledgements.....	iv
Table of Contents.....	vi
List of Tables.....	xi
List of Figures.....	xii
Abstract.....	xix
1. Introduction.....	1
1.1 Geologic Setting.....	5
1.1.1 Regional Geology.....	5
1.1.2 Woodford Shale.....	11
1.2 Objectives.....	17
2. Methodology.....	19
2.1 Study Area and Sampling Methodology.....	19
2.2 Thin Section Sample Preparation.....	20
2.3 Electron Probe Micro-Analyzer.....	22
2.4 Energy-Dispersive X-Ray Analysis (EDXA).....	22
2.5 Wavelength Dispersive X-Ray Spectroscopy (WDS).....	24
2.6 Backscattered Electron (BSE) Imaging.....	25
2.7 Mineralogical Micro-Logging.....	27
2.7.1 Micro-Mineralogy Log Calculations.....	29

2.8	X-Ray Mapping	33
3.	Results.....	34
3.1	Petrographic and Microprobe Thin Section Imaging and Description.....	34
3.1.1	120.9 ft Petrographic and Microprobe Thin Sections.....	36
3.1.2	135.7 ft Petrographic and Microprobe Thin Sections.....	47
3.1.3	145.3 ft Petrographic and Microprobe Thin Sections.....	52
3.2	Energy Dispersive X-Ray Analyses (EDXA).....	57
3.2.1	120.9 ft EDXA.....	59
3.2.1.1	120.9 ft Calcite EDXA.....	59
3.2.1.2	120.9 ft Quartz EDXA.....	60
3.2.1.3	120.9 ft Pyrite EDXA.....	61
3.2.1.4	120.9 ft Organic EDXA.....	62
3.2.1.5	120.9 ft Dolomite EDXA.....	64
3.2.1.6	120.9 ft Kaolinite EDXA.....	65
3.2.2	135.7 ft EDXA.....	66
3.2.2.1	135.7 ft Dolomite EDXA.....	66
3.2.2.2	135.7 ft Apatite EDXA.....	67
3.2.2.3	135.7 ft Chlorite EDXA.....	68
3.2.3	145.3 ft EDXA.....	69
3.2.3.1	145.3 ft Dolomite EDXA.....	69

3.2.3.2	145.3 ft Apatite EDXA	70
3.2.3.3	145.3 ft Organic EDXA	72
3.2.3.4	145.3 ft Blood-Red Organic Phosphate EDXA	73
3.2.3.5	145.3 ft Mica EDXA.....	74
3.2.3.6	145.3 ft Muscovite EDXA	75
3.2.3.7	145.3 ft K-Feldspar EDXA.....	76
3.3	Wavelength Dispersive X-Ray Spectrometry (WDS) Data.....	77
3.3.1	120.9 ft Sample Calcite-Clay Couplet WDS Weight Percent Element Result	79
3.3.2	120.9 ft Sample Calcite-Clay Couplet WDS Weight Percent Oxide Result...	80
3.3.3	120.9 ft Sample Calcite-Clay Couplet Calculated Mineralogic Fractionation	81
3.4	Micro-Mineralogy Logs.....	82
3.4.1	120.9 ft Micro-Mineralogy Log.....	82
3.4.2	135.7 ft Micro-Mineralogy Log.....	84
3.4.3	145.3 ft Micro-Mineralogy Log.....	86
3.5	Comparison to Bulk-Rock Mineralogy by XRD From Sierra (2011)	88
3.6	WDS X-Ray Intensity Mapping.....	90
4.	Discussion.....	92

4.1	120.9 ft Calcite-Clay Laminated Sample Micro-Stratigraphy	92
4.2	135.7 ft Dolomitic Sample Micro-Stratigraphy	105
4.3	145.3 ft Dolomitic Sample Micro-Stratigraphy	107
4.4	Micro-Mineralogy Log as an Analog to the ECS Tool and BSE Image Photomontage as Analog to Borehole Imaging Tools	110
4.5	Geomechanical Modeling Potential	113
5.	Conclusions	114
6.	Recommendations for Future Work	116
	References	117
	APPENDIX A 120.9 ft Sample WDS Weight Percent Element Result	124
	APPENDIX B 120.9 ft Sample WDS Weight Percent Oxide Result	124
	APPENDIX C 120.9 ft Sample WDS Calculated Mineralogic Fractionation	124
	APPENDIX D 135.7 ft Sample WDS Weight Percent Element Result	124
	APPENDIX E 135.7 ft Sample WDS Weight Percent Oxide Result	124
	APPENDIX F 135.7 ft Sample WDS Calculated Mineralogic Fractionation	124
	APPENDIX G 145.3 ft Sample WDS Weight Percent Element Result	124
	APPENDIX H 145.3 ft Sample WDS Weight Percent Oxide Result	124
	APPENDIX I 145.3 ft Sample WDS Calculated Mineralogic Fractionation	124
	APPENDIX J 120.9 ft BSE Image Photomontage	124
	APPENDIX K 135.7 ft BSE Image Photomontage	124

APPENDIX L 145.3 ft BSE Image Photomontage	124
APPENDIX M 120.9 ft High-Resolution Digital Thin Section Scan.....	125
APPENDIX N 135.7 ft High-Resolution Digital Thin Section Scan.....	125
APPENDIX O 145.3 ft High-Resolution Digital Thin Section Scan.....	125

Table 3. Weighted well, WPA weight percent grade result for one calcite-clay laminate sample in the 120.9 ft sample.....	80
---	----

Table 4. Weighted well, calculated calcite weight fraction for one calcite-clay laminate sample in the 120.9 ft sample.....	81
--	----

Table 5. Top 3000 (2011) XRD half-angle maximum results (%) from "sister" core samples that were analyzed by electron microprobe in this thesis. Entries: Averages of XRD micro-mineralogy parameters plus in from each electron microprobe sample interval.....	88
---	----

LIST OF TABLES

Table 1. Acquisition settings for the 120.9 ft calcite-clay X-ray intensity map analysis.	33
Table 2. Wyche-1 well, WDS weight percent element result for one calcite-clay laminated couplet in the 120.9 ft sample.	79
Table 3. Wyche-1 well, WDS weight percent oxide result for one calcite-clay laminated couplet in the 120.9 ft sample.	80
Table 4. Wyche-1 well, calculated mineralogic fractionation for one calcite-clay laminated couplet in the 120.9 ft sample.	81
Table 5. Top: Sierra (2011) XRD bulk-sample mineralogy results (%) from "sister" core samples to those analyzed by electron microprobe in this thesis. Bottom: Averages of WDS micro-mineralogy per mineral phase in from each electron microprobe sample interval.	88

LIST OF FIGURES

Figure 1. U.S. Shale gas plays of the lower 48 states (EIA, 2011b).....	2
Figure 2. Map of Pontotoc County and its relative location in a map of Oklahoma; a satellite image of the Wyche-1 well and its relative location to the Wyche shale pit; a photomontage of the Wyche shale pit. From Miceli, 2010.....	4
Figure 3. Map of the North American southern mid-continent during the early to middle Paleozoic showing the Oklahoma basin (green) and Ouachita trough (blue) depositional provinces as well as the southern Oklahoma Aulacogen (yellow) tectonic province (modified from Johnson et al., 1989).....	6
Figure 4. Generalized stratigraphic section of the Upper Cambrian to Pennsylvanian units from southern Oklahoma illustrating the nature of the pre-Woodford unconformity as well as periods of nondeposition in black. Modified from Kirkland et al., 1992.	7
Figure 5. General Paleozoic stratigraphic column of the Arkoma Basin. Modified from Perry, 1995; in Portas, 2009 and Miceli, 2010.	9
Figure 6. Map of Oklahoma showing the depositional and tectonic provinces of the state after the orogenic events of the Late Paleozoic. Modified from Johnson and Cardott, 1992.	10
Figure 7. Woodford Shale thickness map of Oklahoma and Western Arkansas. From Comer, 2008b; in Miceli, 2010.	11
Figure 8. Paleogeographic maps of Oklahoma in the Late Devonian to Early Mississippian annotated with red-dashed circles. Modified from Blakey, 2011.	12
Figure 9. Woodford Shale TOC map of Oklahoma and Western Arkansas. From Comer, 2008b; in Miceli, 2010.	14

Figure 10. Woodford Shale organic maturity map of Oklahoma based on vitrinite reflectance (%Ro) data. Modified from Comer, 1992 and Comer, 2008a.....	15
Figure 11. Woodford Shale type log illustrating the Gamma-Ray, Density, and Resistivity log behaviors commonly found in the Woodford Shale. From Cardott, 2007.	16
Figure 12. Schematic of the EDS system modified from Goldstein et al., 1992.....	23
Figure 13. BSE image annotated to illustrate the characteristic gray-scale tones assigned to prominent mineral phases observed with BSE images throughout this thesis..	35
Figure 14. Wyche-1 well, Woodford 120.9 ft petrographic thin section.....	38
Figure 15. BSE image from the 120.9 ft thin section showing where the diagenetic fill of a Tasmanites cyst plucked out during polishing, leaving its lignite coating behind.....	39
Figure 16. Photomicrographs taken from the 120.9 ft petrographic thin section sample showing the different diagenetic quartz precipitation patterns within Tasmanites cysts..	40
Figure 17. Photomicrographs taken from the 120.9 ft petrographic thin section sample showing the different diagenetic-pyrite precipitation patterns within Tasmanites cysts..	41
Figure 18. Photomicrographs taken from the 120.9 ft petrographic thin section sample showing the different compaction patterns among Tasmanites cysts.....	42
Figure 19. Photomicrographs taken from the 120.9 ft petrographic thin section sample showing calcite cementation patterns within a calcite lamination.....	43
Figure 20. (a) Photomicrograph (PPL) taken from the 120.9 ft petrographic thin section coupled with (b) a BSE image taken from the 120.9 ft polished microprobe thin section showing spherical (circular), quartz-filled Tasmanites cysts.....	44

Figure 21. (a) Photomicrograph (XPL) taken from the 120.9 ft petrographic thin section coupled with (b) a BSE image taken from the 120.9 ft polished microprobe thin section showing calcite laminations..... 44

Figure 22. (a) Photomicrograph (PPL) taken from the 120.9 ft petrographic thin section coupled with (b) a BSE image taken from the 120.9 ft polished microprobe thin section showing quartz-filled, partially-compacted Tasmanites cysts with preserved organic walls. 45

Figure 23. (a) Photomicrograph (PPL) taken from the 120.9 ft petrographic thin section coupled with (b) a BSE image taken from the 120.9 ft polished microprobe thin section showing dominantly pyrite-filled, lobate Tasmanites cysts with a minor amount of precipitated quartz..... 45

Figure 24. (a) Photomicrograph (XPL) taken from the 120.9 ft petrographic thin section coupled with (b) a BSE image taken from the 120.9 ft polished microprobe thin section showing spherical (circular), euhedral-pyrite filled, quartz-rimmed Tasmanites cysts that lack a preserved organic wall..... 46

Figure 25. (a) Photomicrograph (PPL) taken from the 120.9 ft petrographic thin section coupled with (b) a BSE image taken from the 120.9 ft polished microprobe thin section showing semi-compacted, dominantly pyrite-filled with quartz-core Tasmanites cysts.. 46

Figure 26. Wyche-1 well, Woodford 135.7 ft petrographic thin section..... 48

Figure 27. (a) Photomicrograph (PPL) taken from the 135.7 ft petrographic thin section coupled with (b) a BSE image taken from the 135.7 ft polished microprobe thin section showing zones of coarser, euhedral pyrite..... 49

Figure 28. (a) BSE image taken from the 135.7 ft polished microprobe thin section coupled with (b) a photomicrograph (XPL) taken from the 135.7 ft petrographic thin section showing what is speculated to be the morphologies of compacted Tasmanites algal cysts that have been completely replaced by chalcedony.	50
Figure 29. Photomicrograph (XPL) taken from the 135.7 ft petrographic thin section showing a thin layer of chalcedony-rimmed and pyrite-cored Tasmanites algal cysts found in the very top portion of the thin section.....	51
Figure 30. Wyche-1 well, Woodford 145.3 ft petrographic thin section.....	53
Figure 31. (a) BSE image taken from the 145.3 ft polished microprobe thin section coupled with a (b) Photomicrograph (PPL) taken from the 145.3 ft petrographic thin section showing thin, comparable laminations of mixed detrital dolomite and quartz found at low frequency in the 145.3 ft sample interval.	54
Figure 32. (a) BSE image taken from the 145.3 ft polished microprobe thin section coupled with a (b) Photomicrograph (PPL) taken from the 145.3 ft petrographic thin section showing relatively large pyrite framboids that appear in low frequency throughout the 145.3 ft thin section interval.	55
Figure 33. (a) Photomicrograph (PPL) taken from the 145.3 ft petrographic thin section coupled with a (b) BSE image taken from the 145.3 ft polished microprobe thin section showing highly compacted, thin, dark-brown to opaque organic stingers.	56
Figure 34. EDXA of the Wyche-1, Woodford 120.9 ft sample within a calcite grain located in a calcite lamination.....	59
Figure 35. EDXA of the Wyche-1, Woodford 120.9 ft sample within a quartz grain located in a clay lamination.	60

Figure 36. EDXA of the Wyche-1, Woodford 120.9 ft sample within a pyrite grain (bright white in BSE image) located in a clay lamination. 61

Figure 37. EDXA of the Wyche-1, Woodford 120.9 ft sample within a ruptured and compressed Tasmanites-cyst organic wall (black in BSE image) located in a clay lamination. 62

Figure 38. EDXA of the Wyche-1, Woodford 120.9 ft sample within a Tasmanites-cyst organic wall (black in BSE image) located in a clay lamination. 63

Figure 39. EDXA of the Wyche-1, Woodford 120.9 ft sample within a dolomite grain located in a calcite lamination..... 64

Figure 40. EDXA of the Wyche-1, Woodford 120.9 ft sample within an authigenic kaolinite clay (dark gray in BSE image) located inside a Tasmanites algal cyst filled rim. 65

Figure 41. EDXA of the Wyche-1, Woodford 135.7 ft sample within a dolomite grain located in the clay matrix of the sample. 66

Figure 42. EDXA of the Wyche-1, Woodford 135.7 ft sample within a coarse, detrital apatite grain located in the clay matrix of the sample. 67

Figure 43. EDXA of the Wyche-1, Woodford 135.7 ft sample within a chlorite grain (light gray in BSE image) located in the clay matrix of the sample. 68

Figure 44. EDXA of the Wyche-1, Woodford 145.3 ft sample within a dolomite grain (dark gray in BSE image) located in the clay matrix of the sample. 69

Figure 45. EDXA of the Wyche-1, Woodford 145.3 ft sample within apatite (light gray BSE image) located in the core of a dolomite grain (dark gray) of the sample..... 70

Figure 46. EDXA of the Wyche-1, Woodford 145.3 ft sample within an apatite grain (light gray in BSE image) located in a dolomite lamination of the sample.....	71
Figure 47. EDXA of the Wyche-1, Woodford 145.3 ft sample within an organic stringer (black in BSE image) located in the clay matrix of the sample.....	72
Figure 48. EDXA of the Wyche-1, Woodford 145.3 ft sample within a blood-red (under the petrographic microscope) organic-rich phosphate.....	73
Figure 49. EDXA of the Wyche-1, Woodford 145.3 ft sample within a mica grain (light gray in BSE image) located in the clay matrix of the sample.....	74
Figure 50. EDXA of the Wyche-1, Woodford 145.3 ft sample within a muscovite grain (light gray in BSE image) located in the clay matrix of the sample.....	75
Figure 51. EDXA of the Wyche-1, Woodford 145.3 ft sample within a K-feldspar grain (light gray in BSE image) located in the clay matrix of the sample.....	76
Figure 52. Crops of the scanned digital image of the 120.9 ft petrographic thin section paired with its corresponding 120.9 ft electron microprobe thin section BSE image photomontage showing the calcite-clay laminated couplet corresponding to a WDS data interval	78
Figure 53. Wyche-1 well, Woodford 120.9 ft micro-mineralogy log from WDS analysis.	83
Figure 54. Wyche-1 well, Woodford 135.7 ft sample microprobe analysis.....	85
Figure 55. Wyche-1 well, Woodford 145.3 ft sample electron microprobe analysis.	87
Figure 56. X-ray intensity maps of elements Ca, Mg, Si, O, Fe, S, K, Al, and Na coupled with a BSE image of a calcite-clay laminated couplet in the Wyche-1, 120.9 ft sample.	90


Figure 57. Photomicrograph of the 50 μm thick, electron microprobe thin section (PPL) showing quartz growth rings with euhedral pyrite grains at their center in a dominantly quartz-filled Tasmanites cyst.	96
Figure 58. Tasmanites green algae life cycle modified from Tappan (1980).	98
Figure 59. Schematic presentation of early diagenetic processes in quartz- and pyrite-filled Tasmanites algal cysts modified from Schieber (1996).	101
Figure 60. Linear cross plots from the 120.9 ft micro-mineralogy log results showing organics vs. clay, quartz, calcite, and dolomite.	103
Figure 61. Increasingly higher magnification BSE images within a calcite lamination in the Wyche-1, 120.9 ft, electron microprobe thin section showing the calcite grain morphology and cementation behavior of the quartz grains.	104
Figure 62. (a) Photomicrograph (XPL) of the 145.3 ft optical thin section showing a long, dark-brown organic lense and a microquartz-dolomite mixed lens. (b) Photomicrograph (XPL) of the 145.3 ft optical thin section showing a lens of mixed microquartz and dolomite.	109
Figure 63. Side-by-side comparison of scales between the ECS, FMI, and micro-mineralogy logs.	112



ABSTRACT

Three samples from the Wyche-1, Late Devonian Woodford Shale, OU-Devon-Schlumberger research core were analyzed with a Cameca SX-50 electron probe micro-analyzer with the aim of characterizing the mineralogy of very fine grained shale samples perpendicular to their laminations and with a vertical resolution < 100 micrometers. The samples chosen for analysis were the remaining pieces of core material that had been prepared by Sierra (2011) for geomechanical experimentation.

Micro-mineralogy of the samples was accomplished from chemical analyses performed by Wavelength Dispersive X-ray Spectrometry (WDS) and the resulting data were plotted as micro-mineralogy logs. Elemental Capture Spectroscopy logs (ECS - trade mark of Schlumberger), generated from capture gamma-ray spectroscopy in cased and uncased boreholes, can be thought of as analogous to micro-mineralogy logs, but with coarser vertical resolutions between 1.5 ft (uncased boreholes) to 2.5 ft (cased boreholes) (Schlumberger, 2000). Additional techniques performed with the aim to complement the WDS analysis included Backscattered Electron (BSE) imaging, which was taken throughout each sample and along each WDS spot analysis transect line, Energy Dispersive X-ray Analysis (EDXA) to characterize mineral phases when examining samples in live-time BSE imaging, X-ray intensity mapping of a selected area within a calcite-clay laminated couplet, and plane/cross polarized light microscopy of "sister" petrographic thin sections. Overlapping BSE images acquired along each WDS analysis transect line were stitched into a photomontage producing an image log analogous to lower vertical resolution image logs produced using borehole imaging tools. To finalize each micro-mineralogy log for visual analysis, the micro-mineralogy log,



BSE photomontage, and digitally-scanned image of a complete thin section were scaled and cross-correlated.

Analysis of all the data sets for each sample allowed for micro-stratigraphic observations and interpretations. Cross plots of micro-mineralogy log organics versus individual mineral phases allowed for trends to be observed showing decreases in organic content within more brittle calcite-cemented quartz laminations and increases in organic content within more ductile clay laminations. Such brittle-ductile couplet combinations offer the potential for lamination scale reservoir-source amalgamations if targeted for hydraulic fracture. Tasmanites algal cyst identification, the diagenetic precipitation of quartz and pyrite within such palynomorphs, and the variety of observed cyst compaction features offered evidence for inferences about changes in rate of deposition, radiolarian test origins for internal cyst diagenetic quartz, and activity pulses by bacterial sulfate reducing organisms based on internal cyst pyrite precipitation. The presence of fine calcite grains with distinct circular morphologies also presented evidence for calcareous algae or calcareous coral-spore deposition. Observations of minor detrital apatite bone fragments as well as organic-rich apatite grains provided inferences for anoxic ocean water conditions.

Based on the methods employed in this thesis, I recommend that electron probe micro-analysis of core, sidewall core, and cutting samples be integrated into the reservoir characterization of gas shales because microprobes have spatial resolution on scales at or near the realm of shale grains and can more accurately provide high resolution mineralogic data for geomechanical modeling upon which many hydraulic fracture completions of gas shale reservoirs are now based.

1. INTRODUCTION

Until recent decades, shales were regarded exclusively as organic-rich source and seal mudstones that were economically unworthy of research to the degree that other sedimentary rocks received (Potter, 1980). With the advent of modern hydraulic fracture and horizontal drilling technologies, disinterest towards shales as an insignificant lithology exploded into an active arena of scientific research focused on characterizing these complex and highly variable fine grained rocks, which now seem to have an economic priority among both academia and the oil and gas industry.

The fact that shales comprise more than 60 percent of the Earth's sedimentary record (Potter et al., 1980) generates enormous economic potential for unconventional gas discoveries. Recent industry activity in the continental U.S. reflects this with 4.87 Tcf of shale gas production in 2010 (23 percent of the total U.S. natural gas production) as compared to just 0.39 Tcf in 2000 (EIA, 2011a). Figure 1 (EIA, 2011b) shows a map of the continental U.S. with current and prospective shale gas plays outlined in their respective basins. In the Oklahoma Woodford Shale gas plays alone, the application of advanced completion technologies from the year 2004 (Cardott, 2009) resulted in a marked increase in wells from an average of just two completions per year between 1934 to 2003 (Wickstrom, 2008), up to 501 horizontal completions for the 365 days of 2009 (Cardott, 2009).



Figure 1. U.S. Shale gas plays of the lower 48 states from EIA, 2011b.

Shale research for the purpose of understanding shale gas reservoir characteristics has increased enormously in the past decade with the integration of geoscience disciplines such as geology, geophysics, geochemistry, geomechanics, and petroleum engineering (Portas, 2009; Miceli, 2010; Slatt et al., 2010; Sierra, 2011). Furthermore, shales have been studied on a multitude of scales from regions, to basins, to outcrops and single core (Slatt et al., 2010). However, the nature of gas shales as fine-grained silt and clay rocks full of organic material requires that even finer detailed analyses be performed to understand shales and their complex variability at the individual lamination to grain scales. The development of advanced preparation techniques for clay and silt-sized rock samples (O'Brien and Slatt, 1990; Vardilos, personal communication, 2010) as well as the increased availability of micro- and nano-scale investigative instruments (SEMs, electron

microprobes, and nano-indenters) has facilitated such research (O'Brien and Slatt, 1990; Hover et al., 1996; Schieber, 1996; Schieber and Baird, 2001; Abousleiman et al., 2010). However, analyses on such small scales are tedious, cover only small areas, and usually discover the existence of even greater complexities within the intervals examined. Thus, much more work is required to characterize shales on the nano- to micro-scales and to effectively integrate such data with the findings of larger unit, formation, and basin scale research to ultimately support the exploration and efficient production of gas shale plays.

This thesis is focused on the implementation of electron microprobe methods that will better characterize shale samples on the thin section, lamination, and sub-lamination scales. Three core samples from a Woodford Shale, behind outcrop/quarry well (Figure 2) were analyzed perpendicular to their laminations in order to generate sub-100 micrometer vertical resolution micro-mineralogy logs. Such data was used for micro-stratigraphic interpretation and can be integrated with other shale gas reservoir characterization techniques in the future.



Figure 2, from top to bottom: Map of Pontotoc County and its relative location in a map of Mississippi; a satellite image of the Wyche-1 well and its relative location to the Wyche shale pit; a photograph of the Wyche shale pit with an arrow indicating the location of the Wyche-1 well in the distance. From Miall, 2010

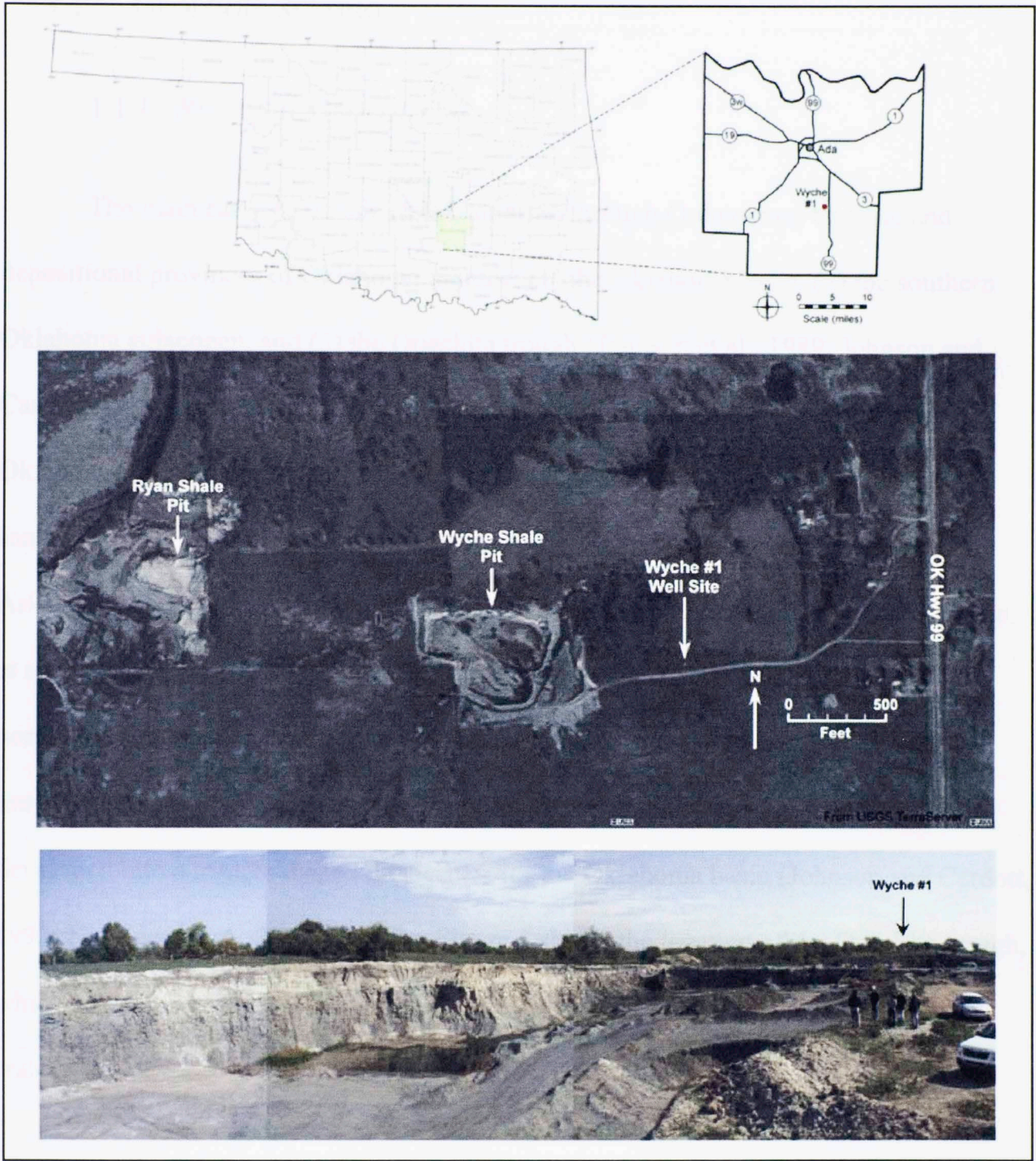


Figure 2. From top to bottom: Map of Pontotoc County and its relative location in a map of Oklahoma; a satellite image of the Wyche-1 well and its relative location to the Wyche shale pit; a photomontage of the Wyche shale pit with an arrow indicating the location of the Wyche-1 well in the distance. From Miceli, 2010.

1.1 GEOLOGIC SETTING

1.1.1 REGIONAL GEOLOGY

The main early Paleozoic (late Cambrian through Ordovician) tectonic and depositional provinces of Oklahoma include: (1) the Oklahoma basin, (2) the southern Oklahoma aulacogen, and (3) the Ouachita trough (Johnson et al., 1989; Johnson and Cardott, 1992; Northcutt et al., 2001). Figure 3 shows the expansive nature of the Oklahoma basin, a thick, shallow-marine carbonate shelf interbedded with thin marine sandstones, covering the majority of Oklahoma and extending into northwestern Arkansas, southern Kansas, southeast Nebraska, and north to northwest Texas (Johnson et al., 1989; Johnson and Cardott, 1992; Northcutt et al., 2001). It also shows the northwest-southeast trending southern Oklahoma aulacogen, which began as an intracratonic rift during the Late Precambrian to Early Cambrian (Webster, 1977) and developed into a trough-shaped depocenter for the Oklahoma basin (Johnson and Cardott, 1992; Northcutt et al., 2001). Finally, Figure 3 shows the location of the Ouachita trough, which accumulated deepwater sediments due to earlier rifting of the North American craton (Johnson and Cardott, 1992; Northcutt et al., 2001).

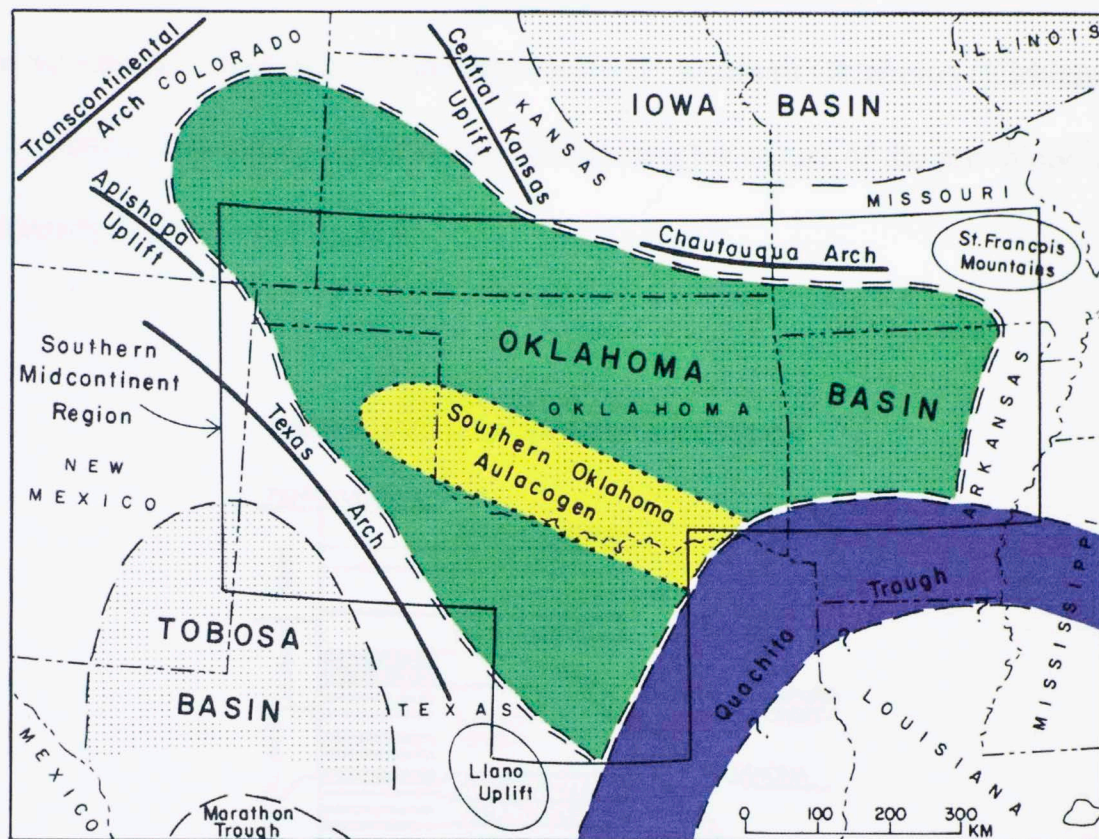


Figure 3. Map of the North American southern mid-continent during the early to middle Paleozoic showing the Oklahoma basin (green) and Ouachita trough (blue) depositional provinces as well as the southern Oklahoma Aulacogen (yellow) tectonic province. Modified from Johnson et al., 1989.

Silurian through Early Devonian deposition included the continued sedimentation of thick, shallow marine limestones of the Hunton Group (Johnson and Cardott, 1992). These limestones grade from clean-washed fossiliferous limestones at the base, to argillaceous and silty carbonates in the middle then back to clean-washed limestones at the top (Johnson and Cardott, 1992). Coeval dolomite units appear away from the axis of the southern Oklahoma aulacogen in the shallower shelf areas to the north (Johnson and Cardott, 1992). A significant epeirogenic uplift and erosional event occurred after deposition of the Hunton Group that led to what is now termed the pre-Late Devonian (pre-Woodford-Chattanooga) unconformity (Johnson et al., 1989) that exposes units as

old as the Arbuckle formation (late Cambrian to early Ordovician) in northern Oklahoma and the Sylvan shale formation (Late Ordovician) in southern Oklahoma (Kirkland et al., 1992). A generalized stratigraphic section illustrating the nature of the pre-Woodford unconformity is shown in Figure 4.

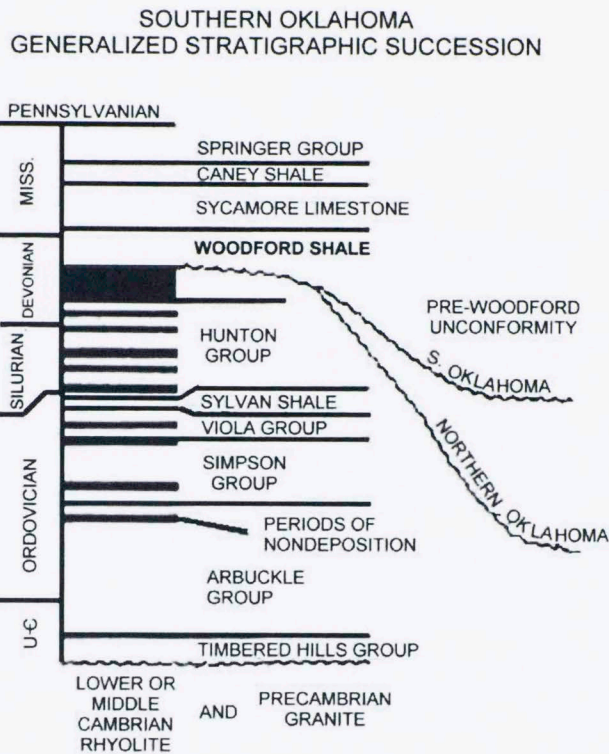


Figure 4. Generalized stratigraphic section of the Upper Cambrian to Pennsylvanian units from southern Oklahoma illustrating the nature of the pre-Woodford unconformity as well as periods of nondeposition in black. Modified from Kirkland et al., 1992.

The late Middle Devonian to early Late Devonian time period brought with it the transgression of a euxinic ocean from the south-southeast (Kirkland et al., 1992) that resulted in the deposition of dark-gray to black, fine-silt to clay-sized sediments that comprise the organic rich Woodford Shale (Johnson et al., 1989). Initial deposition of the Woodford incorporated much of the exposed Hunton Group debris and sands into thin basal conglomerate or sandstone units referred to as the Misener-Sycamore Sandstones

(Johnson et al., 1989). Woodford Shale deposition continued until the early Mississippian when warm, shallow and oxygenated ocean conditions prevailed, which supported a plethora of different benthic organisms that resulted in the accumulation of conformable limestone formations above the Woodford (Johnson and Cardott, 1992). The general Paleozoic stratigraphy of the Arkoma basin in southeastern Oklahoma is shown in Figure 5.

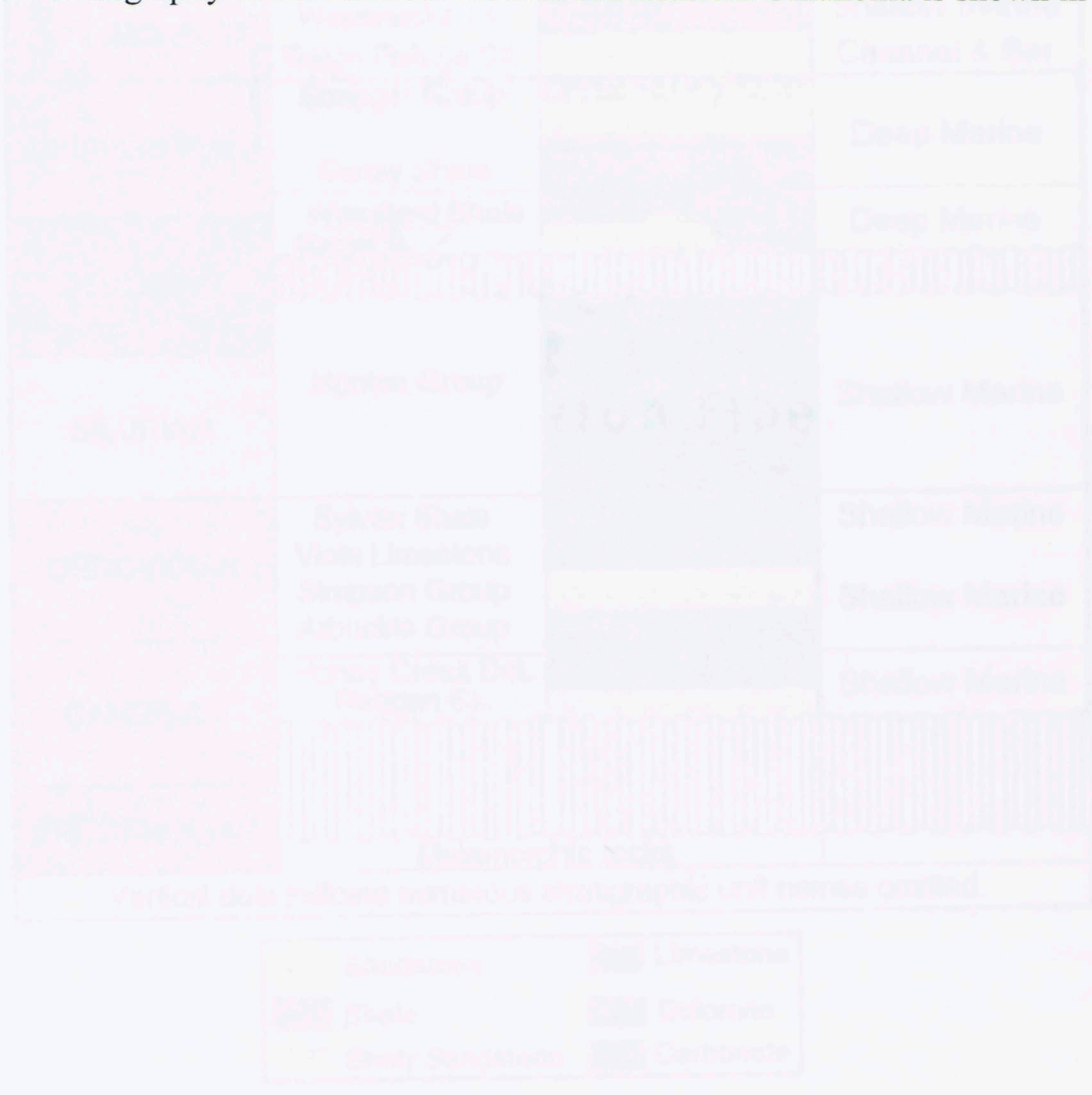


Figure 5. General Paleozoic stratigraphic column of the Arkoma Basin. Modified from Perry, 1985, in Purvis, 2009 and Mizell, 2010.

Late Mississippian to Early Pennsylvanian Oklahoma underwent further tectonic uplift and erosion followed by major periods of orogenesis throughout the Early Middle and Late Pennsylvanian due to the collision of Laurentia and Gondwana, producing the tectonic and depositional provinces as described today (Johnson and

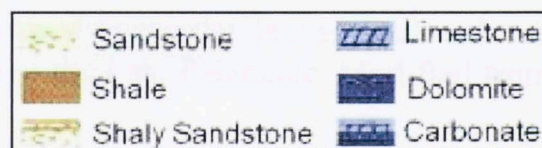
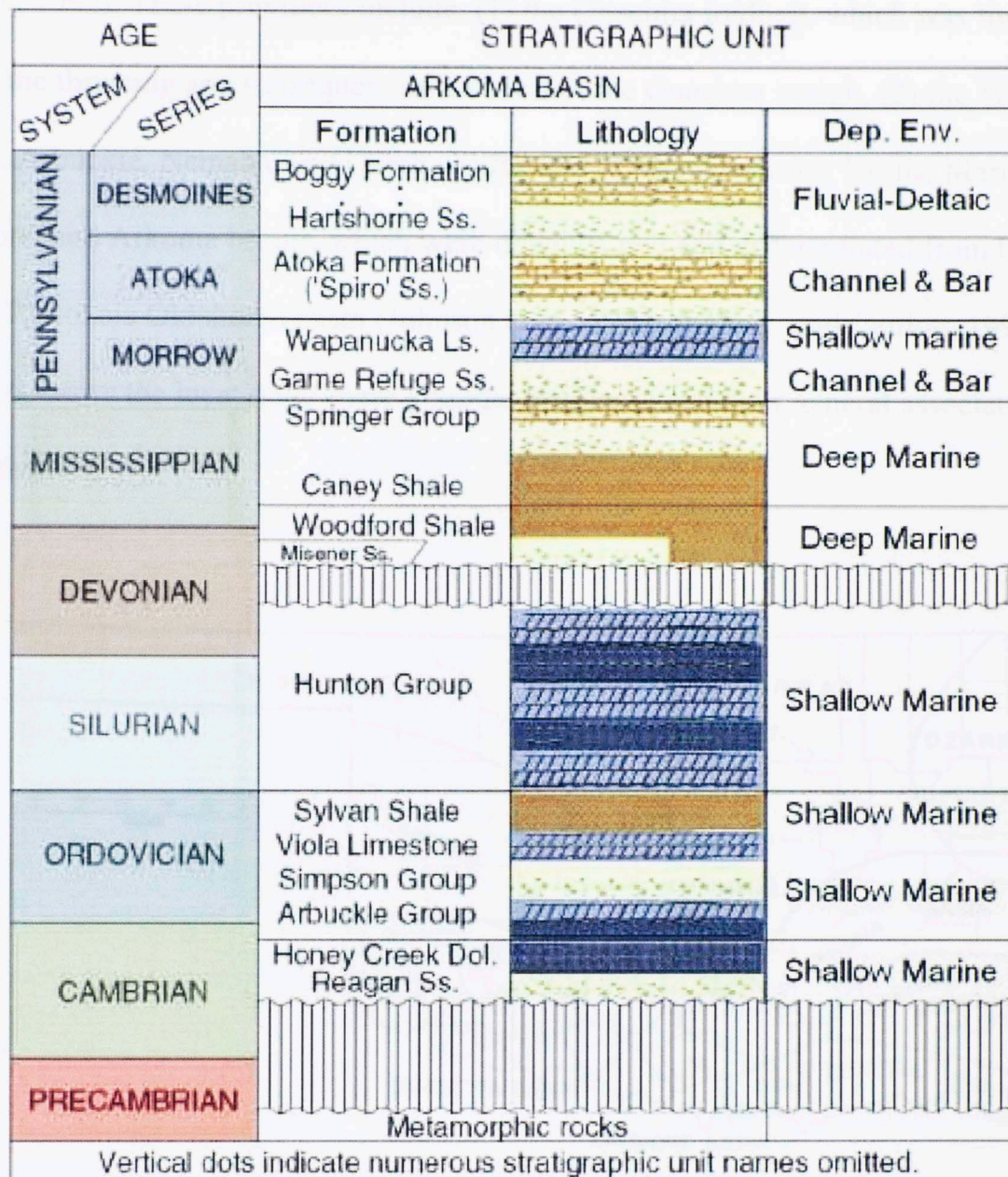


Figure 5. General Paleozoic stratigraphic column of the Arkoma Basin. Modified from Perry, 1995; in Portas, 2009 and Miceli, 2010.

Late Mississippian to Early Pennsylvanian Oklahoma underwent further epeirogenic uplift and erosion followed by major periods of orogenesis throughout the Early, Middle, and Late Pennsylvanian due to the collision of Laurentia and Gondwana, producing the tectonic and depositional provinces as described today (Johnson and

Cardott, 1992). These provinces include: (1) the Ouachita foldbelt, which was formed due to the thrusting and subsequent destruction of the Ouachita trough, (2) the Wichita, Criner, Arbuckle, Nemaha, and Ozark uplifts, and (3) the Anadarko, Hollis, Marietta, Ardmore, and Arkoma basins, which were downwarped and differentiated from the earlier Paleozoic Oklahoma basin (Johnson et al., 1989; Johnson and Cardott, 1992).

Figure 6 shows the location of these younger provinces and their general association with each other.

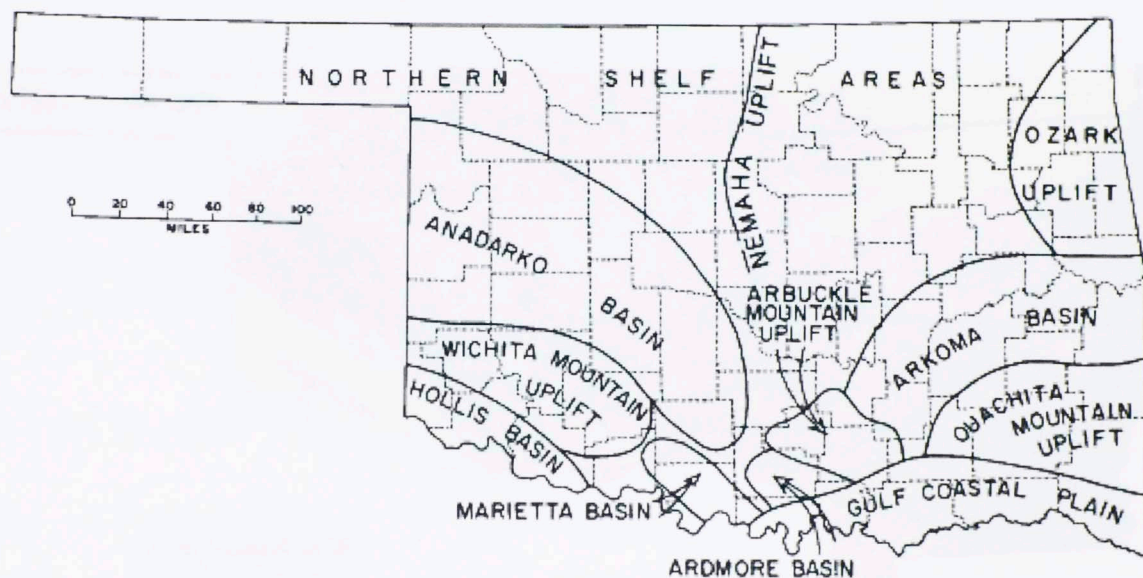


Figure 6. Map of Oklahoma showing the depositional and tectonic provinces of the state after the orogenic events of the Late Paleozoic. Modified from Johnson and Cardott, 1992.

1.1.2 WOODFORD SHALE

The Woodford Shale is a Late Devonian to Early Mississippian organic-rich black shale that was deposited over much of Oklahoma, southern Kansas, and western Arkansas (Johnson et al., 1989). Unit thicknesses range from 200 to 900 ft in the southern Oklahoma aulacogen and 50 to 100 ft on the shallower shelf areas in northern Oklahoma (Johnson and Cardott, 1992). Figure 7 shows the thinning behavior of the Woodford from the aulacogen onto the Cherokee Platform.

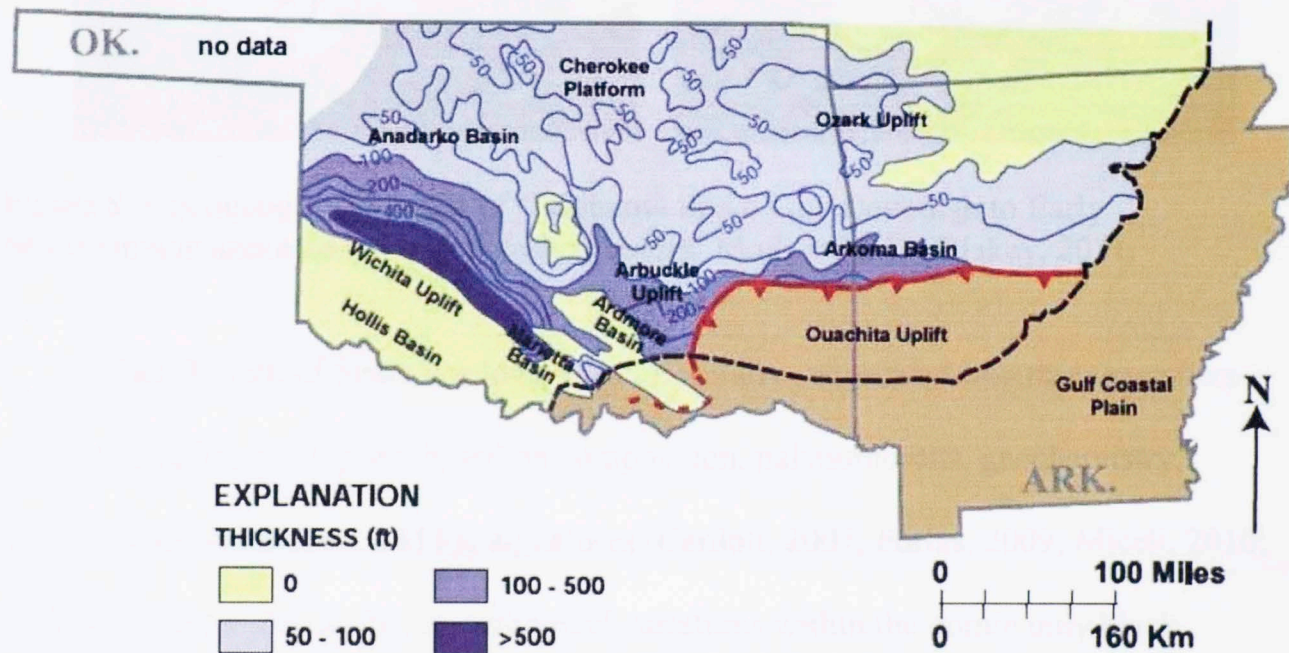


Figure 7. Woodford Shale thickness map of Oklahoma and Western Arkansas. From Comer, 2008b; in Miceli, 2010.

North American black shale stratigraphic equivalents include such formations as the Chattanooga Shale, Arkansas Novaculite, Antrim Shale, Bakken Shale, New Albany Shale, and Ohio Shale (Sullivan et al., 1985; Kirkland et al., 1992; Northcutt et al., 2001). The paleogeographic location of Oklahoma on the ancestral continent of Laurentia during

the Late Devonian and Early Mississippian epochs is delimited by red-dashed circles in Figure 8.

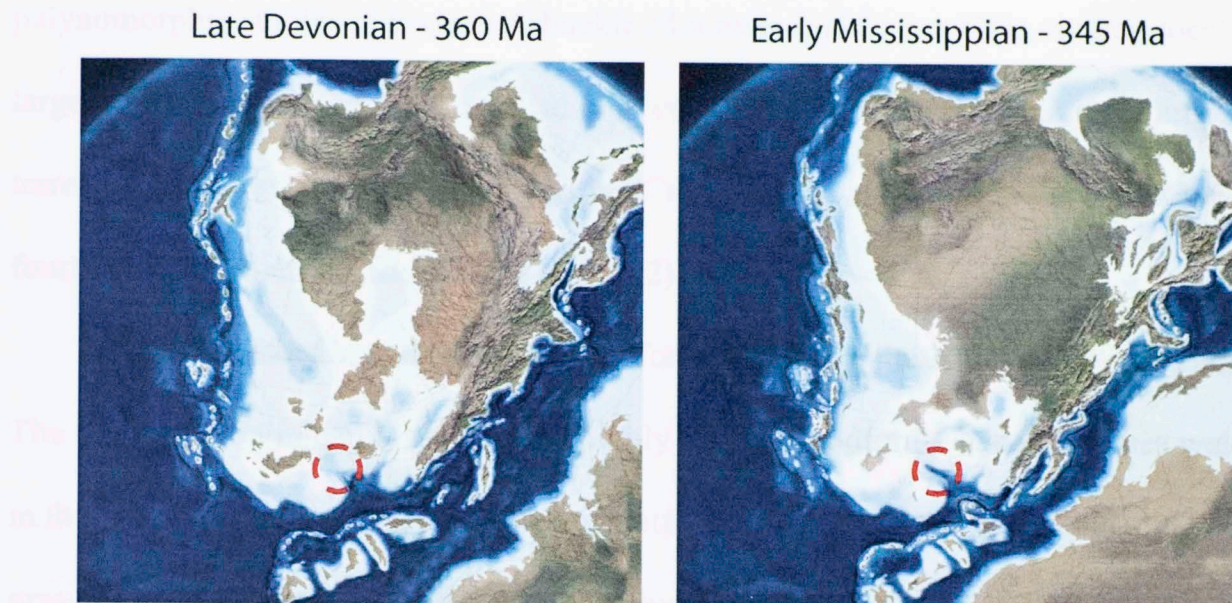



Figure 8. Paleogeographic maps of Oklahoma in the Late Devonian to Early Mississippian annotated with red-dashed circles. Modified from Blakey, 2011.

The Woodford Shale has long been informally subdivided into three members (Lower, Middle, and Upper) based on composition, palynomorphs, geochemistry, geomechanical response, and log signatures (Cardott, 2007; Portas, 2009; Miceli, 2010; Slatt et al., 2010; Sierra, 2011). Lithological variations within the dominantly black Woodford Shale include that of chert, siltstone, sandstone, dolostone, and light-colored shale (Comer, 2005). Kirkland et al. (1992) examined several phosphate nodules, pyrite concretions, and calcite concretions throughout various stratigraphic intervals of the southern Oklahoma Woodford Shale and also documented the presence of siliceous spheres, conodonts, planktonic remains (e.g. *Tasmanites* algal cysts and radiolaria), tiny lenses of silica, and scattered opaque minerals. Less commonly seen are ammonoid and crustacean fossil remains, which are restricted to the upper one-seventh of the Woodford



Shale formation (Kirkland et al., 1992). Hass and Huddle (1965) determined a Late Devonian to Early Mississippian age based on conodont zonation whereas Urban (1960), Van Almen (1970), and Schwartzapfel and Holdsworth (1996) conducted very detailed palynomorphologic studies in various Arbuckle Mountain and Criner Hills outcrop locations largely focusing on algal cysts and radiolarians. Micro- and macro-fauna including terrestrial plants such as *Callixylon* sp. and *Calamites* sp. are found in the lower one-fourth of the formation (Kirkland et al., 1992).

The Woodford was deposited unconformably above the Hunton Group carbonates. The transgression of calm, anoxic, and highly saline Woodford-Chattanooga sea waters in the Late Devonian onto this carbonate platform allowed for the deposition and preservation of organic particles in large volumes without being diluted by excessive clastic input (Kirkland et al., 1992; Comer, 2005). Organic geochemistry by Kirkland et al. (1992) and Miceli (2010) established Woodford Shale kerogen as dominantly type II (marine origin) with TOC values ranging from 1% to 17%. One important division of the Lower, Middle, and Upper Woodford is the variation in TOC content throughout the formation; the Middle Woodford has the highest values whereas the Upper Woodford has the lowest (Kirkland et al., 1992; Miceli, 2010; Slatt et al., 2010). Figure 9 shows the generalized behavior of Woodford Shale TOC accumulations throughout Oklahoma (Comer, 2008b; in Miceli, 2010).

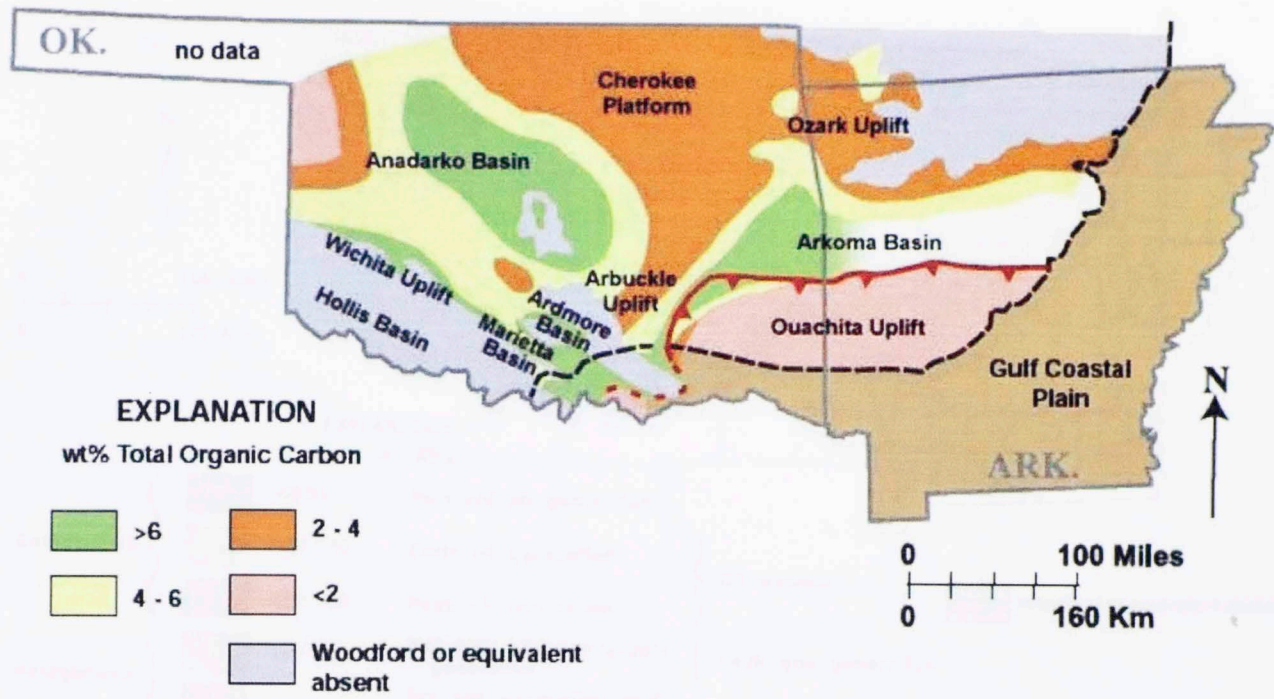


Figure 9. Woodford Shale TOC map of Oklahoma and Western Arkansas. From Comer, 2008b; in Miceli, 2010.

Based on vitrinite reflectance data, organic maturity of the Woodford Shale in Oklahoma ranges from low, incipient oil generation values ($< 0.5 \%R_o$) along the Nemaha uplift throughout central Oklahoma to high, dry gas generation values ($> 2.0 \%R_o$) in the deeper portions of the Anadarko and Arkoma basins (Comer, 1992; Comer, 2008a). Such data is supported by further geochemical work by Miceli (2010) who obtained several $\%R_o$ values from core and cutting samples throughout south central Oklahoma. Figure 10 is a map of organic maturity in the Woodford Shale throughout Oklahoma illustrating the behavior of Woodford Shale vitrinite reflectance.

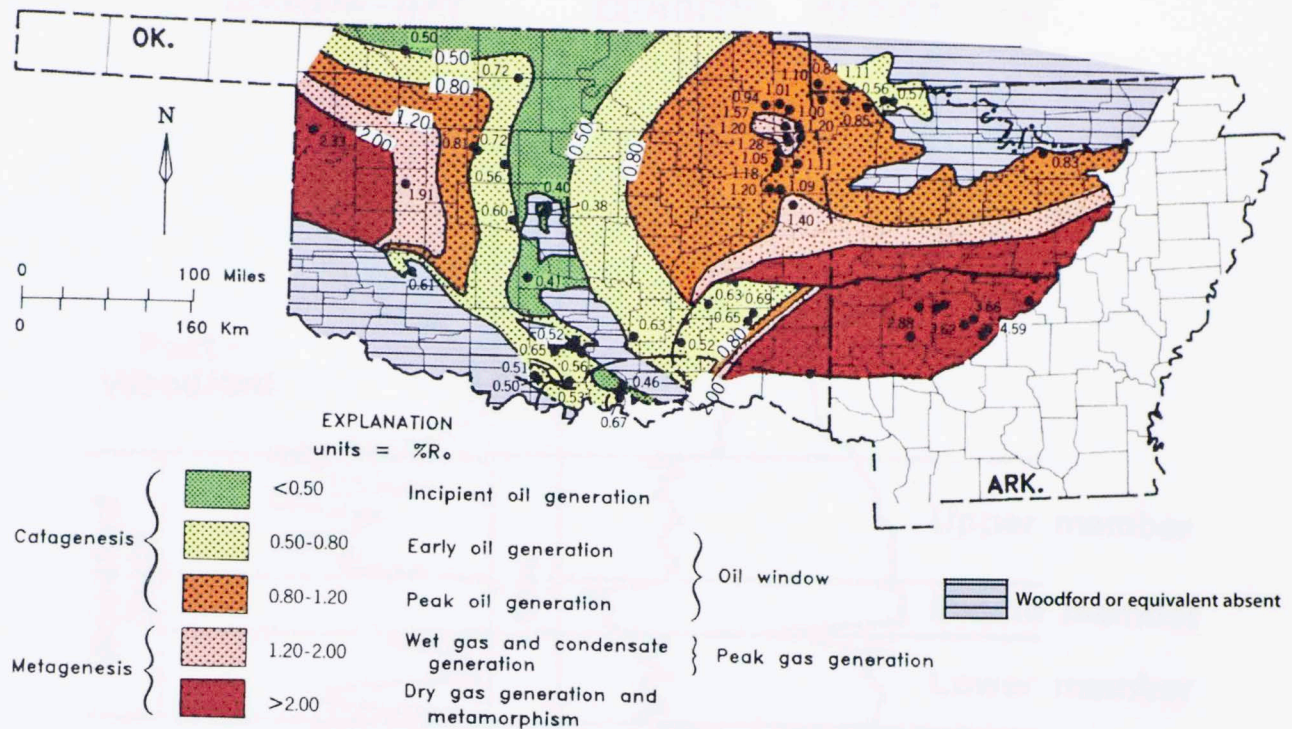


Figure 10. Woodford Shale organic maturity map of Oklahoma based on vitrinite reflectance (%R_o) data. Modified from Comer, 1992 and Comer, 2008a.

The Woodford Shale is considered a "hot" shale as it consistently produces high gamma ray readings on both wireline logs, core gamma ray scans, and outcrop gamma ray measurements (Kirkland et al., 1992; Miceli, 2010; Slatt et al, 2010). This is attributable to the high organic content of the formation, which has an affinity for uranyl ions (Kirkland et al., 1992; Lambert, 1993). As the type log in Figure 11 illustrates, the Middle Woodford is differentiated from the Lower and Upper units by its significantly higher gamma ray response (Cardott, 2007). Also, the Lower Woodford is differentiated from the underlying Hunton Group limestones by its sudden increase in gamma ray values as well. In general, the Woodford is characterized by high gamma ray, high resistivity, and low density readings (Kirkland et al., 1992).

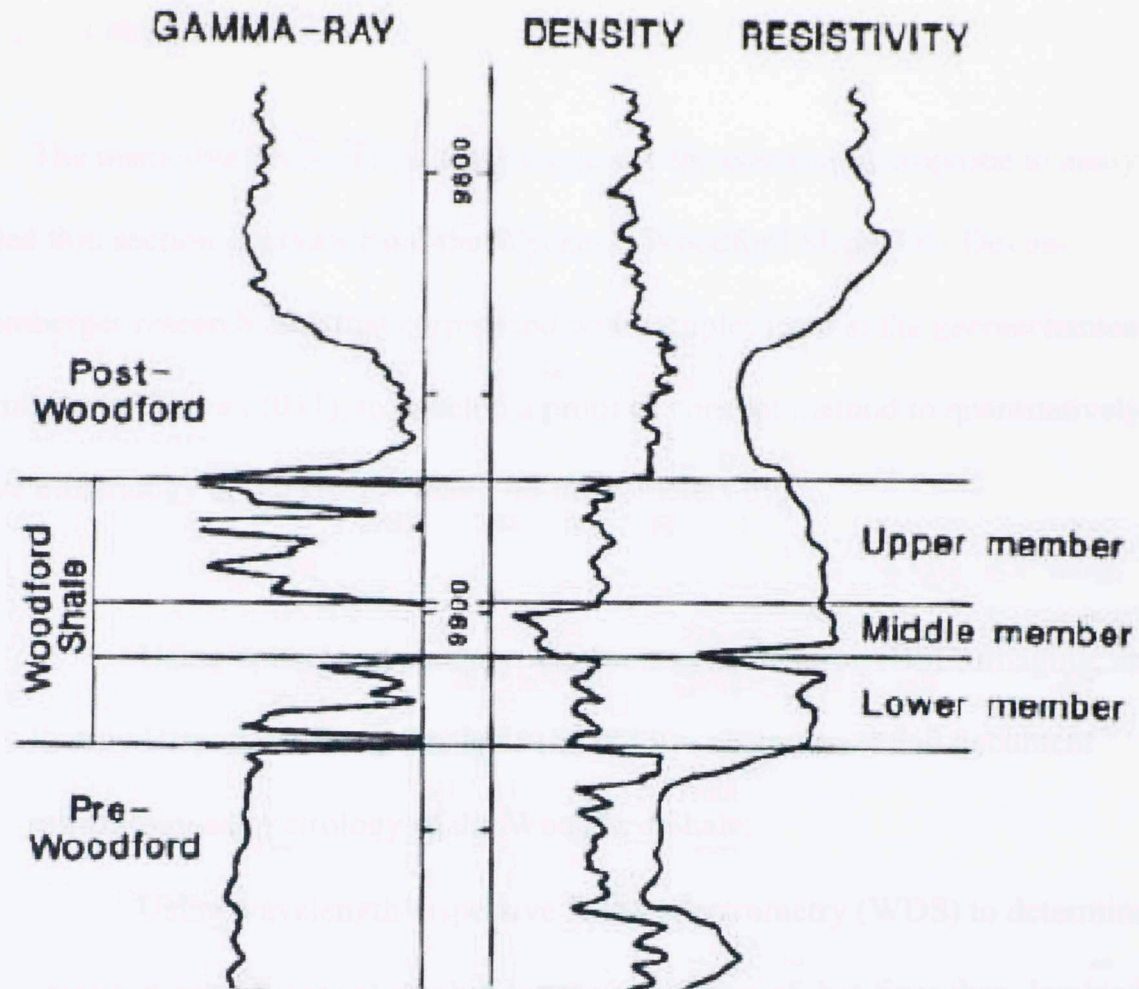


Figure 11. Woodford Shale type log illustrating the Gamma-Ray, Density, and Resistivity log behaviors commonly found in the Woodford Shale. From Cardott, 2007.

Finally, a sequence stratigraphic framework for the Woodford Shale has been established on the basis of Lower, Middle, and Upper unit distribution as well as log and geochemical findings. From this data, the framework is as follows: the Lower Woodford was deposited over a regional unconformity during the rising sea level stage of a transgressive systems tract (TST), the Middle Woodford was deposited during the maximum flooding stage of the same TST, and the Upper Woodford was deposited during the falling sea level stage of the subsequent high-stand systems tract (HST) (Lambert, 1993; Slatt et al., 2010).



1.2 OBJECTIVES

The main objectives of this study are to use the electron microprobe to analyze selected thin section intervals from the Wyche-1, Woodford Shale, OU-Devon-Schlumberger research core that correspond with samples used in the geomechanical experiments of Sierra (2011), to develop a proof of concept method to quantitatively resolve mineralogy at a scale less than 100-micrometers by:

- Using optical petrography, Backscattered Electron (BSE) imaging, and Energy Dispersive X-ray Analysis (EDXA) to characterize and document mineralogy and petrology of the Woodford Shale;
- Using wavelength dispersive X-ray spectrometry (WDS) to determine the compositions of areas at resolutions representative of, but finer than, laminations within the shale;
- Conversion of compositions to modal mineralogy by mass balance, constrained by the compositions and/or atomic ratios of minerals present in the samples;
- Using the resulting data to better understand the Woodford Shale environment of deposition (EOD), depositional processes, the role of organisms and biogenic grains, as well as the relative timing between diagenetic quartz and pyrite precipitation in *Tasmanites* algal cysts.

It is the working hypothesis of this thesis that the microprobe method of determining mineralogy should provide greater accuracy than bulk analysis by XRD and,

because it is a non-destructive method, will preserve the samples for complimentary petrologic analysis.

2.1 STUDY AREA AND SAMPLING METHODOLOGY

Samples were taken from a 210 ft deep research borehole core that was drilled adjacent to the Wyche, Woodford Shale quarry in Pottawatomie County, Oklahoma (Portas, 2008). The Wyche quarry is approximately 1.5 miles south of Ada, Oklahoma and 30 miles to the northeast of Muskogee in Oklahoma's north central Arkhockle Mountains. The recovered core from the Wyche-1 well ends 2 ft above the Woodford-Huntan unconformity (contact at 212 ft) (Stett et al., 2010). The name of the borehole is designated the Wyche-1 and is located approximately 500 ft to the east of the easternmost Wyche quarry well (Figure 2) (Mucchi, 2010).

Core recovery of the 210 ft deep Wyche-1 well was 190 ft (90%) and was complemented by a suite of Schlumberger wireline logs including: (1) gamma ray, (2) resistivity, (3) porosity (porosity - DP), (4) neutron porosity (NPHI), (5) Combination Magnetometer (MR), (6) Sonic Slowness (MSP), (7) Elemental Capture Spectrometer (ECS), and (8) Formation MicroScanner (FMI) (Stett et al., 2010).

Porosity sections of the integrated Formation MicroScanner (FMI) of the University of Oklahoma immediately preserved sections of the core in non-reactive Multigrade PG-1 mineral oil in a vacuum to let the slabs desiccate before geochemical experiments could be conducted (Stett et al., 2010; Stett et al., 2010; Swartz, 2011). The remaining core that was not placed in mineral oil was then slotted, as described and evaluated by Nicole Buckner of the University of Oklahoma Reservoir Characterization Institute (Bhatt et al., 2010).



2. METHODOLOGY

2.1 STUDY AREA AND SAMPLING METHODOLOGY

Samples were taken from a 210 ft deep research borehole core that was drilled adjacent to the Wyche, Woodford Shale quarry in Pontotoc County, Oklahoma (Portas, 2009). The Wyche quarry is approximately 7.5 miles south of Ada, Oklahoma and 30 miles to the northeast of Turner Falls in Oklahoma's south central Arbuckle Mountains. The recovered core from the Wyche-1 well ends 2 ft above the Woodford-Hunton unconformity (contact at 212 ft) (Slatt et al., 2010). The name of the borehole is designated the Wyche-1 and is located approximately 500 ft to the east of the easternmost Wyche quarry wall (Figure 2) (Miceli, 2010).

Core recovery of the 210 ft deep Wyche-1 well was 190 ft (90%) and was complemented by a suite of Schlumberger wireline logs including: (1) gamma ray, (2) resistivity, (3) density porosity (DPHI), (4) neutron porosity (NPHI), (5) Combination Magnetic Resonance (CMR), (6) Sonic Scanner (MSIP) (7) Elemental Capture Spectroscopy (ECS), and (8) Formation MicroImager (FMI) (Slatt et al., 2010).


Petrophysicists in the integrated PoroMechanics Institute (iPMI) at the University of Oklahoma immediately preserved sporadic 1 ft intervals throughout the core in non-reactive Mulitherm PG-1 mineral oil so as not to let the shale desiccate before geomechanical experiments could be conducted (Sierra et al., 2010; Slatt et al., 2010; Sierra, 2011). The remaining core that was not placed in mineral oil was then slabbed, as described and evaluated by Nicole Buckner of the University of Oklahoma Reservoir Characterization Institute (Slatt et al., 2010).



2.2 THIN SECTION SAMPLE PREPARATION

Sufficient core sample material was left from geomechanics experimentation in the 120.9 ft (Upper Woodford), 135.7 ft (Middle Woodford), and 145.3 ft (Middle Woodford) intervals to create both extra shale surface polished thin sections for examination under the University of Oklahoma Cameca SX50 electron probe micro-analyzer and standard petrographic "sister" thin sections for examination under a petrographic microscope. Sister thin sections are defined here as two or more thin sections produced from the same sample billet. The thin sections studied in this thesis match the sample intervals of the same depth label (converted into feet from meters) as published in Sierra (2011).


Thin section preparation was done by Greg Vardilos of TPS Enterprises, a professional thin section lab specializing in shale, located in Bellaire, Texas. Thin sections were made by first impregnating sample billets with low viscosity Bisphenol type epoxy resin. The epoxy is dyed blue with Blue Supra powder and a Columbia Blue UV spike. Impregnation of the samples with the epoxy resin was enabled by the use of multiple, simultaneous vacuums followed by the application of 1000 pounds of pressure with nitrogen gas. Traditional petrographic thin sections were ground to a thickness of approximately 30 micrometers with a standard shale polish. Thin sections made for examination under the electron probe micro-analyzer were ground to a thickness of approximately 50 micrometers and then taken to a 2400 grit final surface polish by using progressively finer, fixed-grit, silicon-carbide paper (Vardilos, personal communication, 2010). Samples were mounted to glass slides and left uncovered. Such extensive thin



section preparation procedures were necessary to limit the plucking of clay-sized grains during the rigorous polishing process.

Next, petrographic thin sections were examined and described under a Carl Zeiss Inc. AxioImager petrographic microscope following the method outlined in the Argillaceous Rock Atlas of O'Brien and Slatt (1990). Plane- and cross-polarized light photomicrographs were taken with a Carl Zeiss Inc. AxioCam MRc 5 megapixel digital camera linked to Zeiss AxioVision 4.7.1.0 image analysis software installed on a desktop PC. The optical thin sections were also scanned using a high-resolution Nikon Super Coolscan 4000 ED digital-film scanner to provide a digital image of each sample for documentation and correlation to the results from respective electron microprobe analyses. Because the microprobe thin sections were intentionally made to a thickness of approximately 50 micrometers, to prevent the plucking of fine grains during the rigorous polishing process, traditional plane- and cross-polarized light photomicrographs could not be acquired. However, in the 120.9 ft microprobe thin section, plane-polarized light photomicrographs of translucent quartz grains were taken in order to better understand the grain morphology of pyrite within several dominantly quartz-filled Tasmanites cysts. The extra 20 micrometers of thickness in the 120.9 ft microprobe thin section allowed focus through the quartz grains and examination of the three-dimensional morphologies of pyrite encased in quartz-filled Tasmanites cysts.

The surface polished thin sections required a final preparation step for analysis in the electron probe micro-analyzer. Each sample was first cleaned using 100 percent isopropanol and dried using compressed air. Each sample was then marked six to seven times with 2 millimeter x 1 millimeter fine lines of India Ink along prominent visual



laminations to provide location markers when viewing the samples under the small scale of the electron microprobe. Finally, the samples were coated with an approximately 150Å-thick layer of carbon by vacuum evaporation to provide electrical conductivity when underneath the microprobe's electron beam.

2.3 ELECTRON PROBE MICRO-ANALYZER

The University of Oklahoma electron probe micro-analyzer is a fully computer-automated Cameca SX50 that is equipped with five wavelength dispersive X-ray spectrometers (WDS), an integrated energy-dispersive X-ray analyzer (EDXA), standard scanning electron microscope (SEM) capabilities including both backscattered electron (BSE) and secondary electron (SE) imaging, as well as a cathodoluminescence detector. Although all the probe's capabilities were used in the completion of this study, the primary tools employed were WDS, EDXA, and BSE imaging.

2.4 ENERGY-DISPERSIVE X-RAY ANALYSIS (EDXA)

"The development of the energy-dispersive X-ray spectrometer has made 'easy' X-ray spectrometry available to virtually all types of electron-beam instruments" (Goldstein et al., 1992). The technique works by bombarding a conductive sample with an electron beam, capturing the resulting X-ray photons emanating from the sample with a solid state detector and converting the X-ray photon charge pulses to a voltage through a series of converters and amplifiers for screen display and digital documentation via multi-channel

analysis (Goldstein et al., 1992). "The key to understanding how an energy-dispersive spectrometer (EDS) works is to recognize that each voltage pulse is proportional to the energy of the incoming X-ray photon. The role of the computer X-ray analyzer is to establish this relationship and to present it in a form understandable to the operator" (Goldstein et al., 1992). A schematic of the EDS system modified from Goldstein et al. (1992) is shown in Figure 12.

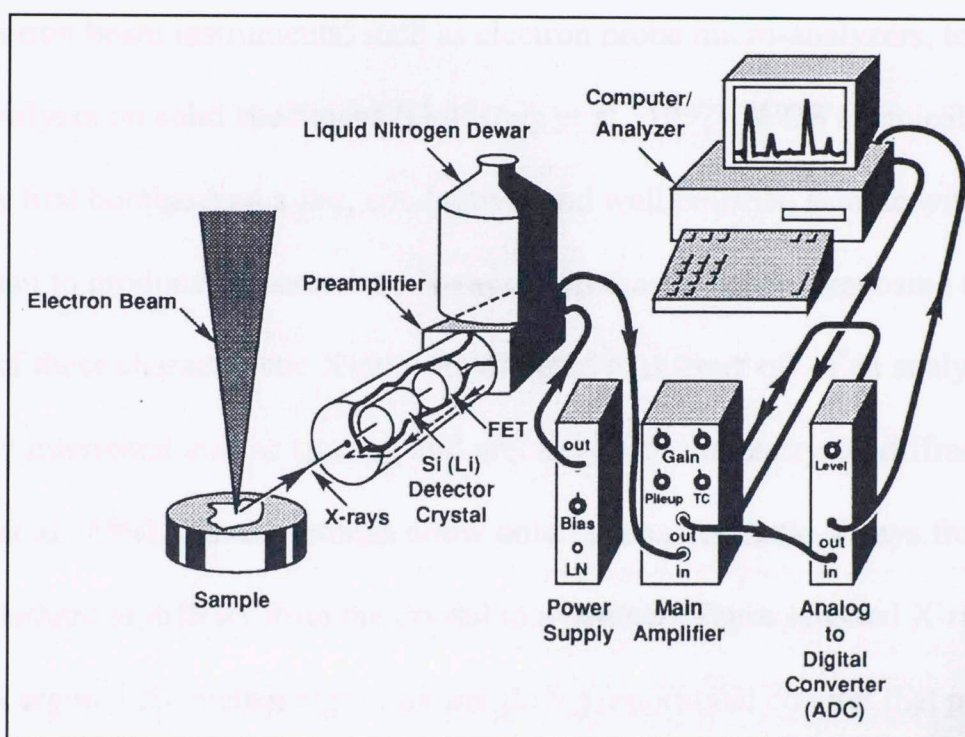



Figure 12. Schematic of the EDS system modified from Goldstein et al., 1992.

Due to the lower statistical accuracy and detection limits of EDXA as compared to that of WDS, EDXA was used primarily for rapid phase identification and semi-quantitative analysis during live-time imaging and exploration sessions. Points of interest were counted with the EDXA detector for thirty seconds and the X-ray energy spectrum produced was converted into relative elemental abundances by the microprobe software. Mineral identification was performed by the probe operator on the basis of elemental




stoichiometry. Beam conditions for EDXA were 20kV acceleration and 20nA sample current; the irradiation area was set by image magnification such that only the phase of interest was irradiated.

2.5 WAVELENGTH DISPERSIVE X-RAY SPECTROSCOPY (WDS)

WDS is an X-ray spectral measurement technique commonly employed on focused electron beam instruments, such as electron probe micro-analyzers, to perform chemical analyses on solid specimens (Goldstein et al., 1992). WDS chemical analysis is achieved by first bombarding a flat, conductive, and well polished sample with an electron beam to produce characteristic X-rays from the elements composing the sample. A fraction of these characteristic X-rays are directed to diffract off of an analyzing crystal with a select interstitial atomic spacing and precisely set sample-crystal diffraction angle (Goldstein et al., 1992). These settings allow only the characteristic X-rays from a particular element to diffract from the crystal to a counter. These selected X-rays then enter a 90% argon-10% methane gas mixture flow-proportional counter that produces photo-electrons upon interaction with the gas mixture, creating charge pulses that can be collected and counted. Compositional analysis is enabled by comparison of the X-ray intensities from samples to those from standard materials of known composition, after corrections are made to account for matrix effects involving atomic number effects, X-ray absorption, and secondary fluorescence (Goldstein et al., 1992).

Elements measured by WDS spot analysis along transect lines in the three sample intervals included: Na, Mg, Al, Si, P, S, K, Ca, Ti, and Fe. All analyses were conducted using an electron beam acceleration of 20 kV, a beam current of 20 nA, a rastered beam




area of 40 micrometers x 40 micrometers, and a counting time of 30 seconds on peak. The beam conditions used were determined based on several pre-analysis calibrations to determine the maximum beam area that could be employed without significant intensity loss due to defocusing of X-rays to the counter. Inconsequential intensity loss along irradiation area edges was confirmed as resulting K numbers remained near 1 and elemental totals equaled 100 ± 1 weight percent for pertinent standards. The 40 micrometer x 40 micrometer beam area employed produced X-rays from a representative sample area that was both greater than the average clay- and silt-sized grains and at least one order of magnitude smaller than the thinnest sample lamination.

Full automation of the Cameca SX50 electron probe micro-analyzer includes the ability to save location points anywhere on a sample to computer memory and return to the same point along both the x and y axes. In the case of this study, WDS point analysis transect lines were created perpendicular to the laminations of each sample with 75 micrometer spacing. Lateral shifts in transect lines were made only if a visible polishing scratch was observed or an India Ink location marker described previously extended into the path selected. Once the elemental X-ray intensities on the standard materials were calibrated and the WDS spot analysis transect lines were saved to computer memory, the automated analysis was instructed to begin.


2.6 BACKSCATTERED ELECTRON (BSE) IMAGING

BSE imaging is a technique used to create gray scale images based upon compositional contrast between materials in a sample under an electron beam. BSE



imaging was a primary tool used for image documentation of the samples in this study. Backscattered electrons are the product of primary beam electrons that collide elastically and ultimately reflect off of near surface atomic nuclei comprising the sample (Krinsley et al., 1998). The fraction of electrons that a given sample will backscatter from the electron beam is dependent on the sample's atomic number; low atomic number materials have larger void spaces between nuclei, which allows for primary beam electrons to penetrate deep into the sample and be absorbed, whereas high atomic number materials provide more obstructions for beam electrons to collide with, causing much greater scattering (Goldstein et al., 1992; Krinsley et al., 1998; Reed, 2005). In a BSE image, the highest density materials (high atomic number) appear in the lightest gray tones, void space and the lowest density materials (low atomic number) appear darkest, and the materials with densities falling in-between the two extremes are distributed in-between, usually on a 256-bin gray scale. BSE imaging is of great value for phase recognition in samples comprised of contrasting density materials, although minerals with similar average atomic numbers or densities produce similar gray scale values (Reed, 2005).

After conducting a WDS analytical transect, BSE images at varying magnifications were acquired throughout the three thin sections to both understand and document the important features: (1) microstratigraphy and rock fabric, (2) authigenic, biogenic, and detrital mineral grains, (3) palynomorphic fossil identification, (4) compositional variations, and (5) relative timing of diagenetic events. A series of 1000 micrometer x 1000 micrometer scaled BSE images were then acquired at every tenth point along a WDS analytical transect line (750 micrometer spacing between adjacent image centers) to create a photomontage for each sample as illustrated by Reed (2005).



The images were stitched together using the Adobe Photoshop CS3 automated photomerge feature and are shown in Appendices I, J, and K for the 120.9 ft, 135.7 ft, and 145.3 ft samples respectively.

2.7 MINERALOGICAL MICRO-LOGGING

The aim of the preceding methodology was to collect quantitative, semi-qualitative, and qualitative data from which sub-100 micrometer scale mineralogy logs could be produced for each sample. These logs were generated by first analyzing the elemental weight percent in transects of WDS point/area analyses and converting them to mineral weight percents by mass balance constrained by the identities and compositions of minerals present in the samples. The mineralogical percentages were then plotted and correlated to both the high-resolution digital thin section scans and BSE image photomontages of the thin sections from which they were generated.

The concentrations obtained by WDS analysis are absolute and not normalized to 100%. Therefore, the results must represent the summation of components in the different minerals present (i.e., sum to 100 weight percent) with the inclusion of any elemental constituents that could not be measured in the analysis: (1) water and (2) carbon (Li and Be are assumed to be in the 10s of ppm level and no minerals were identified in which these elements are essential structural constituents). Water is accounted for by its inclusion in the formulae of hydrous minerals—clay, in this case. Similarly, carbon was not analyzed, but is accounted for by its presence in: (1) the calcite and dolomite formulae, and (2) as organic carbon by difference of the microprobe totals from 100% after accounting for water in clay.

The decision tree used to calculate mineralogy from the WDS elemental analyses began with the clays as the exclusive Al proxy. Performing EDXA on the clay matrices of each sample revealed that illite $\{K_{1-1.5}Al_4[Si_{7-6.5}Al_{1-1.5}O_{20}](OH)_4\}$ was the dominant clay mineral for all three sample intervals. Quartz (SiO_2) was then determined with the remaining silica component as no other major mineral phase incorporated Si. As S is exclusive to pyrite (FeS_2) among the minerals observed, it was used as the proxy for calculating the pyrite phase percentage. Because apatite [$Ca_5(PO_4)_3(OH,F,Cl)$], dolomite ($CaMg(CO_3)_2$), and calcite ($CaCO_3$) all incorporate Ca, these phases were calculated by first sanctioning Ca to apatite proxied by P, second to dolomite proxied by the Mg not incorporated into the clay phase, and last to calcite by using the remaining Ca to proxy for the calcite percentage. The summation of these five mineral phases was then subtracted from 100% to estimate the organic carbon content as WDS analysis of C was not deemed sufficiently accurate. The main source of error in micro-mineralogic logging is therefore included in this organic percentage estimate as minor mineral phases not derived from these calculations and intensity loss due to surface imperfections or voids are incorporated into this final value. Based on this error, organic percentages derived from micro-mineralogy logs are regarded as overestimates.

2.7.1 MICRO-MINERALOGY LOG CALCULATIONS

The Wyche-1, 120.9 ft, 135.7 ft, and 145.3 ft WDS analytical transect line results were output into Microsoft Office Excel spreadsheets for digital documentation and analysis. The procedure for determining mineralogical percentages at each analysis point for the three sample intervals is as follows:

1. Qualitatively determine the dominant clay matrix mineral by EDXA throughout the sample, to decide which clay mineral(s) is/are the dominant clay phase. Illite was found to be the primary clay-matrix mineral in every sample.
2. Calculate the illite-clay $\{K_{1-1.5}Al_4[Si_{7-6.5}Al_{1-1.5}O_{20}](OH)_4\}$ percentage by dividing the aluminum oxide percentage (Al_2O_3) from WDS analysis by the weight fraction of aluminum oxide in a standard illite (from Deer et al., 1985, weight fraction $Al_2O_3 = 18.50 \text{ wt}\% Al_2O_3 / 100.00 \text{ wt}\% = 0.1850$):
$$wt\% Al_2O_3_{WDS} / 0.1850 = \% Illite \dots\dots\dots (Eq. 2.1)$$
3. Calculate the percentage of silica (SiO_2) in the illite-clay matrix by multiplying the clay percentage by the weight fraction of silicon dioxide found in a standard illite (from Deer et al., 1985, weight fraction $SiO_2 = 56.91 \text{ wt}\% SiO_2 / 100.00 \text{ wt}\% = 0.5691$):
$$\% Illite \times 0.5691 = wt\% SiO_2_{clay} \dots\dots\dots (Eq. 2.2)$$
4. Calculate the quartz (SiO_2) percentage by subtracting the $wt\% SiO_2$ in the illite-clay matrix from the $wt\% SiO_2$ from WDS:

$$wt\% SiO_2_{WDS} - wt\% SiO_2_{clay} = \% Quartz \dots\dots\dots (Eq. 2.3)$$

5. Calculate the pyrite (FeS₂) percentage by dividing the wt% S²⁻ from WDS analysis by the weight fraction of S²⁻ in ideal pyrite (= 53.45 wt% S²⁻ / 100.00 wt% = 0.5345):

$$\% S_{WDS}^{2-} / 0.5345 = \% Pyrite \dots \dots \dots (Eq. 2.4)$$

6. Calculate the wt% CaO in apatite by multiplying the wt% P₂O₅ value from WDS by the wt% CaO over wt% P₂O₅ ratio from ideal apatite (= 55.82 wt% CaO / 42.39 wt% P₂O₅ = 1.32):

$$wt\% P_{2O_5} WDS \times (1.32 \text{ wt}\% CaO / wt\% P_{2O_5})_{ideal \text{ apatite}} = wt\% CaO_{apatite} \dots (Eq. 2.5)$$

7. Calculate the apatite [Ca₅(PO₄)₃(OH,F,Cl)] percentage by adding the wt% P₂O₅ value from WDS and the wt% CaO in apatite value:

$$P_{2O_5} WDS + CaO_{apatite} = \% Apatite \dots \dots \dots (Eq. 2.6)$$

8. Calculate the wt% MgO in the illite-clay matrix by multiplying the wt% Al₂O₃ from WDS by the weight fraction of MgO in a standard illite (from Deer et al., 1985, weight fraction MgO = 13.65 wt% MgO / 100.00 wt% = 0.1365):

$$wt\% Al_2O_3 WDS \times 0.1365 = wt\% MgO_{clay} \dots \dots \dots (Eq. 2.7)$$

9. Calculate the wt% MgO in dolomite by subtracting the wt% MgO in the illite-clay matrix from the wt% MgO from WDS. If the calculation yields a negative value, there is no MgO available for dolomite and should be corrected to zero:

$$wt\% MgO_{clay} - wt\% MgO_{WDS} = wt\% MgO_{dolomite} \dots \dots \dots (Eq. 2.8)$$

10. Calculate the wt% CaO available for dolomite by subtracting the wt% CaO in apatite from the wt% CaO from WDS:

$$wt\% CaO_{WDS} - wt\% CaO_{apatite} = wt\% CaO_{available \text{ for dolomite}} \dots \dots \dots (Eq. 2.9)$$

11. Calculate the wt% CaO in dolomite by multiplying the MgO in dolomite by the wt% CaO over wt% MgO ratio found by EDXA in dolomites from each sample interval. For the

$$120.9 \text{ ft sample: } \text{wt}\% \text{ CaO}_{\text{EDXA}} / \text{wt}\% \text{ MgO}_{\text{EDXA}} \text{ ratio} = 30.16 / 13.90 = 2.17;$$

$$135.7 \text{ ft sample: } \text{wt}\% \text{ CaO}_{\text{EDXA}} / \text{wt}\% \text{ MgO}_{\text{EDXA}} \text{ ratio} = 25.25 / 16.18 = 1.56;$$

$$145.3 \text{ ft sample: } \text{wt}\% \text{ CaO}_{\text{EDXA}} / \text{wt}\% \text{ MgO}_{\text{EDXA}} = 31.92 / 19.92 = 1.60;$$

$$\text{wt}\% \text{ MgO}_{\text{dolomite}} \times (\text{wt}\% \text{ CaO}_{\text{EDXA}} / \text{wt}\% \text{ MgO}_{\text{EDXA}}) = \text{wt}\% \text{ CaO}_{\text{dolomite}} \dots \text{(Eq. 2.10)}$$

12. Calculate the wt% CO₂ in dolomite by first summing the mass of CO₂ corresponding to the MgO (as magnesite) and CaO (as calcite) components in dolomite. The wt% of CO₂ in the magnesite component is the wt% MgO in dolomite multiplied by the mass ratio of CO₂ to MgO in ideal dolomite; (44.01 g CO₂ / 40.31 g MgO = 1.09 g CO₂ / g MgO). The wt% of CO₂ in the calcite component is the wt% CaO in dolomite multiplied by the mass ratio of CO₂ to CaO in ideal dolomite; (44.01 g CO₂ / 56.10 g CaO = 0.78 g CO₂ / g CaO):

$$[\text{wt}\% \text{ MgO}_{\text{dolomite}} \times (1.09 \text{ g CO}_2/\text{g MgO})_{\text{ideal dolomite}}] + [\text{wt}\% \text{ CaO}_{\text{dolomite}} \times (0.78 \text{ g CO}_2/\text{g CaO})_{\text{ideal dolomite}}] = \text{wt}\% \text{ CO}_2 \text{ dolomite} \dots \text{(Eq. 2.11)}$$

13. Calculate the dolomite (CaMg(CO₃)₂) percentage by adding the wt% MgO in dolomite with the wt% CaO in dolomite and the wt% CO₂ in dolomite:

$$\text{wt}\% \text{ MgO}_{\text{dolomite}} + \text{wt}\% \text{ CaO}_{\text{dolomite}} + \text{wt}\% \text{ CO}_2 \text{ dolomite} = \% \text{ Dolomite} \dots \text{(Eq. 2.13)}$$

14. Calculate the wt% CaO in calcite by subtracting the wt% CaO in dolomite from the wt% CaO available for dolomite:

$$\text{wt}\% \text{ CaO}_{\text{available for dolomite}} - \text{wt}\% \text{ CaO}_{\text{dolomite}} = \text{wt}\% \text{ CaO}_{\text{calcite}} \dots \text{(Eq. 2.12)}$$

15. Calculate the wt% CO₂ in calcite by multiplying the wt% CaO in calcite by the mass ratio of CO₂ to CaO in ideal calcite; (44.01 g CO₂ / 56.10 g CaO) = (0.78 g CO₂ / g CaO):

$$wt\% CaO_{calcite} \times (0.78 \text{ g } CO_2 / \text{ g CaO})_{ideal \text{ calcite}} \dots \dots \dots (Eq. 2.13)$$

16. Calculate the calcite (CaCO₃) percentage by adding the wt% CaO in calcite with the wt% CO₂ in calcite. If the wt% CaO in calcite is less than zero, there is no calcite and the percentage should be corrected to zero:

$$wt\% CaO_{calcite} + wt\% CO_2_{calcite} = \% Calcite \dots \dots \dots (Eq. 2.14)$$

17. Estimate the percentage of organics by subtracting the summation of the illite-clay, dolomite, calcite, quartz, and pyrite percentages from 100 %:

$$100.00 \% - (\% Illite + \% Dolomite + \% Calcite + \% Quartz + \% Pyrite) = \% Organics \dots \dots \dots (Eq. 2.15)$$

18. Quality control the quantitative percentage of organics with a qualitative gray scale evaluation of corresponding BSE images. As low density organics will appear as black pixels in BSE images, the percentage of black pixels can be calculated with image analysis software and compared to the organic percentage estimated with the micro-mineralogy log calculations. Alternatively, if % TOC data is available, compare the average % Organics value from WDS micro-mineralogy to TOC percentage values obtained from the same sample interval.

19. Finally, a micro-mineralogy log can be plotted and correlated with both the high-resolution digital thin section scan and BSE image photomontage that were discussed earlier in the methodology section.

2.8 X-RAY MAPPING

Elemental X-ray mapping was performed on the 120.9 ft polished microprobe thin section as another semi-quantitative means to characterize the fine-grained mineralogy of the sample focused on understanding relations in a single calcite-clay laminated couplet. Mapping was performed using a combination of WDS and EDXA intensity acquisitions to document elemental distributions in images of an area also captured by BSE imaging. Each element micrograph is a gray-scale intensity map of fluorescent X-ray intensity where a black pixel represents zero counts and the brightest pixel in the frame corresponds to the highest count rate detected.

X-ray intensity maps were setup by assigning the area to be analyzed, the desired image resolution (in pixels), the dwell time (counting time) to be used per pixel in the area, and the desired elements to be analyzed. Table 1 shows the parameters used for the X-ray intensity map acquired.

Table 1. Acquisition settings for the 120.9 ft calcite-clay X-ray intensity map analysis.

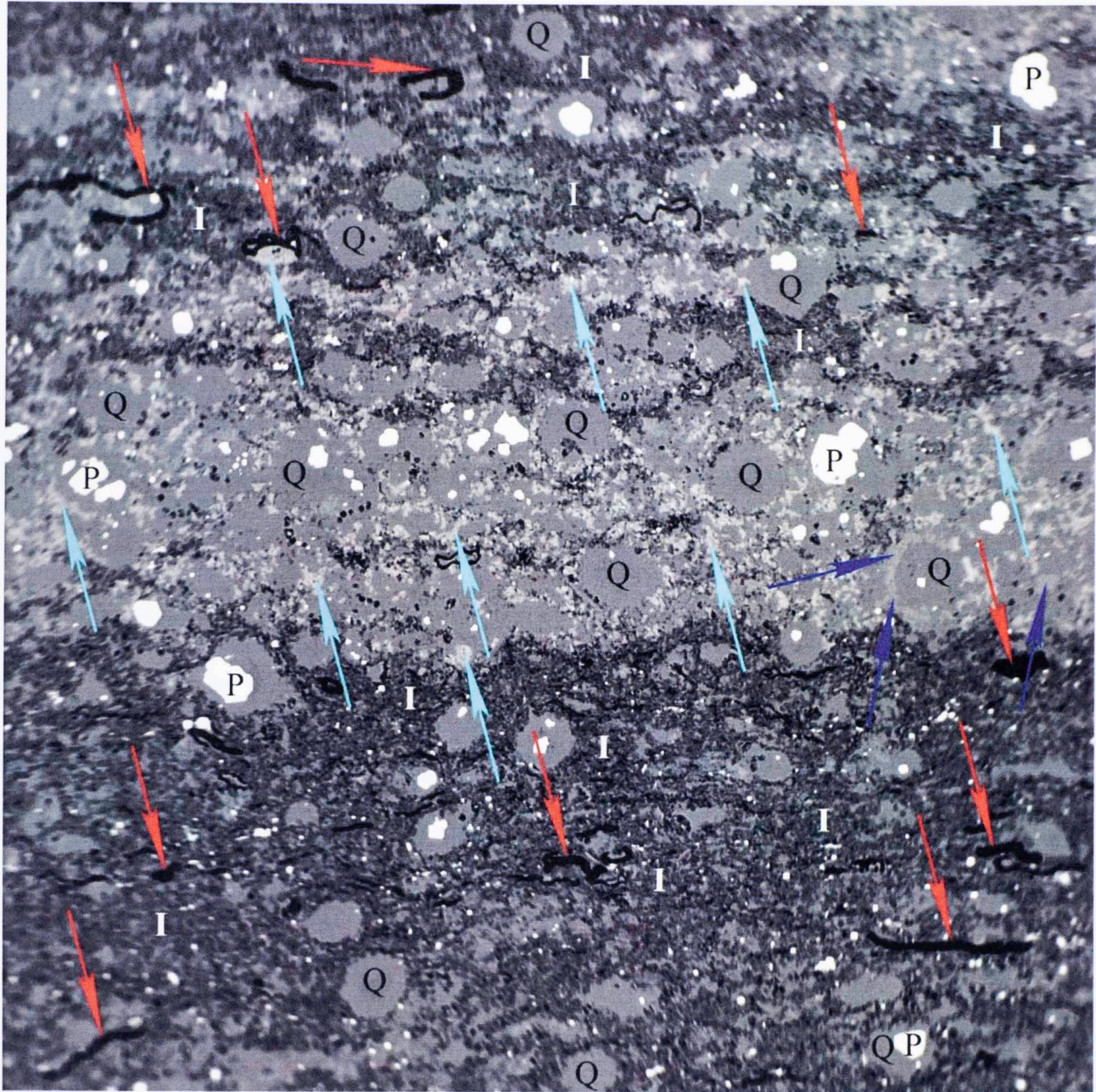
Analysis Area ($\mu\text{m} \times \mu\text{m}$)	Resolution (px x px)	Pixel Area ($\mu\text{m} \times \mu\text{m}$)	Dwell Time (μsec)	WDS elements	EDXA elements
1580 x 1580	512 x 512	3 x 3	0.2	Ca, Mg, K, Na, Fe	Al, Si, S, O

Even though the area analyzed (1.6 mm x 1.6 mm) is quite small, analyses can take several hours as each individual pixel is extremely small (3 μm x 3 μm). Thus, for the single X-ray intensity mapping analysis performed in this thesis, the combined number of pixels and counting time applied per pixel generated the maps in approximately 15 hours.

3. RESULTS

3.1 PETROGRAPHIC AND MICROPROBE THIN SECTION IMAGING AND DESCRIPTION

Samples were first evaluated by means of petrographic thin sections and a light microscope. Each thin section was initially scanned with a Nikon Super Coolscan 4000 ED digital-film scanner. Microscope images were then captured with a Carl Zeiss Inc. AxioCam MRc 5 megapixel digital camera mounted on a Carl Zeiss Inc. AxioImager Z1 petrographic microscope and recorded with the Carl Zeiss Inc. AxioVision 4.7.1.0 image-analysis software on a desktop PC. The carbon coated, polished thin sections were then analyzed by electron microprobe and the resulting BSE images were coupled with the petrographic micrographs of similar features for comparison and evaluation. Figure 13 is a BSE image annotated to act as a legend for how prominent mineral phases appear in the gray-scale BSE images throughout this thesis. Note that denser mineral phases appear as increasingly brighter gray-scale tones and less dense mineral phases appear as increasingly darker gray-scale tones. Organics, pore space, and plucked mineral grain locations due to polishing appear black.



→ Organics → Dolomite → Calcite
 Q = Quartz P = Pyrite **I** = Illite Clay Matrix

Figure 13. BSE image annotated to illustrate the characteristic gray-scale tones assigned to prominent mineral phases observed with BSE images throughout this thesis. Note that denser mineral phases appear as increasingly brighter gray-scale tones and less dense mineral phases appear as increasingly darker gray-scale tones. Organics, pore space, and plucked mineral grain locations due to polishing appear black. Dolomite grains will be an intermediate gray-scale tone between darker quartz and brighter calcite. Care must be taken when identifying dolomite as its gray-scale tone is very similar to that of quartz.

3.1.1 120.9 FT PETROGRAPHIC AND MICROPROBE THIN SECTIONS

The Wyche-1, 120.9 ft sample is located at the base of the Upper Woodford Shale unit and is characterized by alternating dark reddish-brown illite-clay and gray to white calcite-cemented silica lamina (Figure 14). It is a distinctly laminated sample even when viewed macroscopically. Illite-clay layers (darker laminations) contain many liptinite macerals that range from fully-compacted, partially-compacted, to non-compacted circles, half-circles and elongate shapes that are derived from the organic walls of *Tasmanites* algal cysts. The partially-compacted to circular liptinite macerals are filled with diagenetic quartz and less often with pyrite. A combination of both quartz- and pyrite-filled *Tasmanites* cysts are most commonly observed. Many of the partially-compressed, quartz-filled *Tasmanites* cysts exhibit a colloform texture along their outer rim. Pyrite contained within quartz-filled *Tasmanites* cysts is typically euhedral and sometimes shows cubic morphology. Pyrite that dominantly fills a *Tasmanites* cyst is typically anhedral and conforms smoothly to the organic cyst wall. *Tasmanites* cysts are found either with their organic walls intact, replaced by secondary silica, or absent. Small authigenic pyrite framboids are also disseminated throughout the clay matrix. Very minor amounts of fine, blood-red, organic-rich phosphate grains are dispersed sporadically throughout the clay as well. Clay content decreases as the presence of quartz-filled *Tasmanites* cysts increase from bottom to top. The diameter of *Tasmanites* cysts range from 50 micrometers to 200 micrometers and the largest are found exclusively in the clay matrix. Small detrital quartz grains are also disseminated in the clay matrix. Overall, the proportion of diagenetic and detrital quartz increase from the bottom to the top of the thin section. Thin, dark-brown organic stringers of unknown origin are also found

disseminated throughout the clay matrix. These organic stingers are not speculated to be Tasmanites cysts as they appear to be more easily compacted and biodegraded as compared to the more robust and organically preserved Tasmanites cyst organic walls.

Calcite-cemented laminations are generally packed with small- to moderate-sized Tasmanites grains. Liptinite maceral content is much less abundant in the calcite laminations and where present, have generally wavy and compact morphologies. Calcite laminations increase in frequency and thickness from the bottom to the top of the thin section. Individual calcite laminations generally present flat bases with gradually, decreasing calcite grain size into non-calcareous clay laminations above.



Figure 14. Pyrite-1 well. Photomicrograph of section through section.

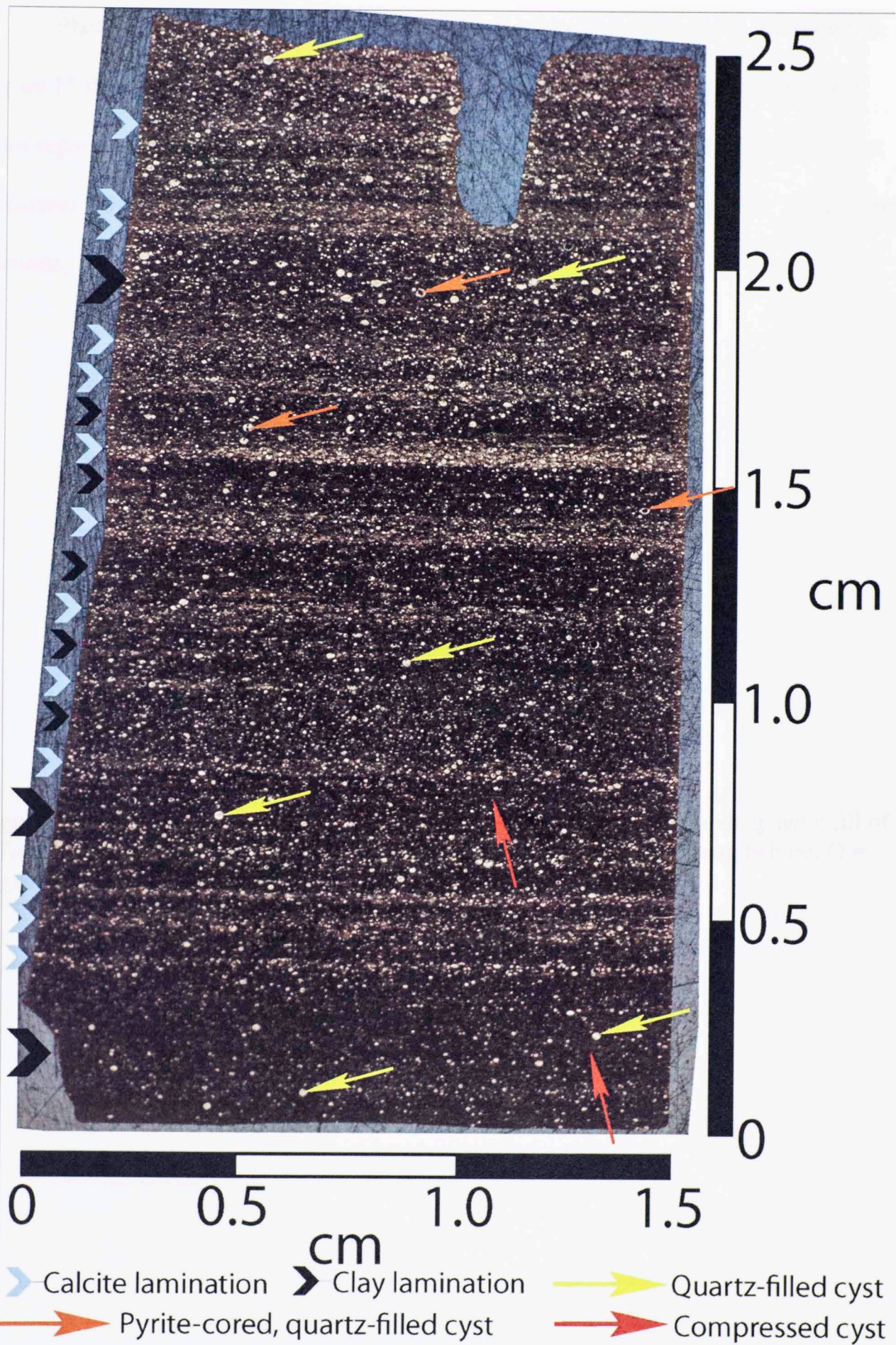


Figure 14. Wyche-1 well, Woodford 120.9 ft petrographic thin section.

Photomicrographs and BSE images of the features described above are shown in Figure 15 through Figure 25. Note that photomicrographs and BSE images were taken from separate thin section samples so when paired, they are not showing the same exact feature(s), but comparable features between the petrographic and microprobe "sister" thin sections.

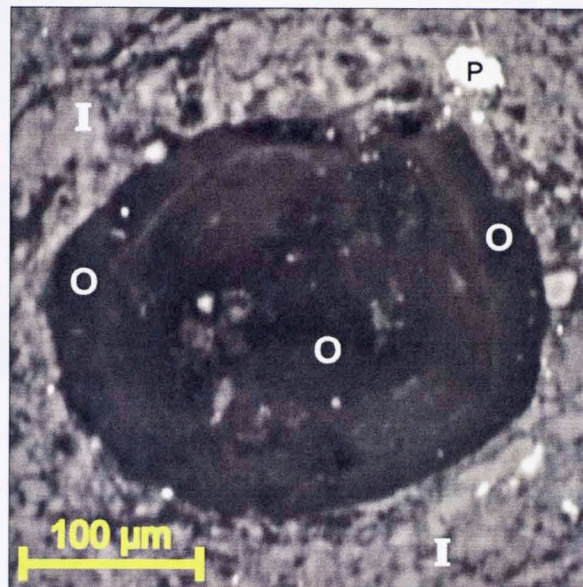


Figure 15. BSE image from the 120.9 ft thin section showing where the diagenetic fill of a Tasmanites cyst plucked out during polishing, leaving its lignite coating behind. O = organic wall, P = pyrite, I = illite.

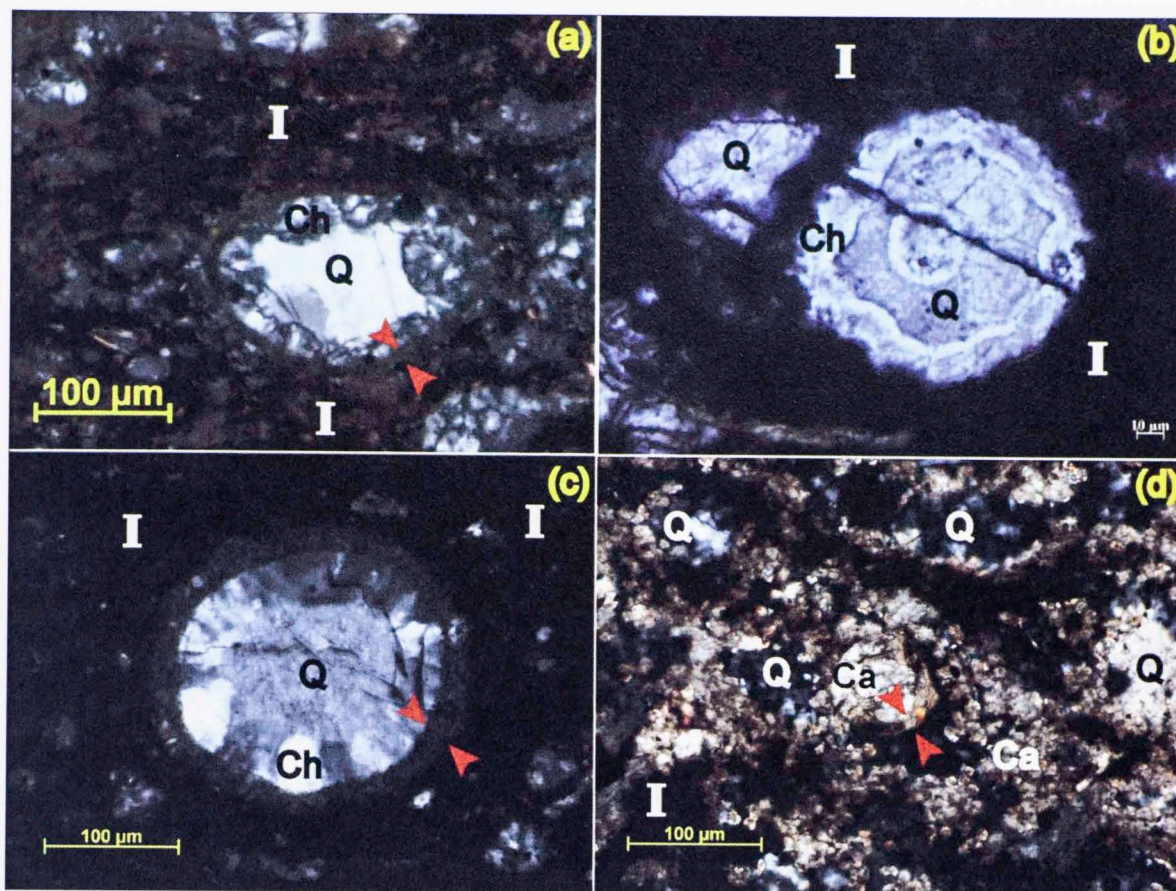


Figure 16. Photomicrographs taken from the 120.9 ft petrographic thin section sample showing the different diagenetic quartz precipitation patterns within Tasmanites cysts. I = illite, Q = quartz, Ch = Chalcedony, and red arrows exhibit the boundaries of preserved Tasmanites cyst organic walls. (a) Photomicrograph (XPL) of a semi-compacted Tasmanites cyst filled with a chalcedony rim on the inner wall of the cyst and the central portion filled with macro-quartz. Differential compaction is observed around the grain. (b) Photomicrograph (PPL) of a spherical Tasmanites cyst (circular) showing a chalcedony rim with colloform texture, a macro-quartz center, and a possible growth ring in the center. (c) Photomicrograph (XPL) of a spherical Tasmanites cyst (circular) showing an organic outer wall, a thick chalcedony rim, and a single-grain quartz center. Although dark in this image, the illite-clay is differentially compacted around the grain. (d) Photomicrograph (XPL) within a calcite lamination showing a 50 μm in diameter, fully-compacted Tasmanites cyst in which calcite has filled the outside of the compacted area to form a circle in thin section. Other comparably sized, quartz-filled Tasmanites cysts, with no organic walls present, are cemented by accumulations of 10 μm in diameter circular calcite grains.

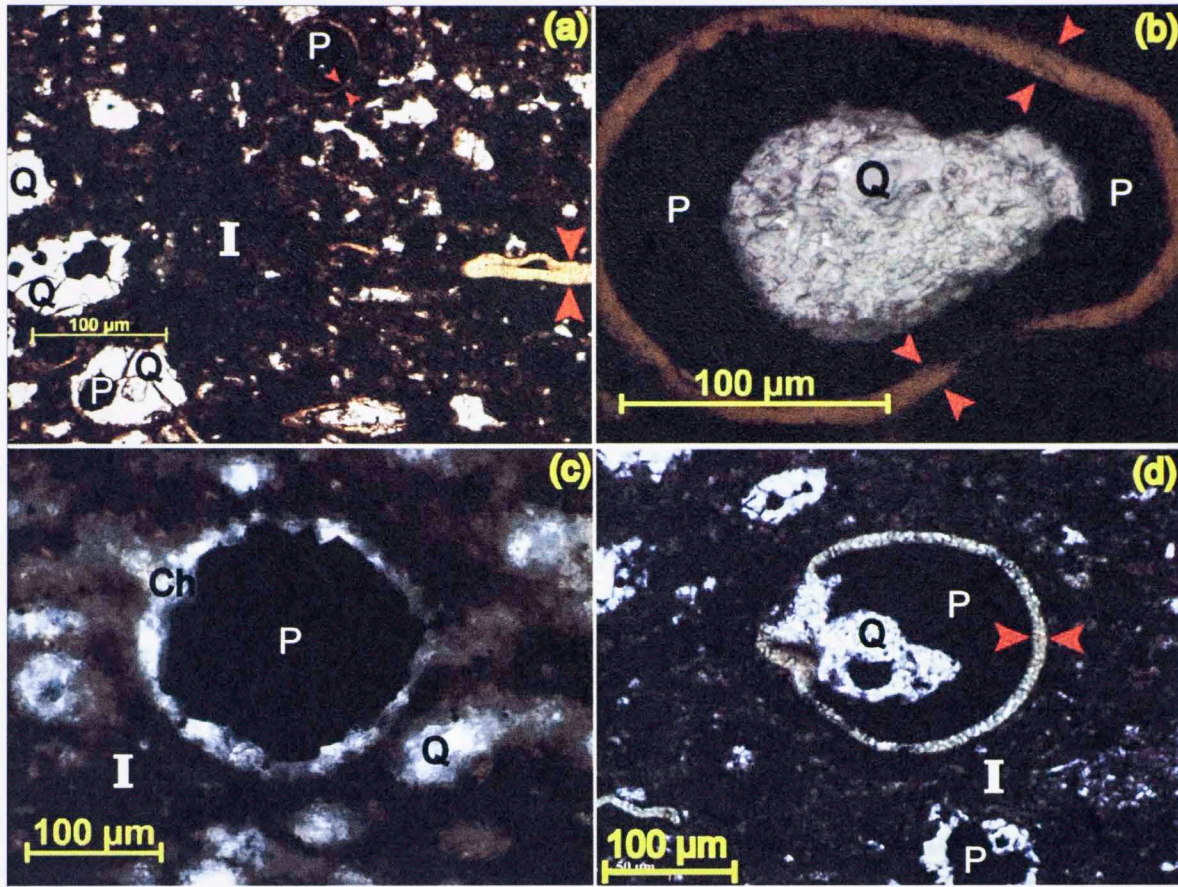


Figure 17. Photomicrographs taken from the 120.9 ft petrographic thin section sample showing the different diagenetic-pyrite precipitation patterns within Tasmanites cysts. I = illite, P = pyrite, Q = quartz, Ch = Chalcedony, and red arrows exhibit the boundaries of preserved Tasmanites cyst organic walls. (a) Photomicrograph (PPL) of a clay lamination showing a spherical pyrite (circular in thin section) wrapped by a Tasmanites cyst organic wall (top), semi-compacted quartz filled Tasmanites cysts lacking their organic walls with some euhedral-pyrite growth within (left), a semi-compacted quartz-filled Tasmanites cyst with a preserved organic wall (bottom), and a fully-compacted cyst (right). (b) Photomicrograph (PPL) of a semi-compacted Tasmanites cyst with a preserved organic wall, pyrite rim, and quartz core. (c) Photomicrograph (XPL) of a Tasmanites cyst that lacks its organic wall, exhibits an outer rim of chalcedony, and a dominant core of massed euhedral-pyrite growth. (d) Photomicrograph (PPL) of a Tasmanites cyst with a preserved organic wall, a near-spherical fill (circular) of the volume by pyrite, and precipitation of quartz where a rupture in the cyst wall occurred.

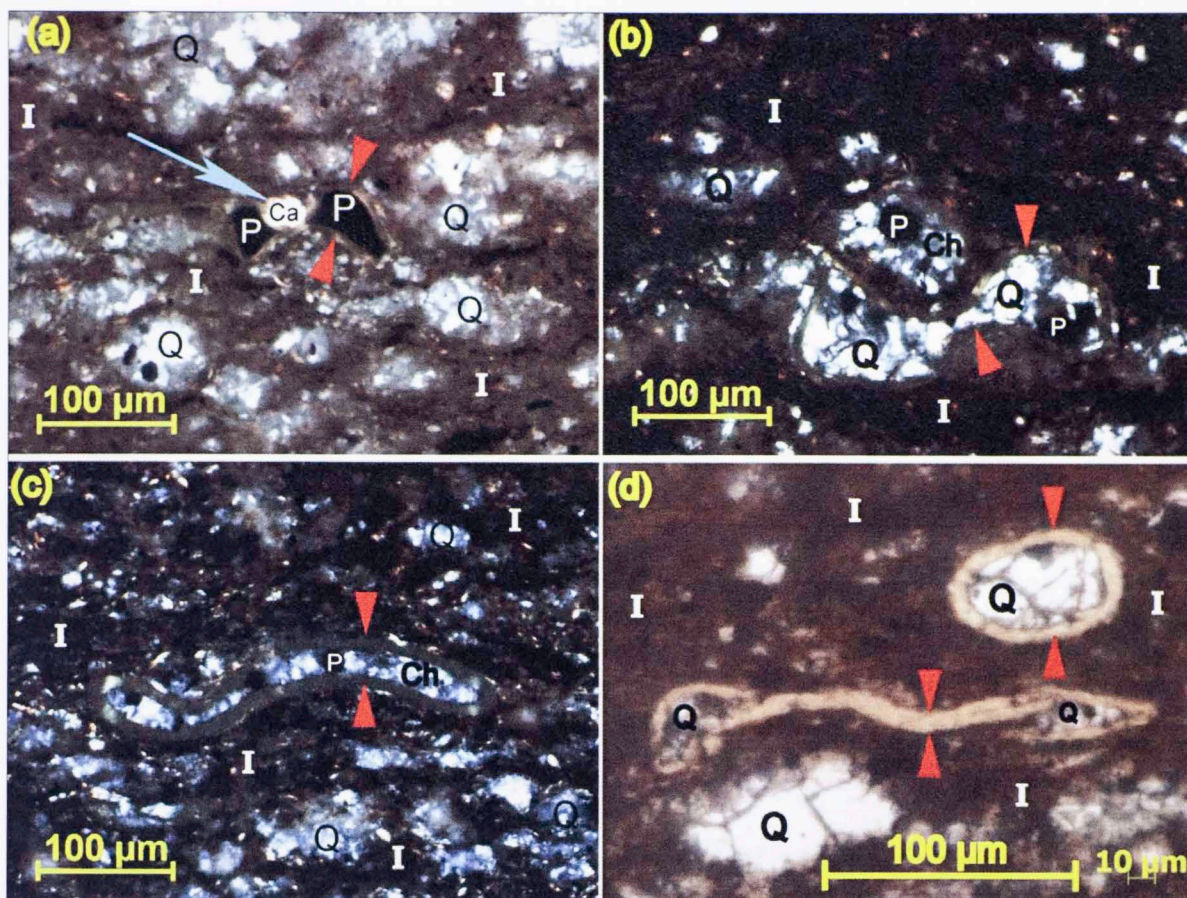


Figure 18. Photomicrographs taken from the 120.9 ft petrographic thin section sample showing the different compaction patterns among Tasmanites cysts. I = illite, P = pyrite, Q = quartz, Ch = Chalcedony, Ca = Calcite, and red arrows exhibit the boundaries of preserved Tasmanites cyst organic walls. Chalcedony was identified in XPL as cryptocrystalline textures could be observed when rotating the stage. (a) Photomicrograph (XPL) of a pyrite-filled, H-shaped, compacted Tasmanites cyst with a preserved organic wall. A detrital calcite grain appears to have compacted the center before diagenetic pyritization occurred and is marked by a light-blue arrow. Quartz-filled Tasmanites cysts are also present and the differential compaction of the illite-clay matrix is readily seen. (b) Photomicrograph (XPL) of a quartz-filled, H-shaped, compacted Tasmanites cyst with a preserved organic wall. Another more spherical (circular) quartz-filled Tasmanites cyst appears to have compacted the underlying cyst before diagenetic precipitation of quartz could preserve the original shape of the cyst. Pyrite growths within the Tasmanites cysts and differential compaction of the illite-clay matrix can also be seen. (c) Photomicrograph (XPL) of a wavy, well-compacted Tasmanites cyst with a preserved organic wall and chalcedony-filled inner space. (d) Photomicrograph (PPL) of a fully-compacted and a semi-compacted Tasmanites cyst. The spaces within the cysts have been filled by diagenetic quartz.

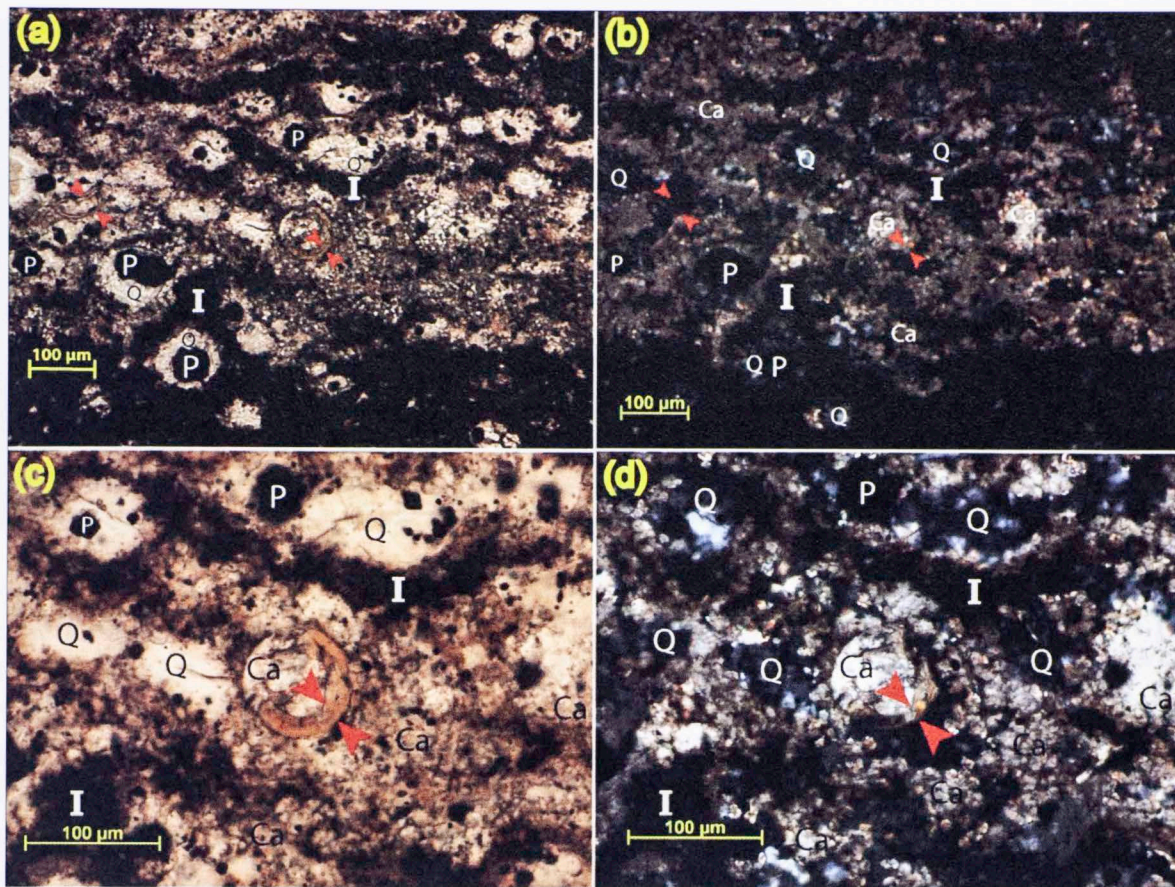


Figure 19. Photomicrographs taken from the 120.9 ft petrographic thin section sample showing calcite cementation patterns within a calcite lamination. I = illite, P = pyrite, Q = quartz, Ca = Calcite, and red arrows exhibit the boundaries of preserved Tasmanites cyst organic walls. (a) Photomicrograph (PPL) of a calcite lamination. Notice the fully compacted Tasmanites cyst in the center of the image. Calcite and quartz are hard to differentiate as the picture was taken in plane polarized light. (b) Photomicrograph (XPL) of the same calcite lamination, however, the image was taken in cross polarized light showing definite visual differences between the calcite and quartz mineral phases. (c) Photomicrograph (PPL) showing a higher magnification focused at the center of image a. The fully-compacted nature of the cyst shown in Figure 19a and b is easily observed here. (d) Photomicrograph (XPL) showing a higher magnification, focused at the center, of Figure 19b. This image shows the morphology and cementation behavior of the calcite better than Figure 19a,b, or c.

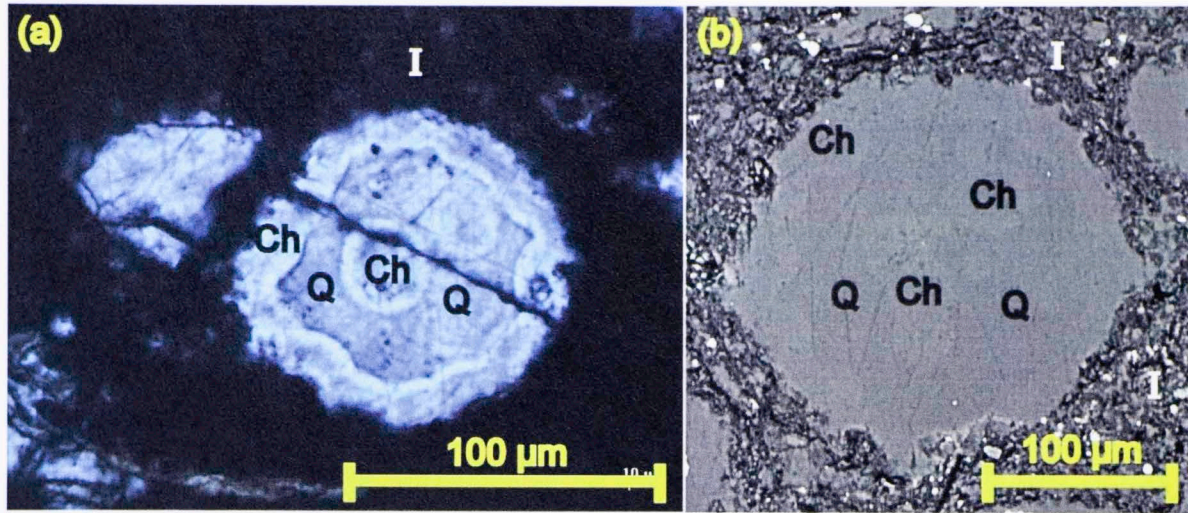


Figure 20. (a) Photomicrograph (PPL) taken from the 120.9 ft petrographic thin section coupled with (b) a BSE image taken from the 120.9 ft polished microprobe thin section showing spherical (circular), quartz-filled Tasmanites cysts. I = illite, P = pyrite, Q = quartz, Ch = chalcedony, and red arrows exhibit the boundaries of preserved Tasmanites cyst organic walls. In BSE images, most quartz filled Tasmanites spheres show a denser rim (brighter) with colloform texture and a slightly less dense inner core (darker). This denser rim is chalcedony and the less dense core is macro- to single-grain quartz.

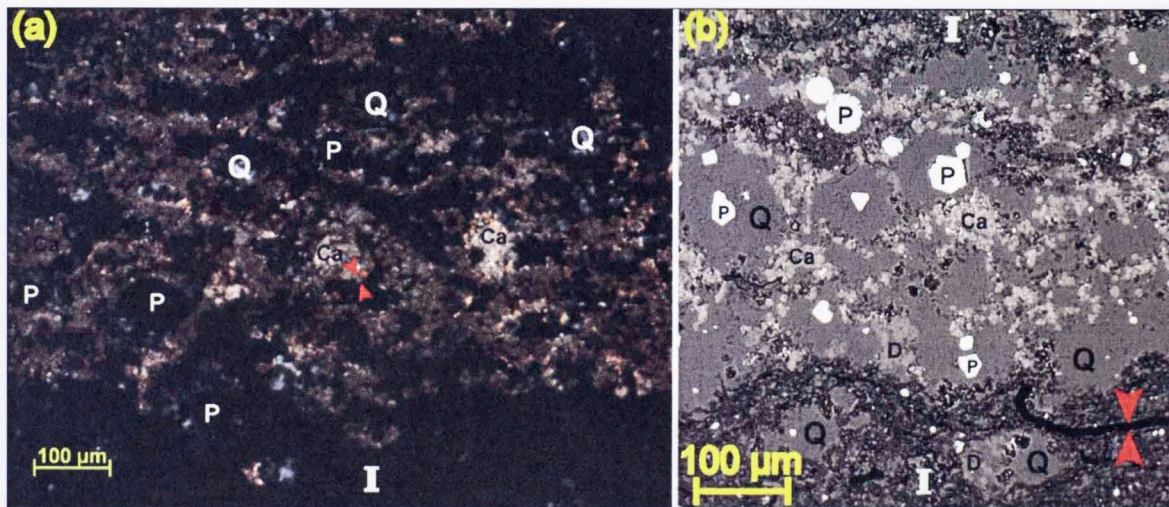


Figure 21. (a) Photomicrograph (XPL) taken from the 120.9 ft petrographic thin section coupled with (b) a BSE image taken from the 120.9 ft polished microprobe thin section showing calcite laminations. I = illite, P = pyrite, Q = quartz, Ca = Calcite, D = dolomite, and red arrows exhibit the boundaries of preserved Tasmanites cyst organic walls.

boundaries of preserved Tasmanites cyst organic walls. This texture is determined by a combination of underlying and overlying grain growth and change between magmatic precipitation of mineral assemblage of diagenesis.

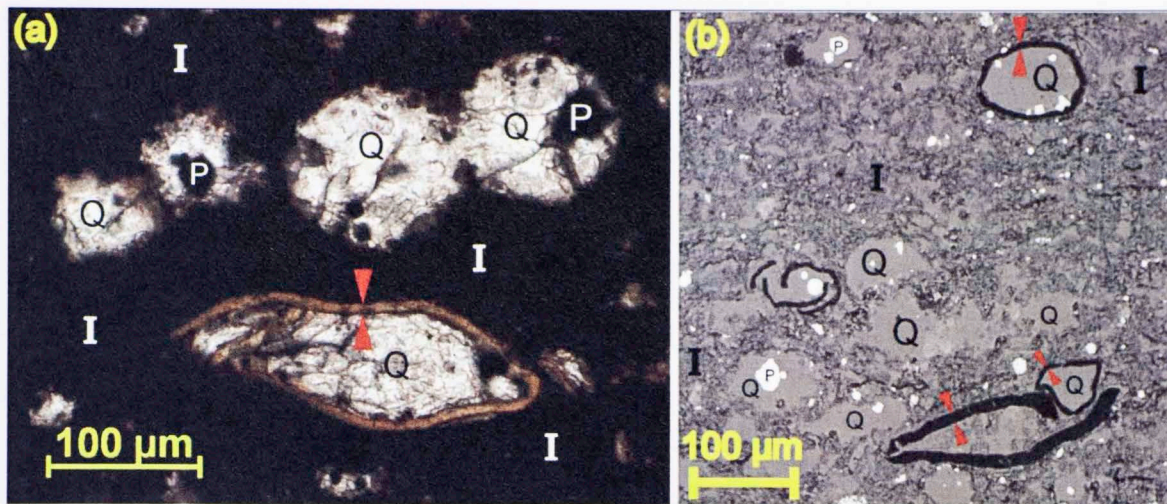


Figure 22. (a) Photomicrograph (PPL) taken from the 120.9 ft petrographic thin section coupled with (b) a BSE image taken from the 120.9 ft polished microprobe thin section showing quartz-filled, partially-compacted Tasmanites cysts with preserved organic walls. I = illite, P = pyrite, Q = quartz, and red arrows exhibit the boundaries of preserved Tasmanites cysts organic walls. The small euhedral-pyrite grains seen within the dominantly quartz-filled cysts is the most common diagenetic filling pattern seen throughout the sample with regard to filled Tasmanites cysts.

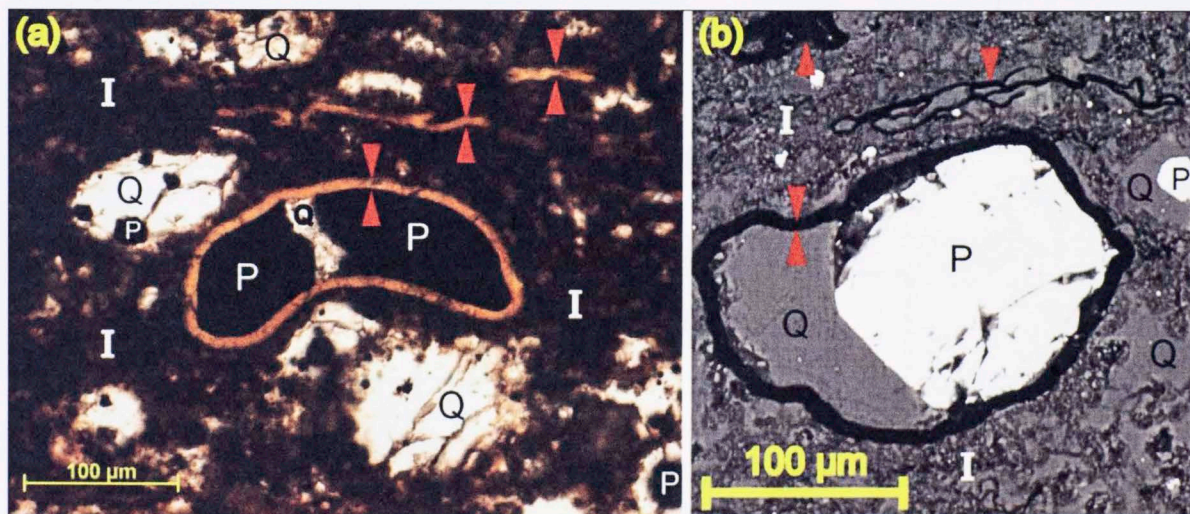


Figure 23. (a) Photomicrograph (PPL) taken from the 120.9 ft petrographic thin section coupled with (b) a BSE image taken from the 120.9 ft polished microprobe thin section showing dominantly pyrite-filled, lobate Tasmanites cysts with a minor amount of precipitated quartz. I = illite, P = pyrite, Q = quartz, and red arrows exhibit the boundaries of preserved Tasmanites cysts organic walls. The final shape is determined by a combination of underlying and overlying grains as well as the timing between diagenetic precipitation of minerals and rate of deposition.

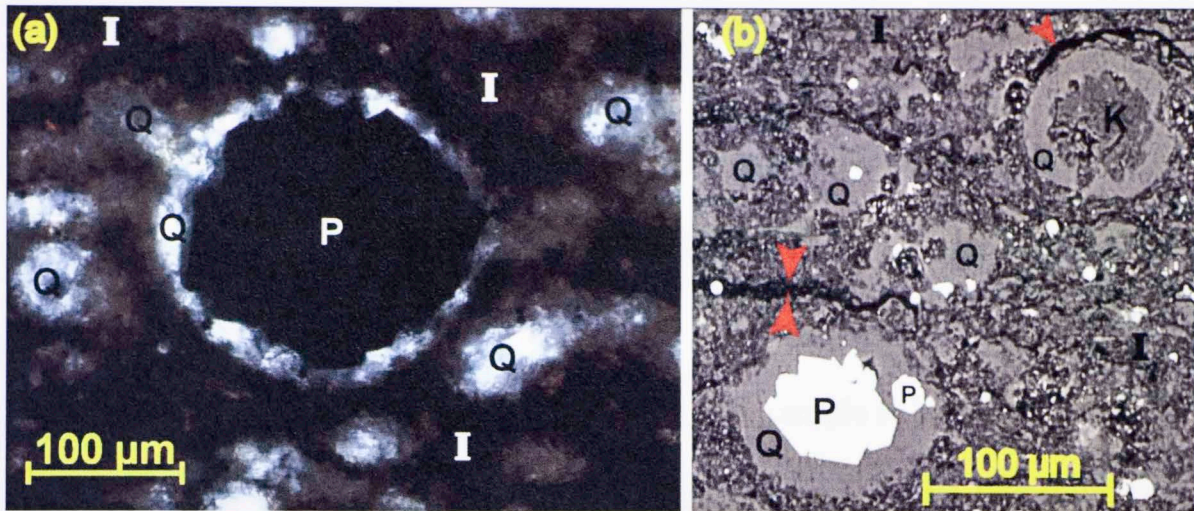


Figure 24. (a) Photomicrograph (XPL) taken from the 120.9 ft petrographic thin section coupled with (b) a BSE image taken from the 120.9 ft polished microprobe thin section showing spherical (circular), euhedral-pyrite filled, quartz-rimmed Tasmanites cysts that lack a preserved organic wall. I = illite, P = pyrite, Q = quartz, K = kaolinite, and red arrows exhibit the boundaries of organic stringers. Note the kaolinite filled Tasmanites cyst with a quartz rim in the upper left.

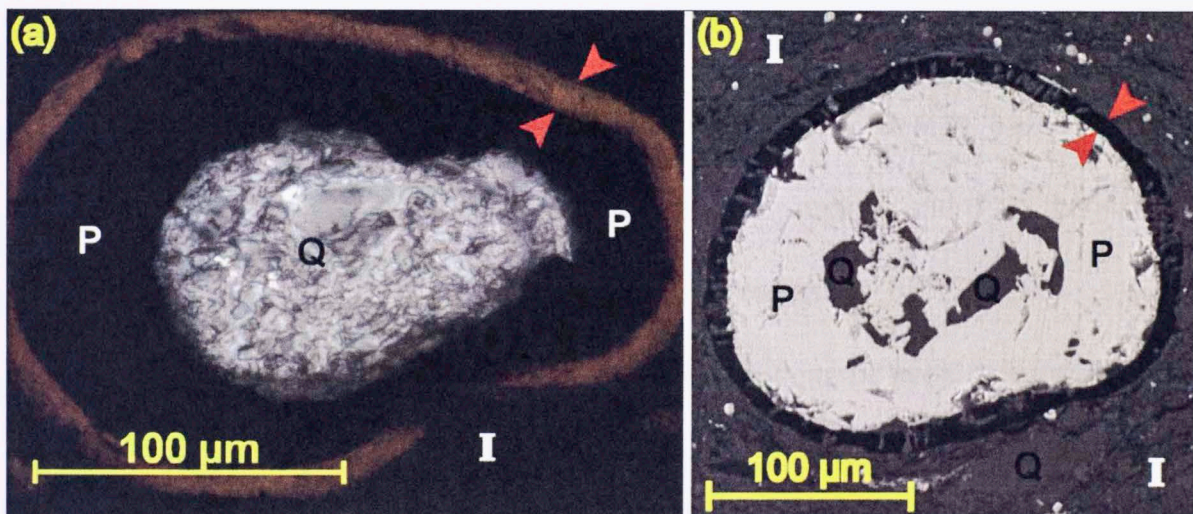


Figure 25. (a) Photomicrograph (PPL) taken from the 120.9 ft petrographic thin section coupled with (b) a BSE image taken from the 120.9 ft polished microprobe thin section showing semi-compacted, dominantly pyrite-filled with quartz-core Tasmanites cysts. I = illite, P = pyrite, Q = quartz, and red arrows exhibit the boundaries of preserved Tasmanites cyst organic walls. Note the very fine quartz that precipitated in the organic wall of the Tasmanites cyst. These are thought to be pore spaces of the organic-cyst wall that have filled with quartz.

3.1.2 135.7 FT PETROGRAPHIC AND MICROPROBE THIN SECTIONS

The Wyche-1, 135.7 ft petrographic thin section shown in Figure 26 is characterized as a mixed dolomitic-argillaceous mudstone that is dominated by a dark reddish-brown illite-clay matrix with 10 micrometer to 50 micrometer diameter detrital dolomite and quartz grains disseminated throughout. The sample is located in the Middle Woodford unit and is approximately 13 feet beneath the Upper-Middle Woodford contact. Rare laminations that appear in the sample interval are generally 100 micrometers in thickness and are not laterally continuous. Detrital-rhombic dolomite is the dominant silt-sized grain in the matrix. Detrital dolomite grains range from finer grains in the base and top of the sample interval to coarser grains in the middle. Detrital quartz is present, but generally much finer than the dolomite. Pyrite framboids are also disseminated throughout the matrix and range from a few to 100 micrometers in size. Sub-10 micrometer pyrite grains are abundant throughout the thin section and three 1 millimeter thick zones of coarser, euhedral pyrite are easily observed in the 135.7 ft BSE photomontage (Appendix L). A few, subtle color changes can be seen macroscopically and are most likely due to increases and decreases in dark-brown to opaque organic stringers of unknown origin. Flat, thin-walled, compacted, light brownish-yellow Tasmanites cysts are present, but are less abundant than dark-brown to opaque organic stringers. Chert lenses resembling compacted Tasmanites cysts are prominent throughout the sample. A very small layer (less than 1 millimeter) of quartz- and pyrite-filled Tasmanites cysts can be seen at the very top of the sample. A few fine, blood-red, organic-rich phosphate grains as well as a few 20 to 40 micrometer long, rectangular, bright white, detrital apatite grains occur sporadically throughout the clay matrix.

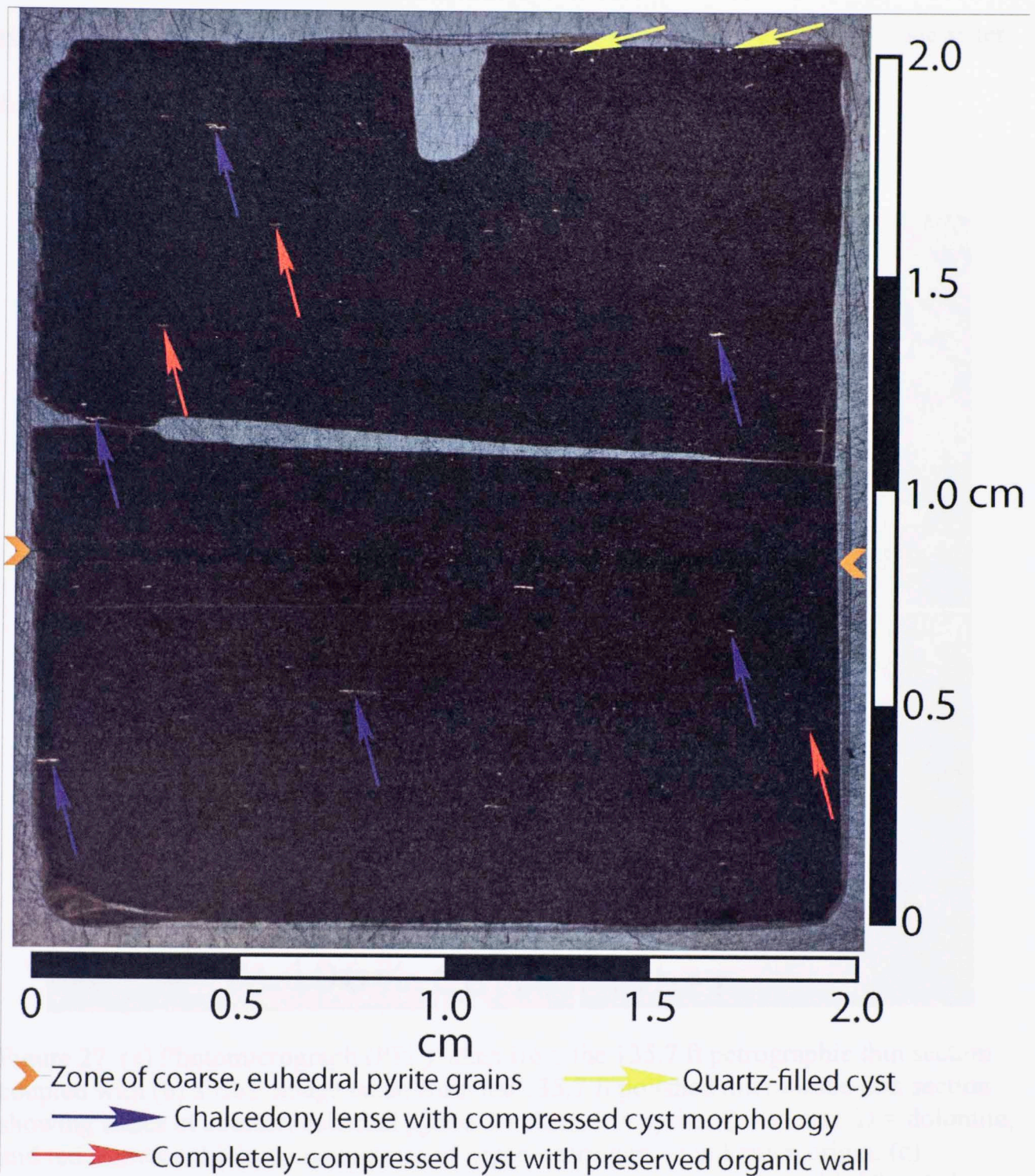


Figure 26. Wyche-1 well, Woodford 135.7 ft petrographic thin section.

Photomicrographs and BSE images of the features described above are shown in Figure 27, Figure 28, and Figure 29. Note that photomicrographs and BSE images were taken from separate thin section samples so when paired, they are not showing the same

exact feature(s), but comparable features between the petrographic and microprobe sister thin sections.

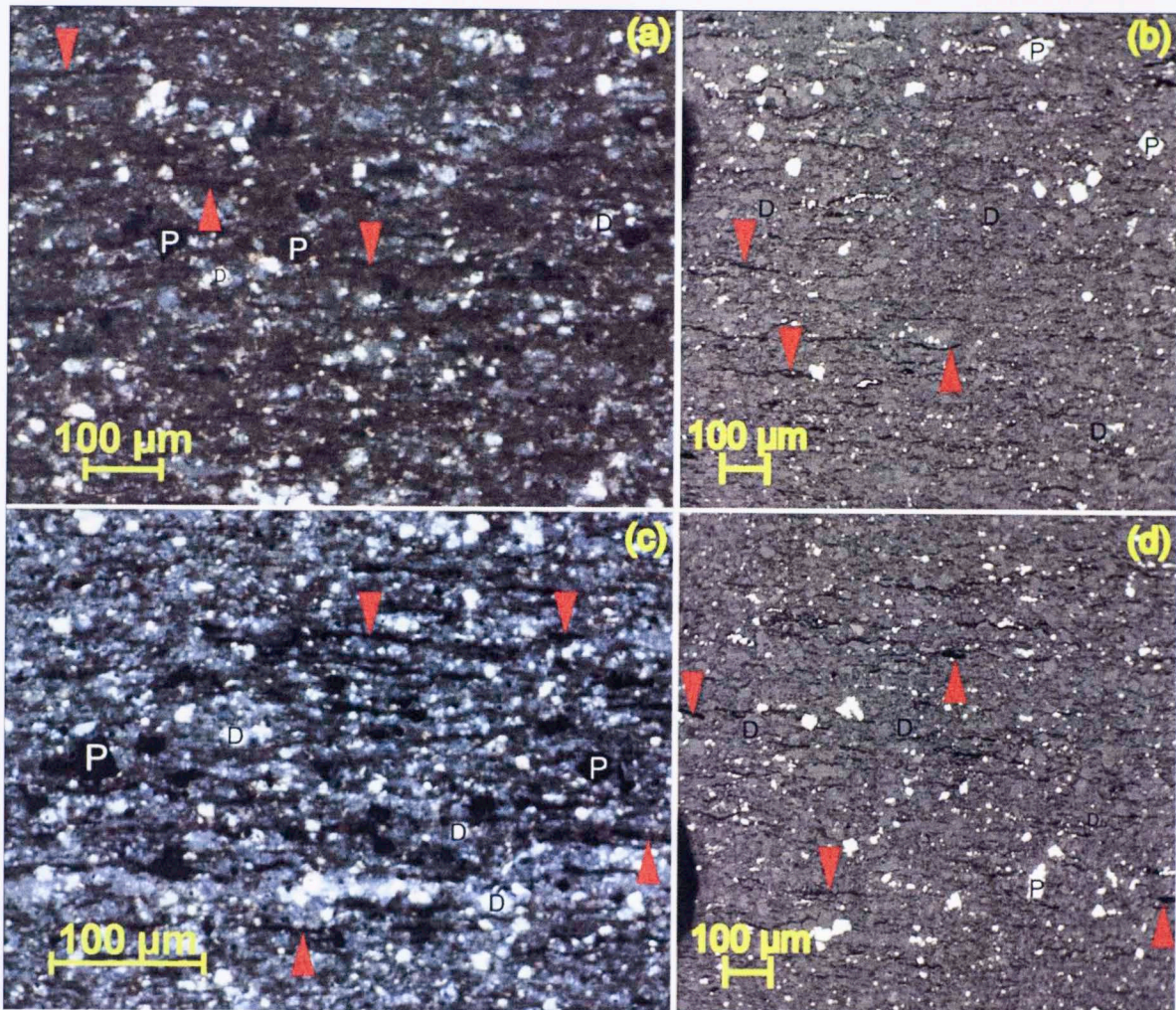


Figure 27. (a) Photomicrograph (PPL) taken from the 135.7 ft petrographic thin section coupled with (b) a BSE image taken from the 135.7 ft polished microprobe thin section showing zones of coarser, euhedral pyrite. I = illite, P = pyrite, Q = quartz, D = dolomite, and red arrows exhibit the boundaries of organic stringers of unknown origin. (c) Photomicrograph (XPL) of a zone of coarser, euhedral pyrite coupled with (d) a BSE image of a comparable pyrite zone from the microprobe polished thin section.

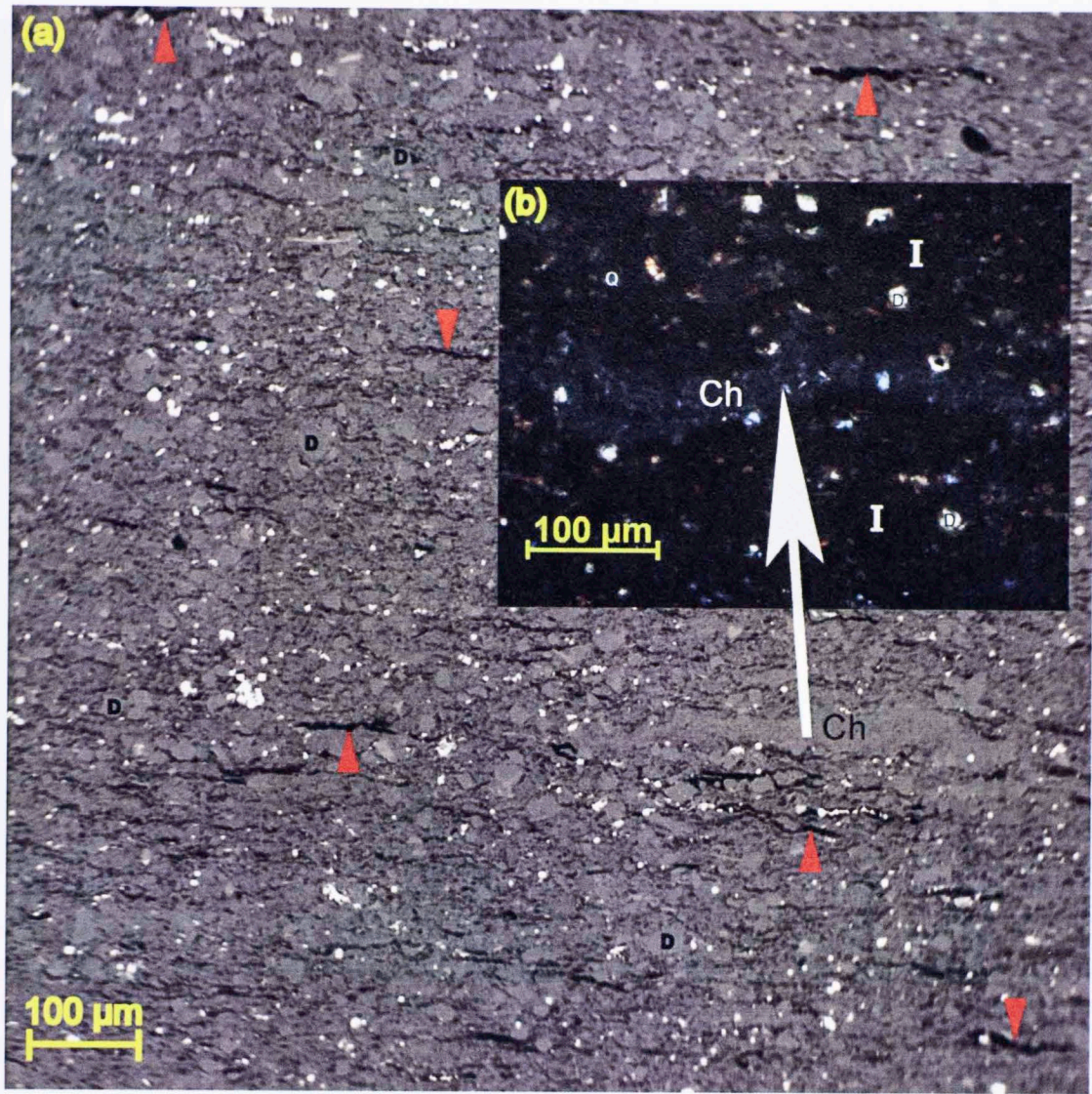


Figure
shows
found
around

(1)
small

Figure 28. (a) BSE image taken from the 135.7 ft polished microprobe thin section coupled with (b) a photomicrograph (XPL) taken from the 135.7 ft petrographic thin section showing what is speculated to be the morphologies of compacted Tasmanites algal cysts that have been completely replaced by chalcedony. The BSE image also shows the overall, generally homogenous looking rock fabric of the 135.7 ft thin section interval. I = illite, P = pyrite, Q = quartz, Ch = chalcedony, D = dolomite, and red arrows exhibit the boundaries of organic stringers.

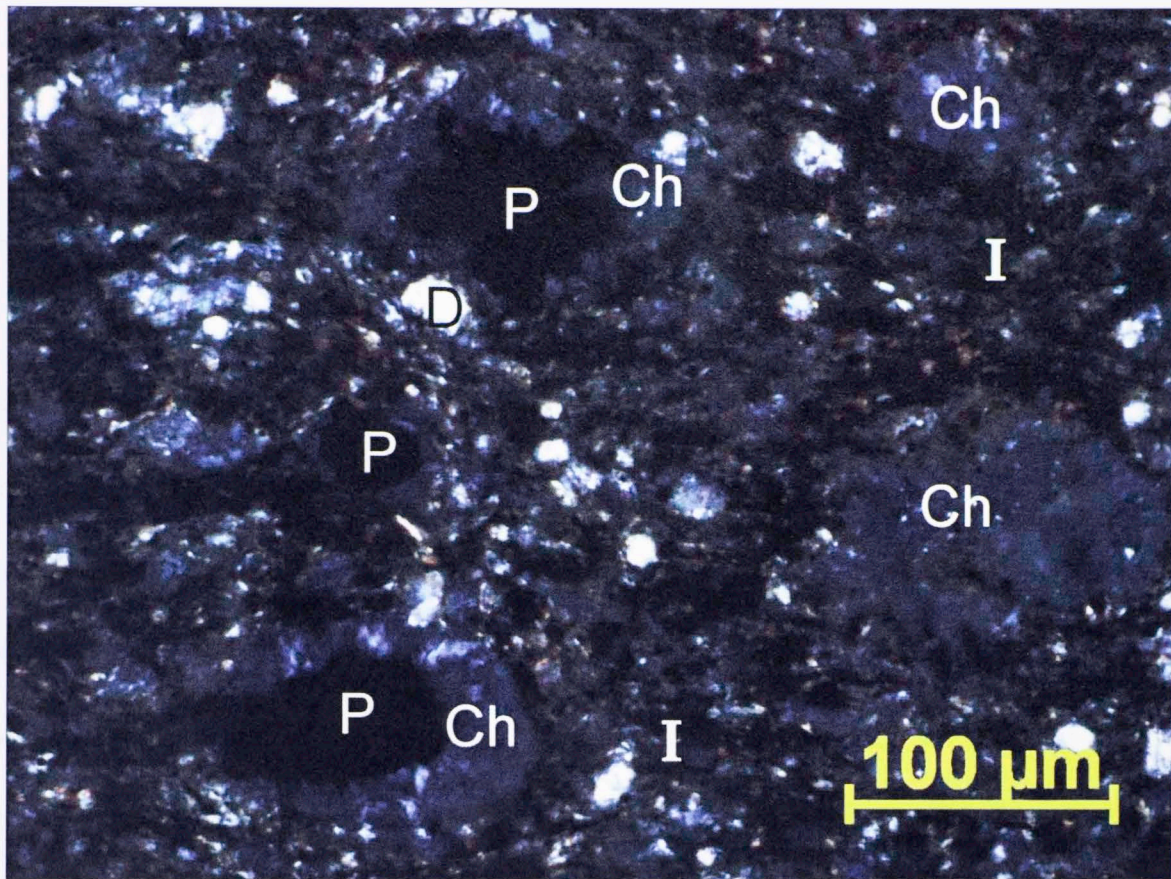


Figure 29. Photomicrograph (XPL) taken from the 135.7 ft petrographic thin section showing a thin layer of chalcedony-rimmed and pyrite-cored Tasmanites algal cysts found in the very top portion of the thin section. Differential compaction of the clay (I) around the cysts is also apparent. I = illite, P = pyrite, Ch = chalcedony, and D = dolomite.

3.1.3 145.3 FT PETROGRAPHIC AND MICROPROBE THIN SECTIONS

The Wyche-1, 145.3 ft petrographic thin section shown in Figure 30 is characterized as a mixed dolomitic-argillaceous, moderately-laminated mudstone with a dark reddish-brown illite-clay matrix and an abundance of dark-brown to opaque organic stringers of unknown origin. The sample is located in the Middle Woodford unit and is approximately 23 feet beneath the Upper-Middle Woodford contact. Sporadic 100 micrometer to 150 micrometer thick, laterally continuous detrital dolomite grain laminations are present throughout the sample. Detrital dolomite rhombs, ranging in diameter from 10 micrometers to 50 micrometers, are disseminated throughout the sample. Less abundant and generally finer-detrital quartz is also present. Mixed dolomite and chert cement is sporadic throughout the matrix, usually having morphologies resembling compressed Tasmanites cysts. Pyrite framboids are also disseminated throughout the sample, ranging in diameter from a few to 100 micrometers. Sub-10 micrometer sized framboids occur frequently throughout the matrix whereas coarser framboids are much less abundant. Fine, blood-red, organic-rich phosphate grains are more prominent in the 145.3 ft interval than the 120.9 ft and 135.7 ft intervals, but are still very minor and sporadic. The occurrence of fine, bright white, detrital apatite grains also increases in this interval. Thin-walled, fully-compacted, light brownish-yellow Tasmanites cysts are present, but minor when compared to the dominant, dark-brown to opaque organic stringers. Zones of increased dark-brown to opaque organic stringers of unknown origin appear throughout the sample. An overall increase in detrital-dolomite grain size occurs from top to bottom in the sample.

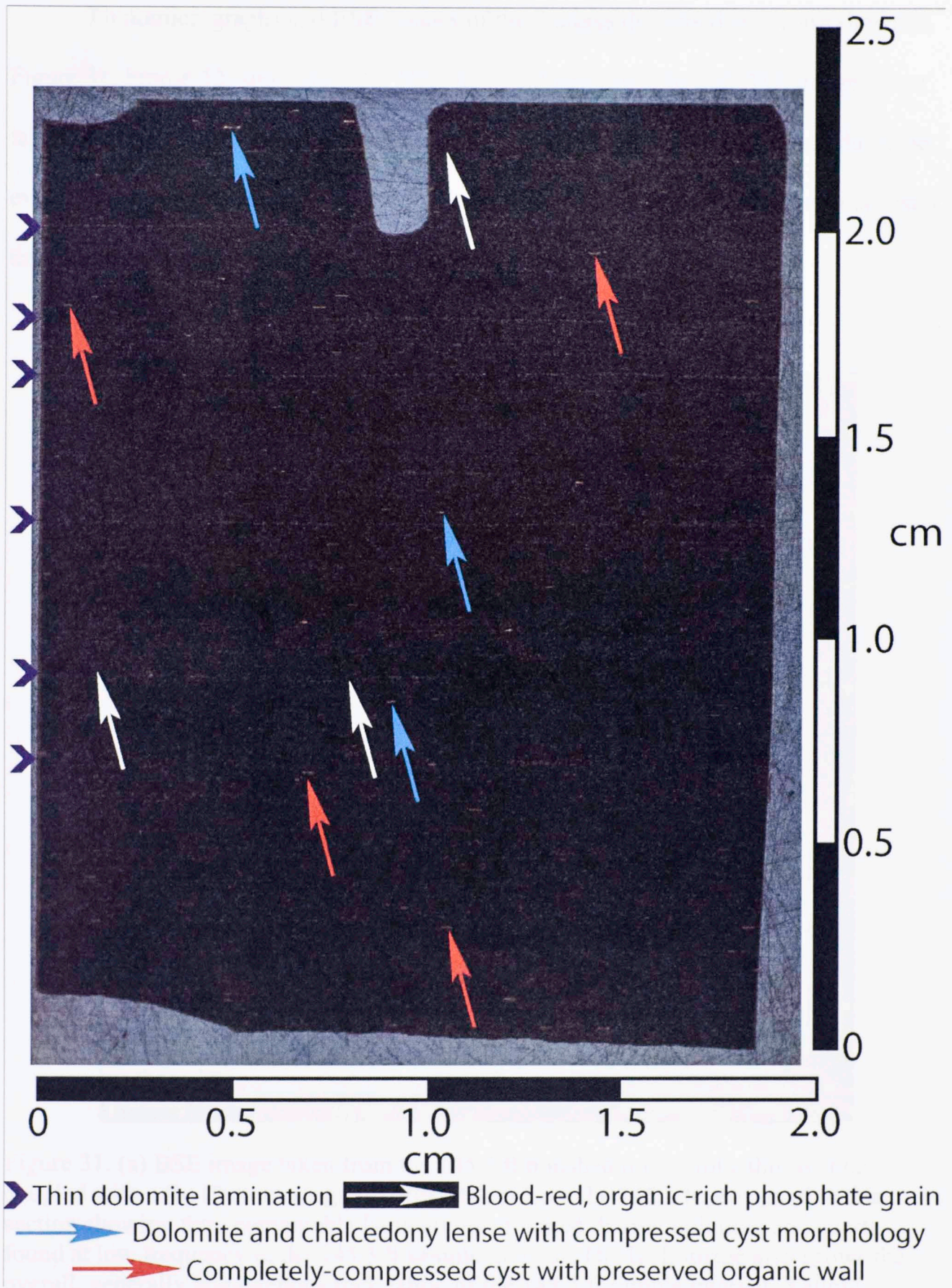


Figure 30. Wyche-1 well, Woodford 145.3 ft petrographic thin section.

Photomicrographs and BSE images of the features described above are shown in Figure 31, Figure 32, and Figure 33. Note that photomicrographs and BSE images were taken from separate thin section samples so when paired, they are not showing the same exact feature(s), but comparable features between the petrographic and microprobe sister thin sections.

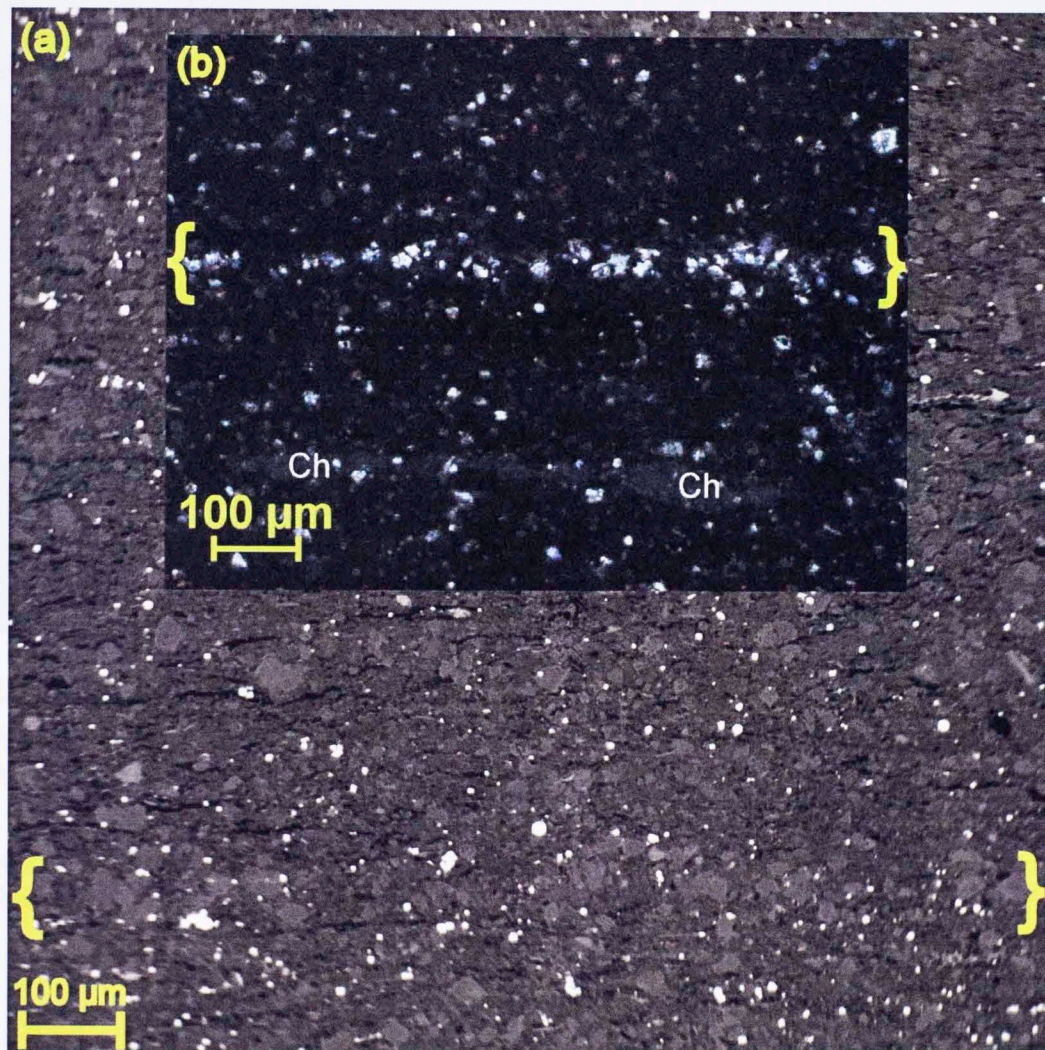


Figure 31. (a) BSE image taken from the 145.3 ft polished microprobe thin section coupled with a (b) Photomicrograph (PPL) taken from the 145.3 ft petrographic thin section showing thin, comparable laminations of mixed detrital dolomite and quartz found at low frequency in the 145.3 ft sample interval. The BSE image also shows the overall, generally homogenous rock fabric of the 145.3 ft sample interval. Yellow brackets bound the mixed detrital dolomite and quartz laminations, Ch = chalcedony.

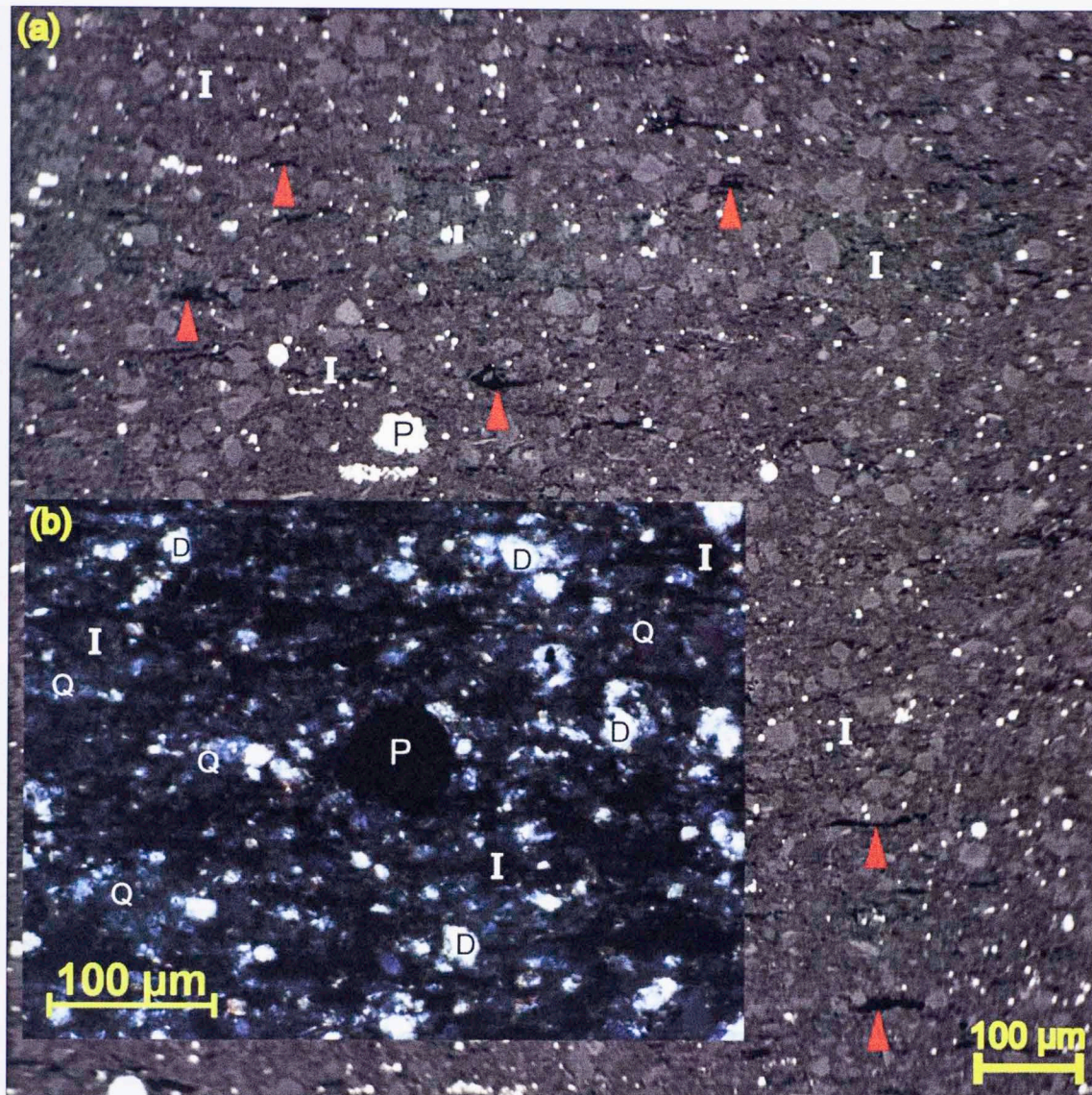


Figure 32. (a) BSE image taken from the 145.3 ft polished microprobe thin section coupled with a (b) Photomicrograph (PPL) taken from the 145.3 ft petrographic thin section showing relatively large pyrite framboids that appear in low frequency throughout the 145.3 ft thin section interval. The BSE image also shows the overall, generally homogenous rock fabric of the 145.3 ft thin section interval. I = illite, P = pyrite, Q = quartz, Ch = chalcedony, D = dolomite, and red arrows exhibit the boundaries of organic stringers.

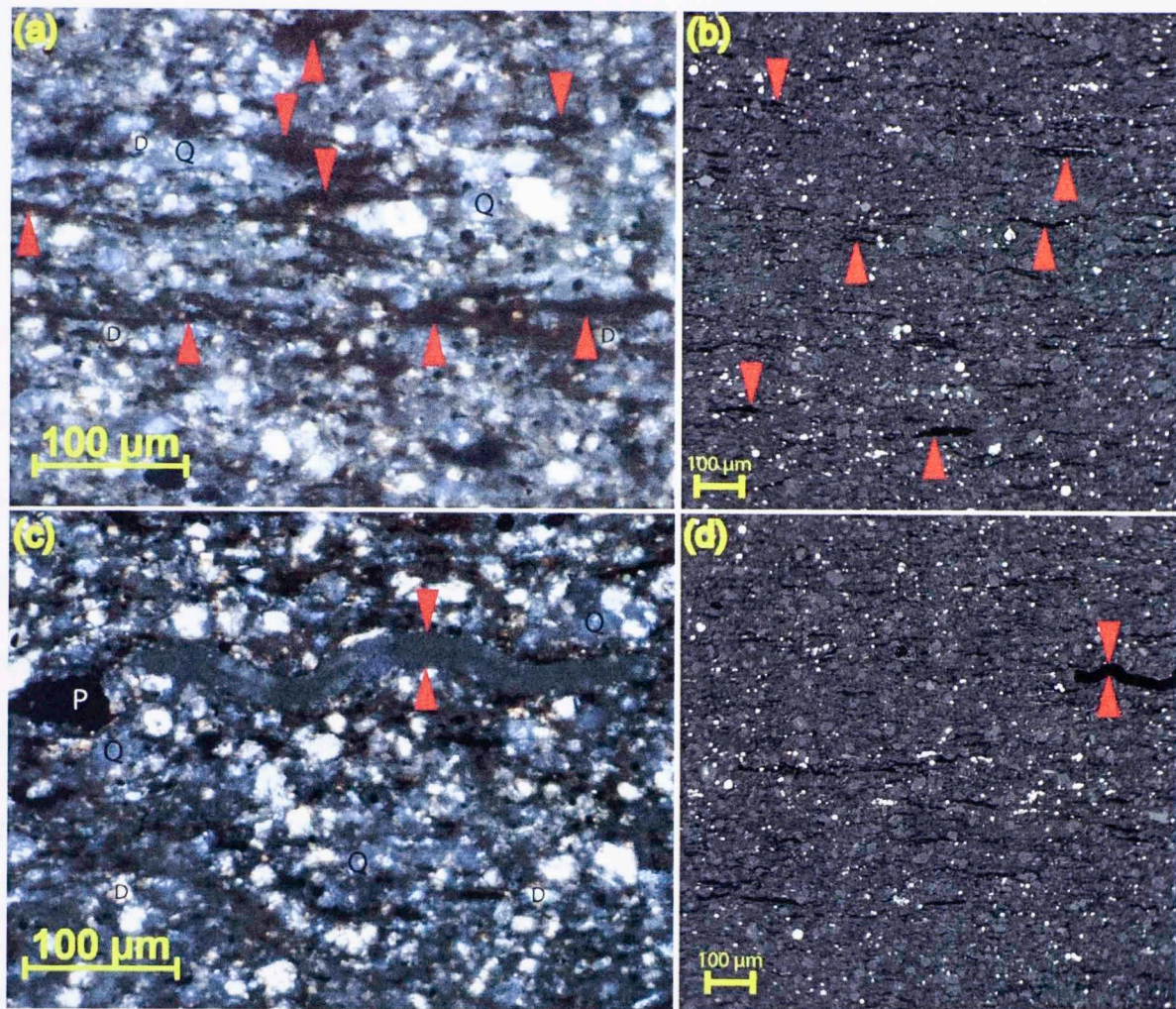


Figure 33. (a) Photomicrograph (PPL) taken from the 145.3 ft petrographic thin section coupled with a (b) BSE image taken from the 145.3 ft polished microprobe thin section showing highly compacted, thin, dark-brown to opaque organic stringers. I = illite, P = pyrite, Q = quartz, D = dolomite, and red arrows exhibit the boundaries of the organic stringers. (c) Another photomicrograph (PPL) of a less frequently observed, fully-compacted Tasmanites cyst coupled with a (d) BSE image showing a comparable fully-compacted cyst as well as several thin organic stringers.

3.2 ENERGY DISPERSIVE X-RAY ANALYSES (EDXA)

The PGT Prism 2000 Energy-Dispersive X-ray Analyzer with a Moxtek polymer entry window affixed to the Cameca SX50 electron probe micro-analyzer was used in conjunction with real-time BSE imaging in order to semi-quantitatively identify mineral phases based on their relative BSE image gray scale for a given sample. Figure 34 through Figure 51 are the results of the spot EDXA performed and show: (1) X-ray energy spectrums labeled with elemental $K\alpha$ and $K\beta$ X-ray peaks, (2) a table showing derived elements and their: (a) X-ray peaks ($K\alpha$, $K\beta$, etc.), (b) X-ray peak intensities, (c) weight percent element, (d) atomic weight percent, (e) oxide formula, (f) weight percent oxide, and (g) cation ratios, as well as (3) a BSE image with a red arrow pointing to the location where the analysis was performed. This mineral phase identification was important in order to identify the principal mineral constituents of a sample as well as to understand the mineral and grain relationships exhibited by the qualitative BSE images.

Mineral phases present in EDXA that are not present in the micro-mineralogy logs are due to: (1) their minor presence in the overall mineralogy of a sample and (2) difficulty in determining how to assign elemental percentages to their mineral formulae (e.g., chlorite, muscovite, kaolinite, plagioclase, K-feldspar). Oil and gas industry service companies such as Schlumberger and Halliburton have developed proprietary, iterative algorithms for mineralogic interpretation of weight percent element data gathered from capture gamma-ray tools such as the ECS (trademark of Schlumberger) and the GEM (trademark of Halliburton) in which the elemental weight percent microprobe data could be subjected to and additional mineral phases derived. However, due to the scope of this study, such advanced equations could not be formulated, but are possible for future work

and data analysis. The minor mineral phases identified by EDXA (e.g., chlorite, muscovite, kaolinite, plagioclase, K-feldspar) are also presented here with major mineral phases (e.g. quartz, dolomite, calcite, pyrite) and organics identified by EDXA to acknowledge their minor occurrence within the samples.

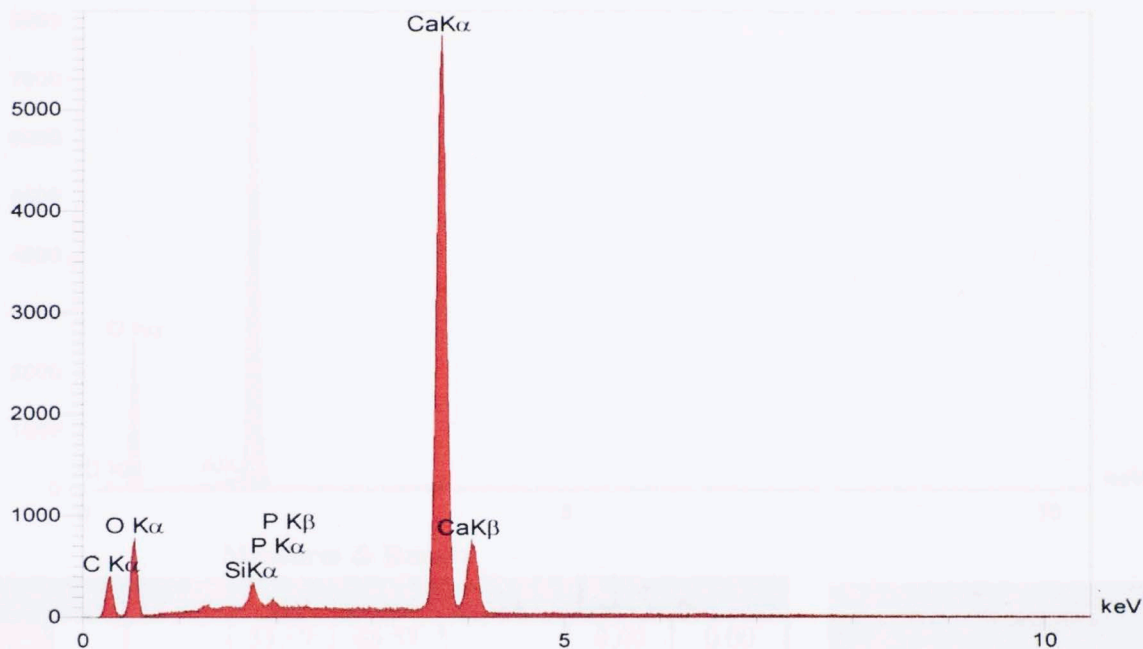


Figure 34. EDXA of the Wyche-1, W-63396 (20.9 Å sample) within a calcite grain located in a calcite host. The red arrow points to a large group of these approximately 10 micrometer in diameter calcite grains that are light-gray in the SEM image. The diffractometer for calcite is CaCO₃.

3.2.1 120.9 FT EDXA of Quartz EDXA

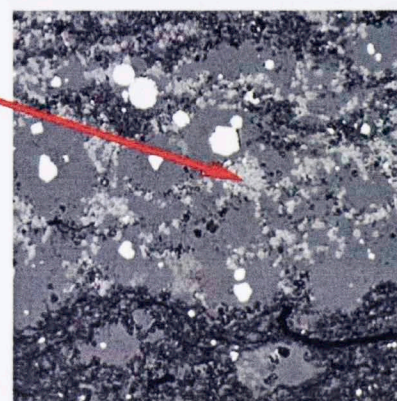
3.2.1.1 120.9 ft Calcite EDXA

Wyche-1 Well Woodford Shale 120.9 ft EDX Analysis (Calcite)



Measures & Results

Element	Line	Int	W%	A%	Formula	Ox%	Cat#
C	Ka	111.9	14.06	22.33	CO2	51.50	1.10
O			51.28	61.17		0.00	0.00
Ca	Ka	2333.2	34.66	16.50	CaO	48.50	0.81
			100.00	100.00		100.00	1.90



527 μm x 527 μm

Figure 34. EDXA of the Wyche-1, Woodford 120.9 ft sample within a calcite grain located in a calcite lamination. The red arrow points to a large group of these approximately 10 micrometer in diameter calcite grains that are light-gray in the BSE image. The mineral formula for calcite is CaCO_3 .

3.2.1.2 120.9 ft Quartz EDXA

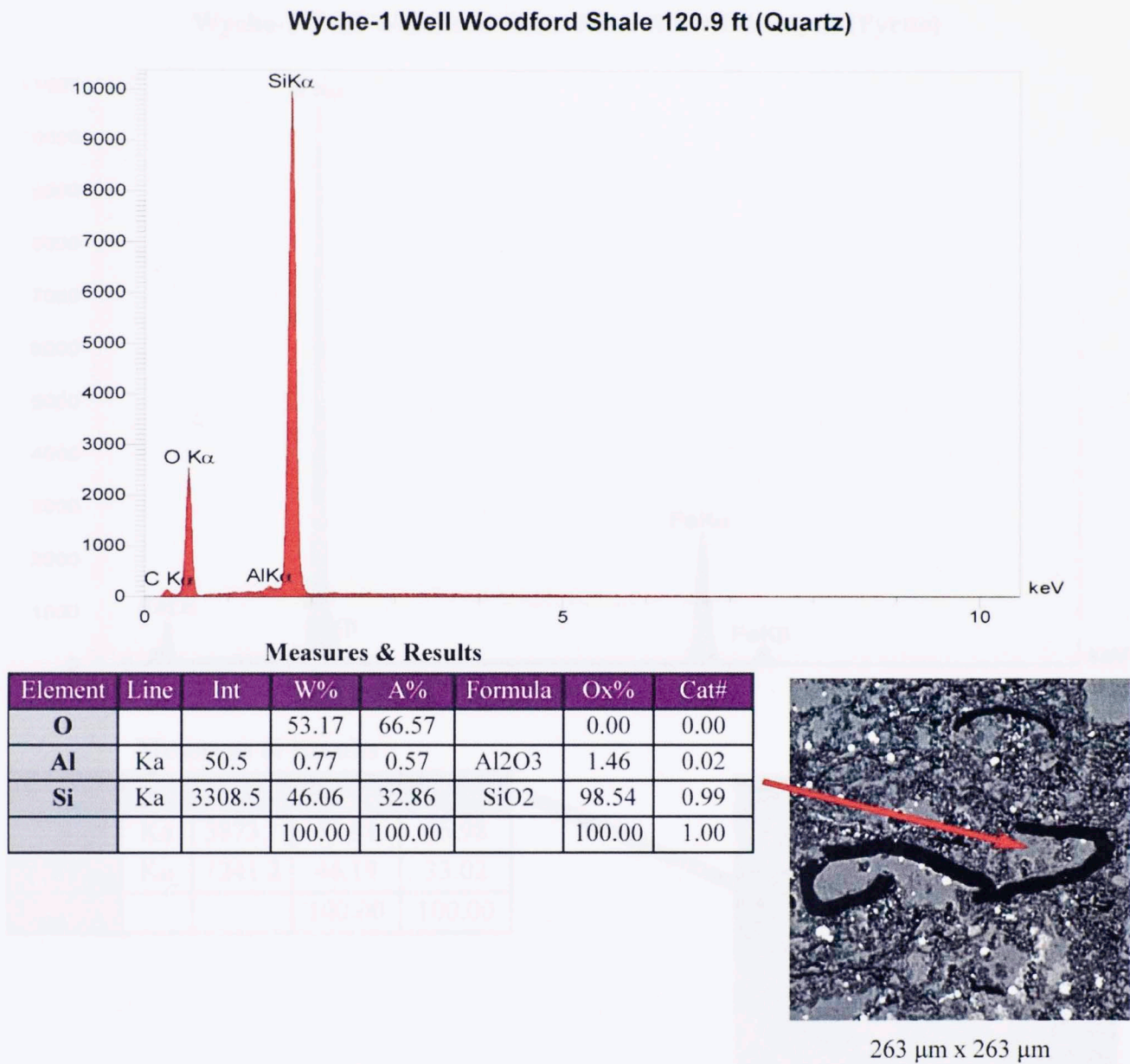
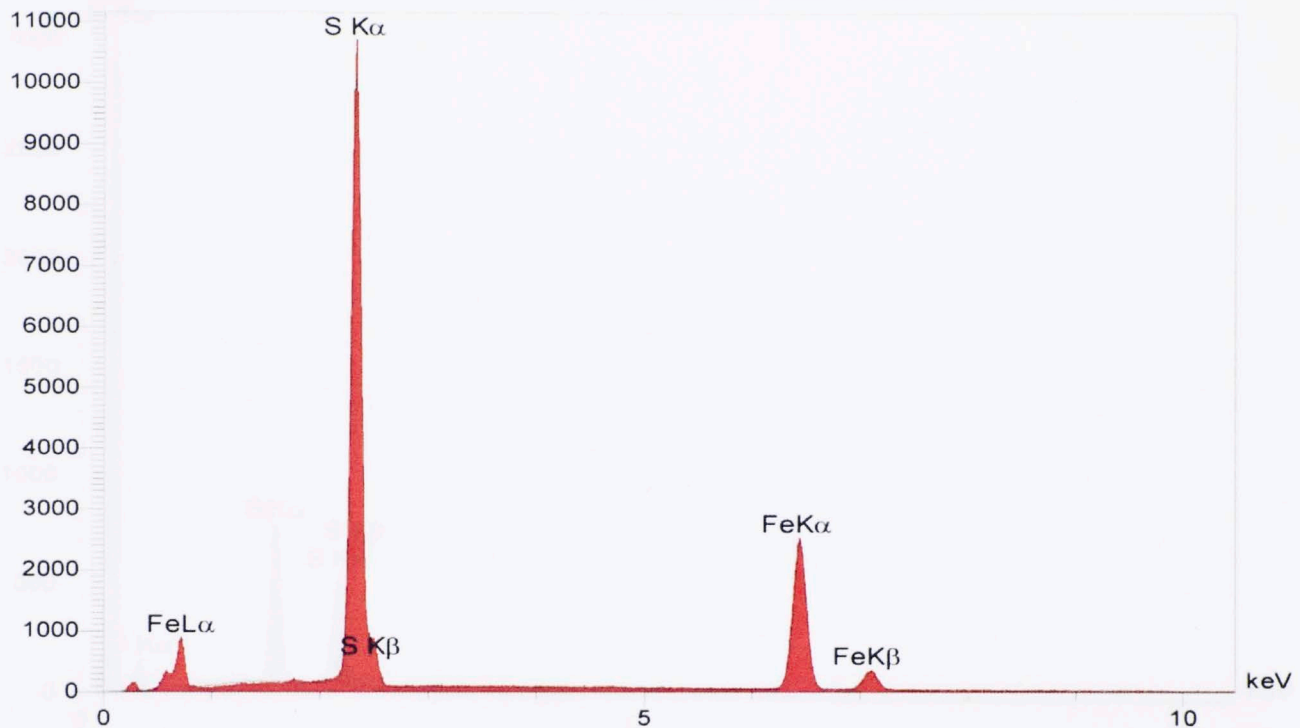


Figure 35. EDXA of the Wyche-1, Woodford 120.9 ft sample within a quartz grain located in a clay lamination. The quartz (mid-gray in BSE image) is wrapped by a ruptured Tasmanites-cyst organic wall that appears black in the BSE image. The mineral formula for quartz is SiO₂.

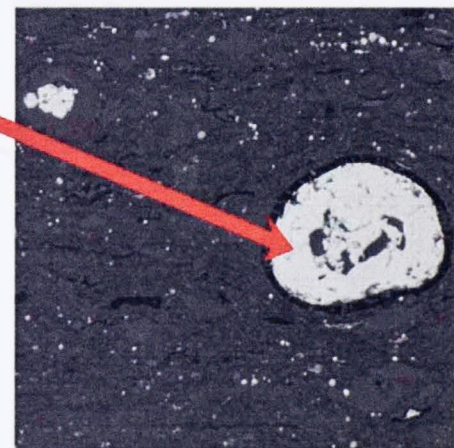
3.2.1.3 120.9 ft Pyrite EDXA

Wyche-1 Well Woodford Shale 120.9 ft EDX Analysis (Pyrite)



Measures & Results

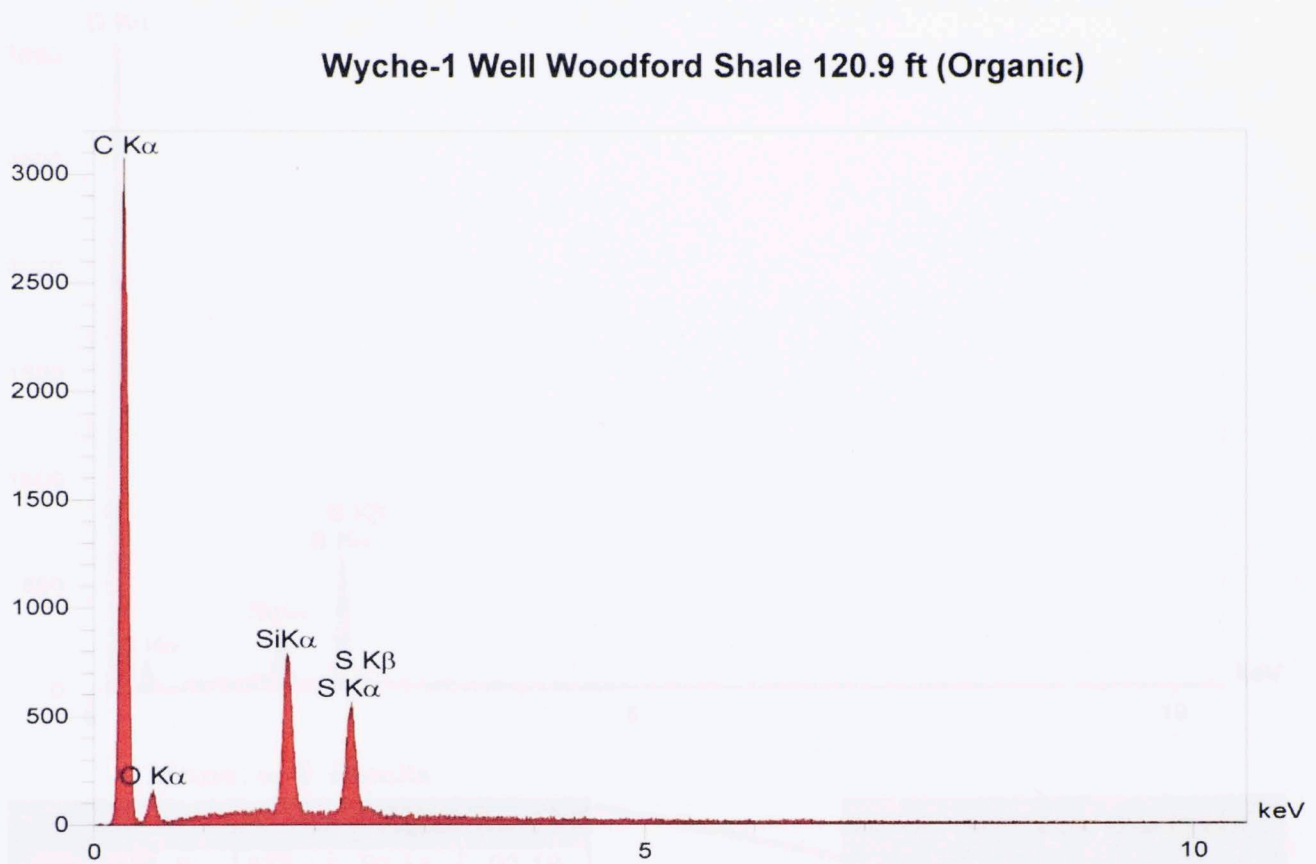
Element	Line	Int	W%	A%
S	Ka	3873.1	53.81	66.98
Fe	Ka	1241.2	46.19	33.02
			100.00	100.00



527 μm x 527 μm

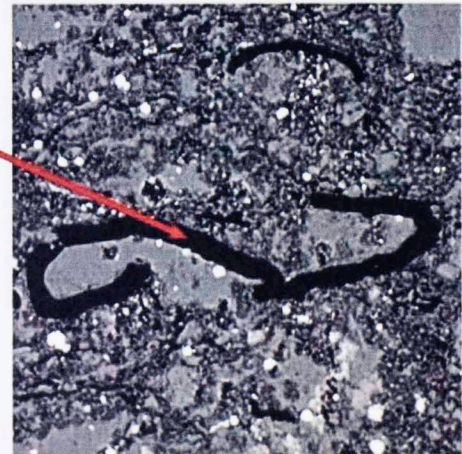
Figure 36. EDXA of the Wyche-1, Woodford 120.9 ft sample within a pyrite grain (bright white in BSE image) located in a clay lamination. The pyrite grain is wrapped by a Tasmanites-cyst organic wall (black in BSE image). The organic wall contains very fine diagenetic-quartz grains (gray in BSE image) that filled the cyst wall pores. Quartz can also be seen in the core of the pyrite located in the cyst. The mineral formula for pyrite is FeS₂.

3.2.1.4 120.9 ft Organic EDXA



Measures & Results

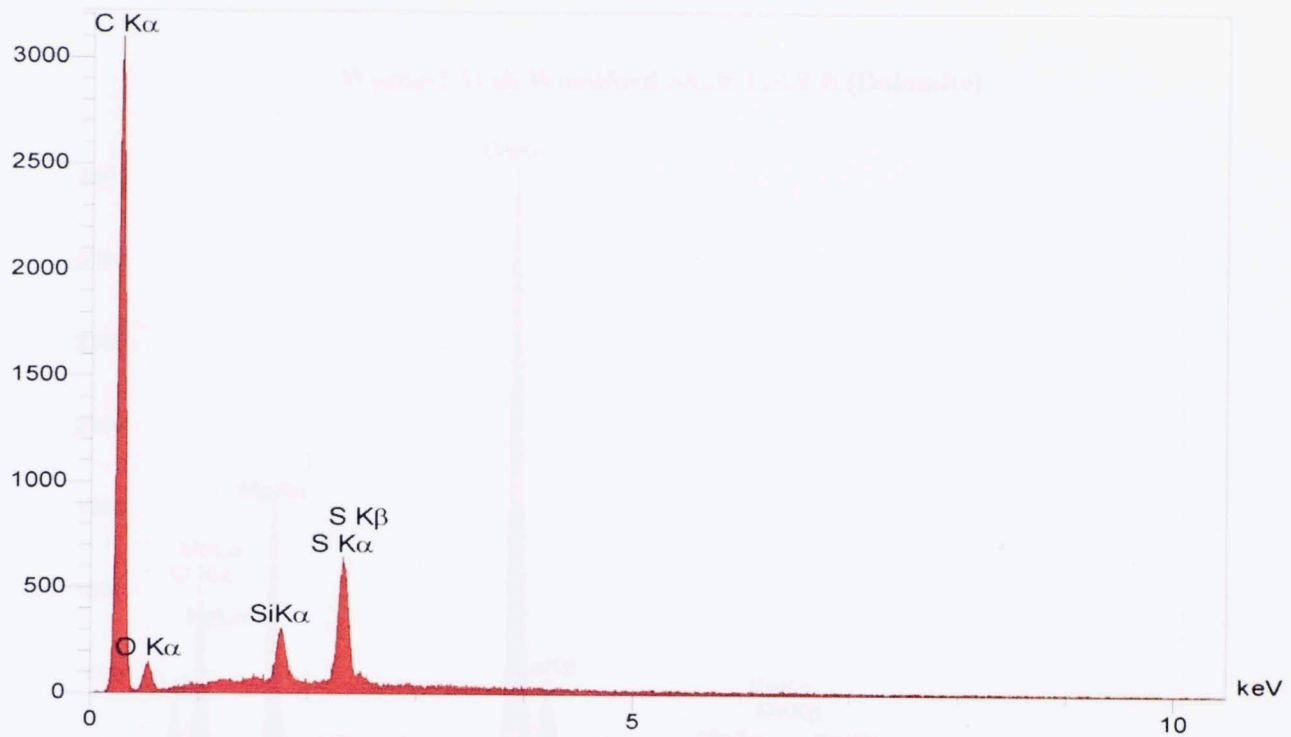
Element	Line	Int	W%	A%
C	Ka	830.6	87.08	91.61
O	Ka	44.2	7.96	6.29
Si	Ka	262.5	2.70	1.21
S	Ka	201.0	2.27	0.89
			100.00	100.00



263 μm x 263 μm

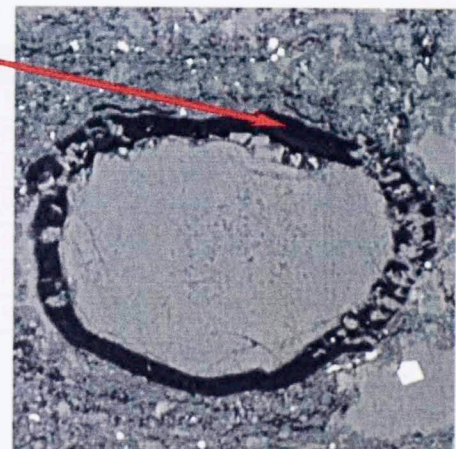
Figure 37. EDXA of the Wyche-1, Woodford 120.9 ft sample within a ruptured and compressed Tasmanites-cyst organic wall (black in BSE image) located in a clay lamination. Quartz grains (gray in BSE image) can be seen between cyst walls in the curls of the S shape.

Wyche-1 Well Woodford 120.9 ft (Organic-clad Quartz)



Measures & Results

Element	Line	Int	W%	A%
C	Ka	833.1	88.14	92.18
O	Ka	40.0	7.92	6.22
Si	Ka	98.5	1.10	0.49
S	Ka	233.6	2.83	1.11
			100.00	100.00

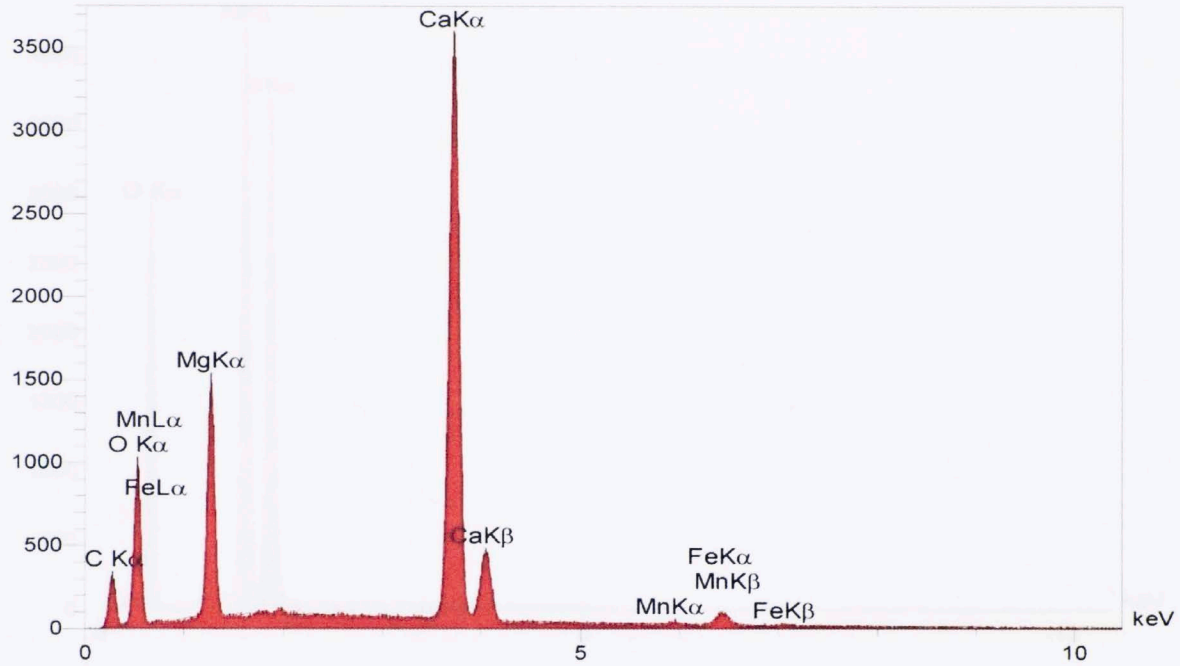


243 μm x 243 μm

Figure 38. EDXA of the Wyche-1, Woodford 120.9 ft sample within a Tasmanites-cyst organic wall (black in BSE image) located in a clay lamination. Note that in the image, some of the organic wall is being replaced by quartz (gray in BSE image) and that the entire interior of the cyst has been filled by quartz. The diagenetic quartz inside the cyst wall filled the pores of the cyst wall.

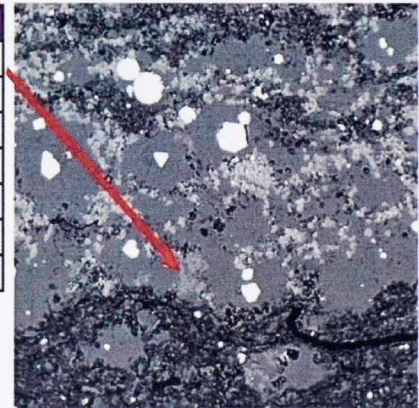
3.2.1.5 120.9 ft Dolomite EDXA

Wyche-1 Well Woodford Shale 120.9 ft (Dolomite)



Measures & Results

Element	Line	Int	W%	A%	Formula	Ox%	Cat#
C	Ka	89.0	14.79	22.35	CO2	54.18	2.19
O			53.91	61.18		0.00	0.00
Mg	Ka	455.5	8.38	6.26	MgO	13.90	0.61
Ca	Ka	1449.6	21.55	9.76	CaO	30.16	0.96
Mn	Ka	4.5	0.14	0.04	MnO	0.17	0.00
Fe	Ka	36.3	1.23	0.40	FeO	1.58	0.04
			100.00	100.00		100.00	3.81

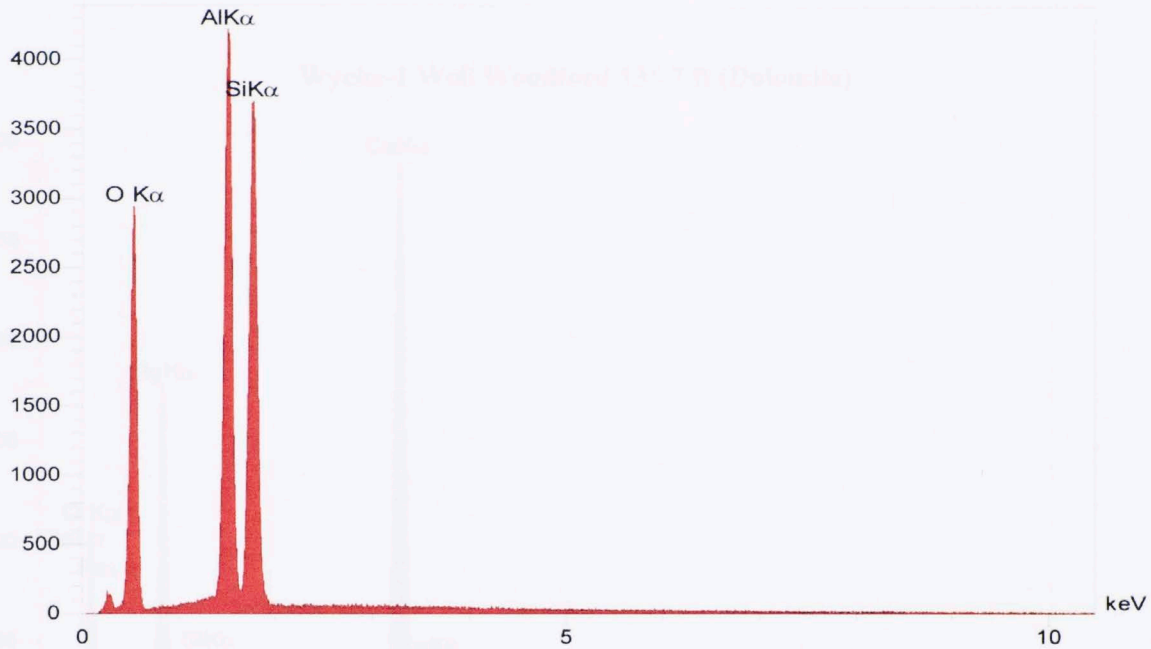


527 μm x 527 μm

Figure 39. EDXA of the Wyche-1, Woodford 120.9 ft sample within a dolomite grain located in a calcite lamination. The dolomite grain has replaced calcite through diagenetic alteration. Calcite appears as light gray and quartz appears as dark gray in the BSE image. Dolomite appears as a mid-level gray between that of the quartz and calcite in the BSE image. The chemical formula for dolomite is $(Ca,Mg)(CO_3)_2$.

3.2.1.6 120.9 ft Kaolinite EDXA

Wyche-1 Well Woodford 120.9 ft (Kaolinite)



Measures & Results

Element	Line	Int	W%	A%	Formula	Ox%	Cat#
O			50.46	63.68		0.00	0.00
Al	Ka	1440.0	23.97	17.94	Al ₂ O ₃	45.29	1.97
Si	Ka	1265.3	25.57	18.39	SiO ₂	54.71	2.02
			100.00	100.00		100.00	3.99



100 μm x 100 μm

Figure 40. EDXA of the Wyche-1, Woodford 120.9 ft sample within an authigenic kaolinite clay (dark gray in BSE image) located inside a Tasmanites algal cyst filled rim. The rim of the cyst fill is quartz (light gray in BSE image). The mineral formula for kaolinite is Al₄[Si₄O₁₀](OH)₈.

3.2.2 135.7 FT EDXA

3.2.2.1 135.7 ft Dolomite EDXA

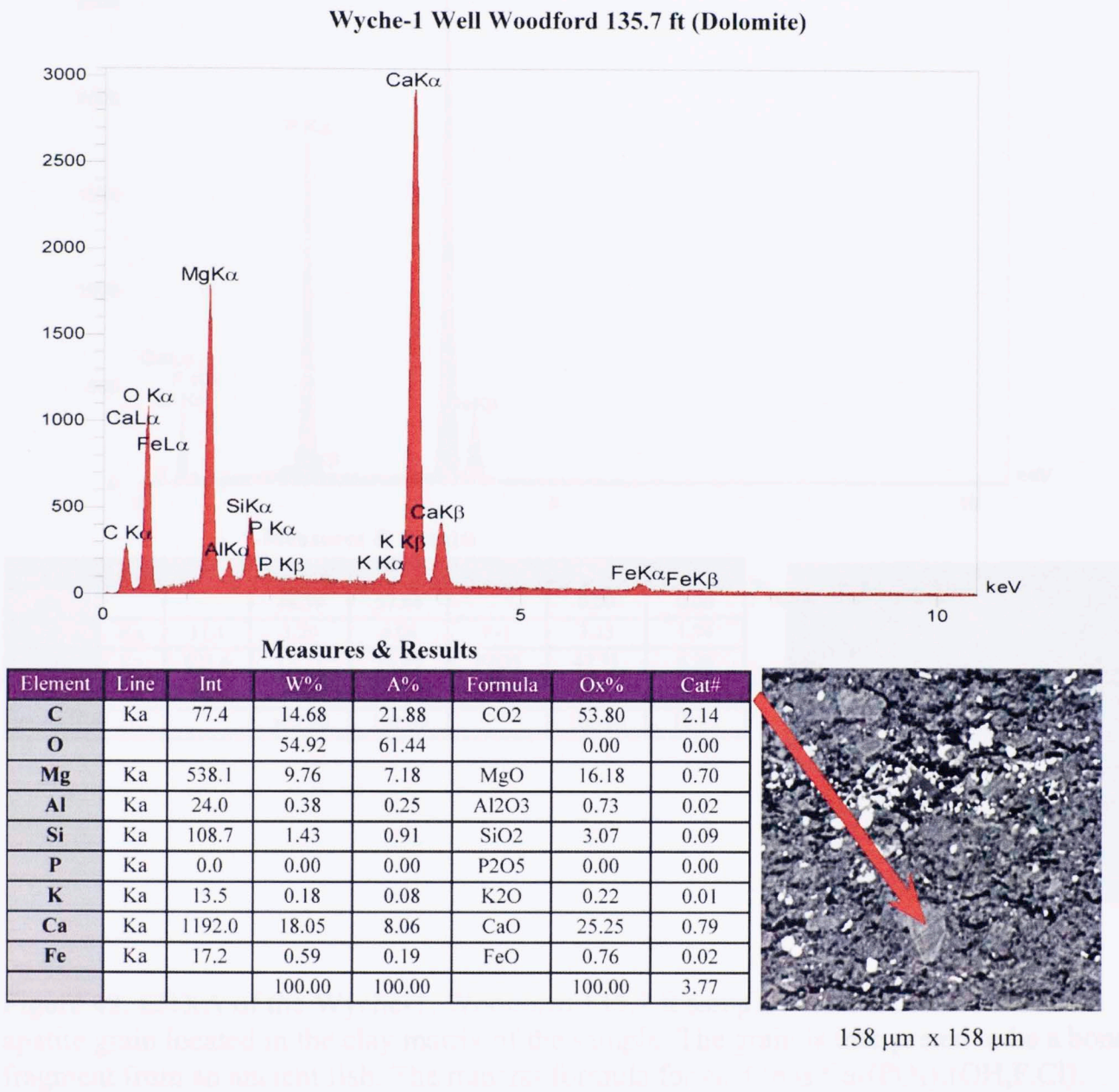
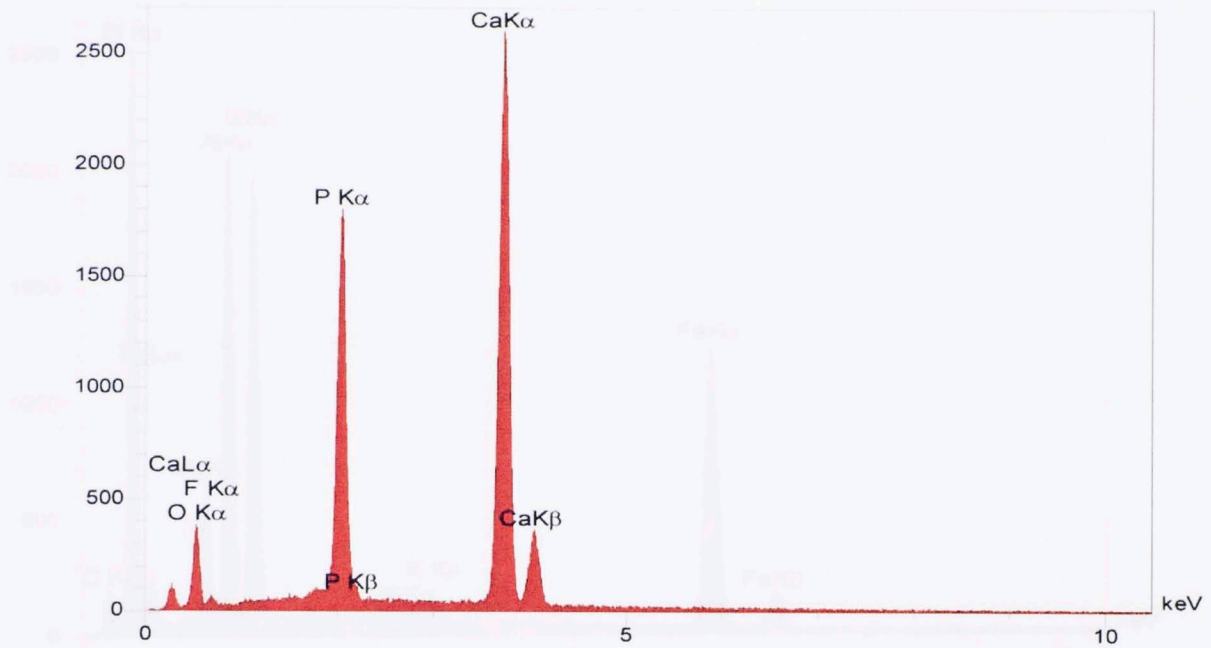


Figure 41. EDXA of the Wyche-1, Woodford 135.7 ft sample within a dolomite grain located in the clay matrix of the sample. The mineral formula for dolomite is $\text{CaMg}(\text{CO}_3)_2$.

3.2.2.2 135.7 ft Apatite EDXA

Wyche-1 Well Woodord 135.7 ft (Apatite, possible bone fragment)



Measures & Results

Element	Line	Int	W%	A%	Formula	Ox%	Cat#
O			38.59	57.84		0.00	0.00
F	Ka	11.1	3.20	4.04	F-1	3.15	1.74
P	Ka	621.6	18.71	14.49	P2O5	42.31	6.26
Ca	Ka	1041.7	39.50	23.64	CaO	54.54	10.22
			100.00	100.00		100.00	18.22

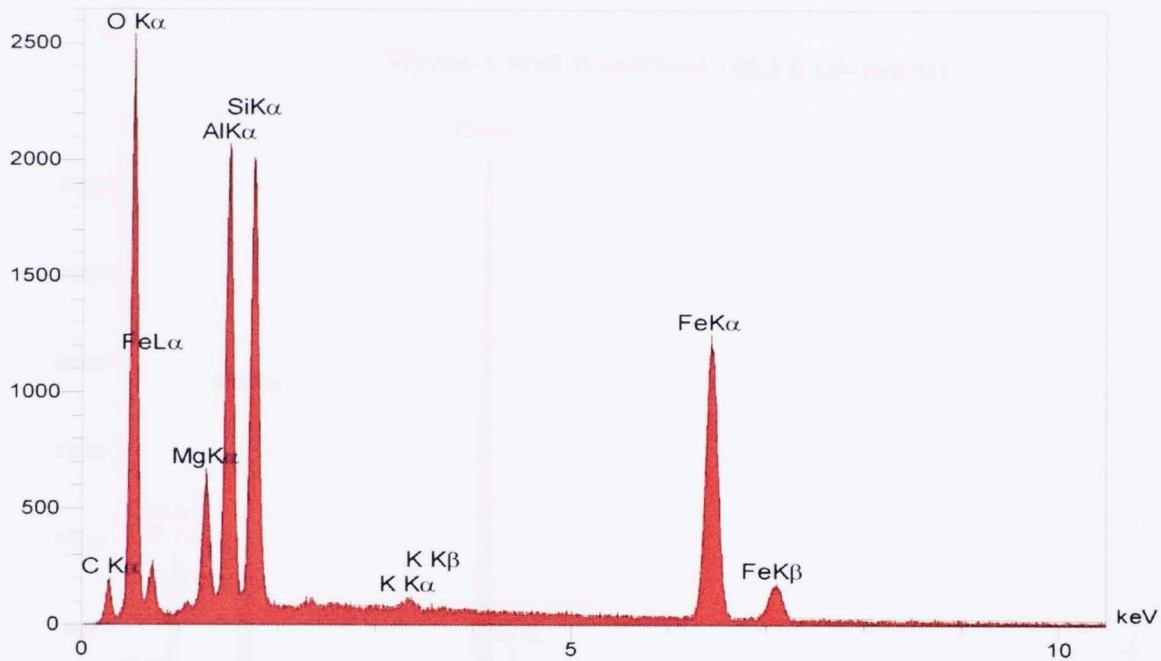


1580 μm x 1580 μm

Figure 42. EDXA of the Wyche-1, Woodford 135.7 ft sample within a coarse, detrital apatite grain located in the clay matrix of the sample. The grain is interpreted to be a bone fragment from an ancient fish. The mineral formula for apatite is $Ca_5(PO_4)_3(OH,F,Cl)$.

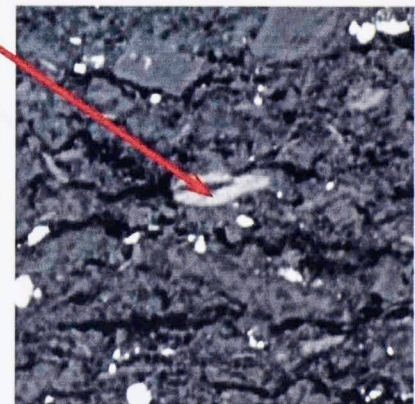
3.2.2.3 135.7 ft Chlorite EDXA

Wyche-1 Well Woodford 135.7 ft (Chlorite)



Measures & Results

Element	Line	Int	W%	A%	Formula	Ox%	Cat#
O			39.79	59.04		0.00	0.00
Mg	Ka	187.8	5.15	5.03	MgO	8.54	1.19
Al	Ka	662.9	14.56	12.81	Al ₂ O ₃	27.52	3.04
Si	Ka	657.3	13.91	11.76	SiO ₂	29.77	2.79
K	Ka	15.5	0.31	0.19	K ₂ O	0.38	0.05
Fe	Ka	596.8	26.27	11.17	FeO	33.80	2.65
			100.00	100.00		100.00	9.71



100 μm x 100 μm

Figure 43. EDXA of the Wyche-1, Woodford 135.7 ft sample within a chlorite grain (light gray in BSE image) located in the clay matrix of the sample. The mineral formula for chlorite is $(Mg,Al,Fe)_{12}[(Si,Al)_8O_{20}](OH)_{16}$.

3.2.3 145.3 FT EDXA

3.2.3.1 145.3 ft Dolomite EDXA

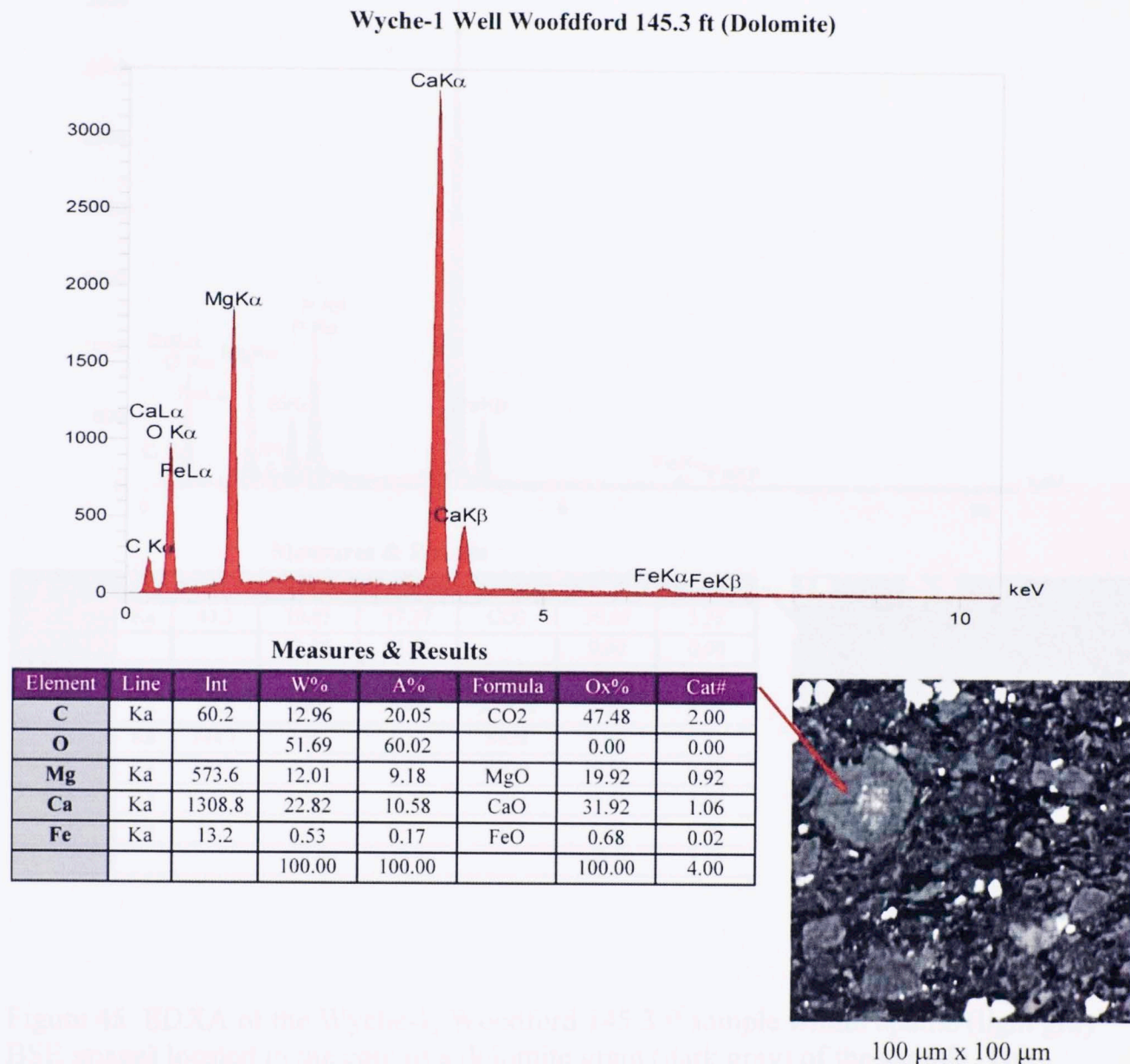


Figure 44. EDXA of the Wyche-1, Woodford 145.3 ft sample within a dolomite grain (dark gray in BSE image) located in the clay matrix of the sample. Note the apatite (light gray in BSE image) at the core of the dolomite grain. The mineral formula for dolomite is $\text{CaMg}(\text{CO}_3)_2$.

3.2.3.2 145.3 ft Apatite EDXA

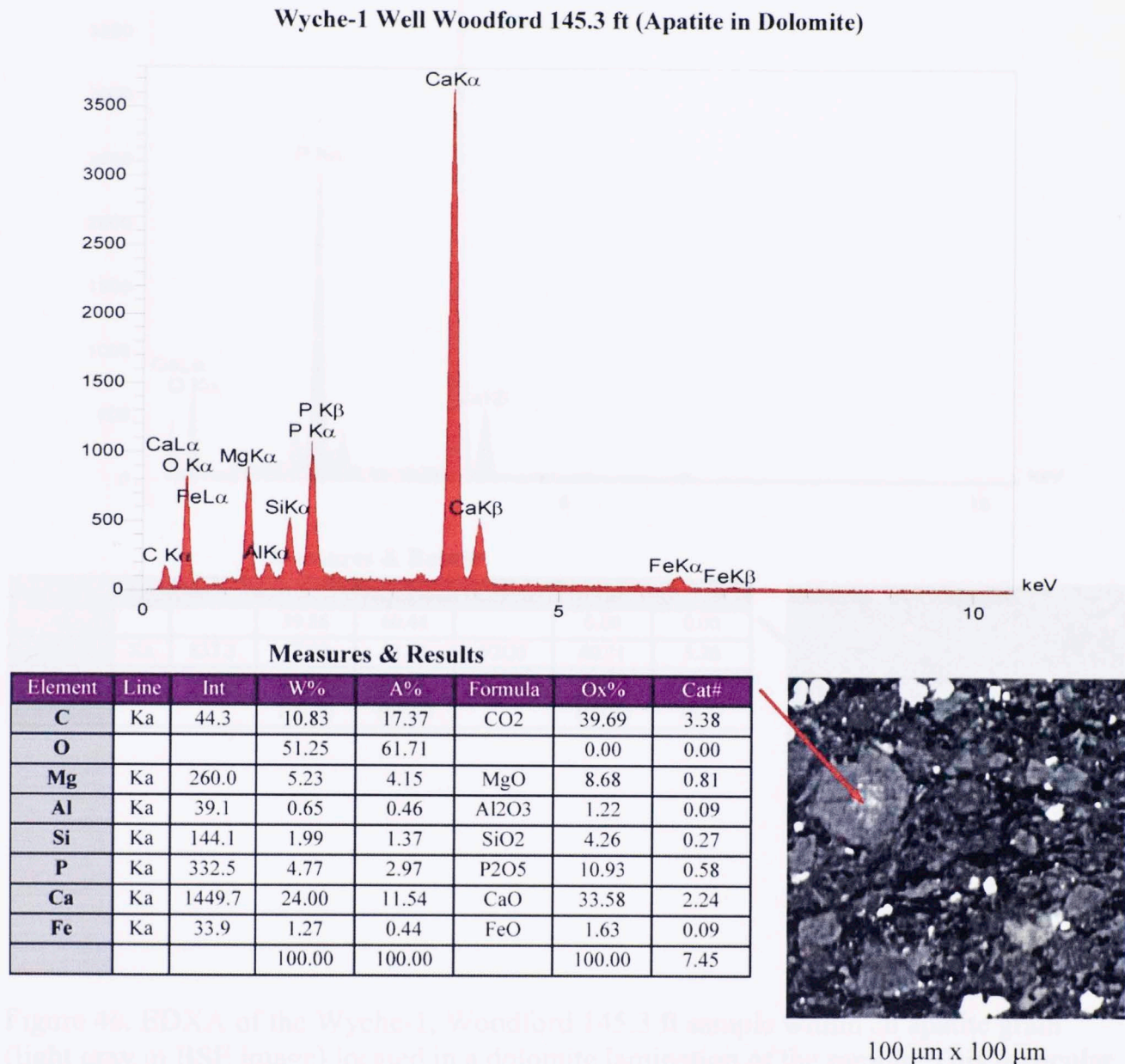
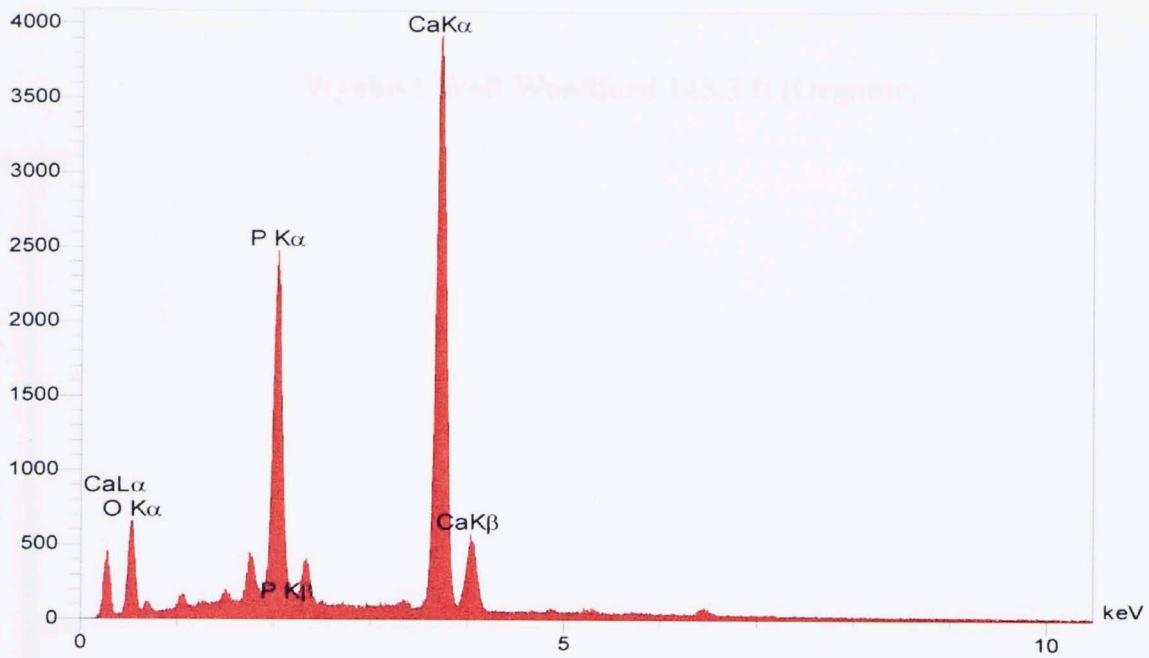


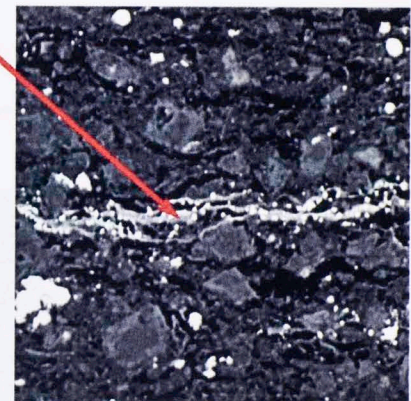
Figure 45. EDXA of the Wyche-1, Woodford 145.3 ft sample within apatite (light gray BSE image) located in the core of a dolomite grain (dark gray) of the sample. The mineral formula for apatite is $Ca_5(PO_4)_3(OH,F,Cl)$.

Wyche-1 Well Woodford 145.3 ft (Apatite)



Measures & Results

Element	Line	Int	W%	A%	Formula	Ox%	Cat#
O			39.86	60.44		0.00	0.00
P	Ka	837.3	17.77	13.91	P2O5	40.71	5.76
Ca	Ka	1587.0	42.38	25.65	CaO	59.29	10.61
			100.00	100.00		100.00	16.37

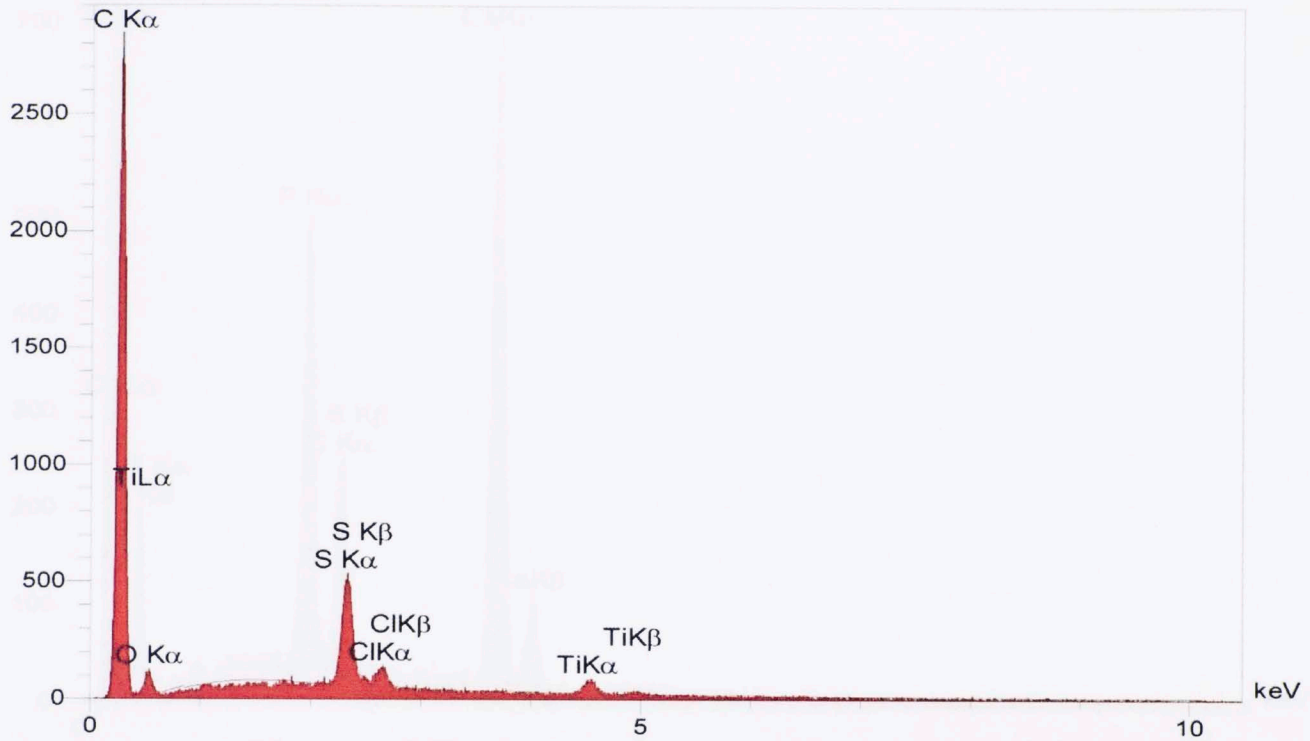


158 μm x 158 μm

Figure 46. EDXA of the Wyche-1, Woodford 145.3 ft sample within an apatite grain (light gray in BSE image) located in a dolomite lamination of the sample. This particular sub-lamina exhibits a concentration of fine-apatite grains and several fine-pyrite frambooids seen at the center of the BSE image. The mineral formula for apatite is $Ca_5(PO_4)_3(OH,F,Cl)$.

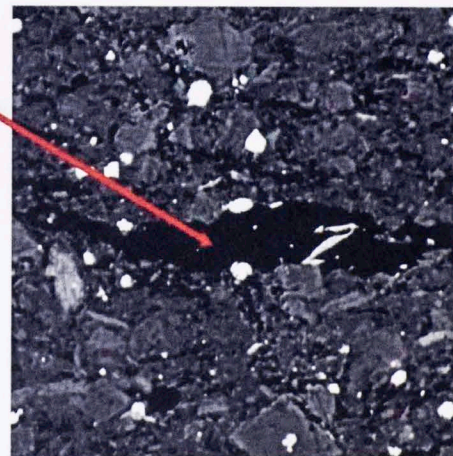
3.2.3.3 145.3 ft Organic EDXA

Wyche-1 Well Woodford 145.3 ft (Organic)



Measures & Results

Element	Line	Int	W%	A%
C	Ka	780.9	89.99	93.75
O	Ka	26.1	6.26	4.90
S	Ka	177.7	2.51	0.98
Cl	Ka	36.0	0.57	0.20
Ti	Ka	25.9	0.67	0.18
			100.00	100.00

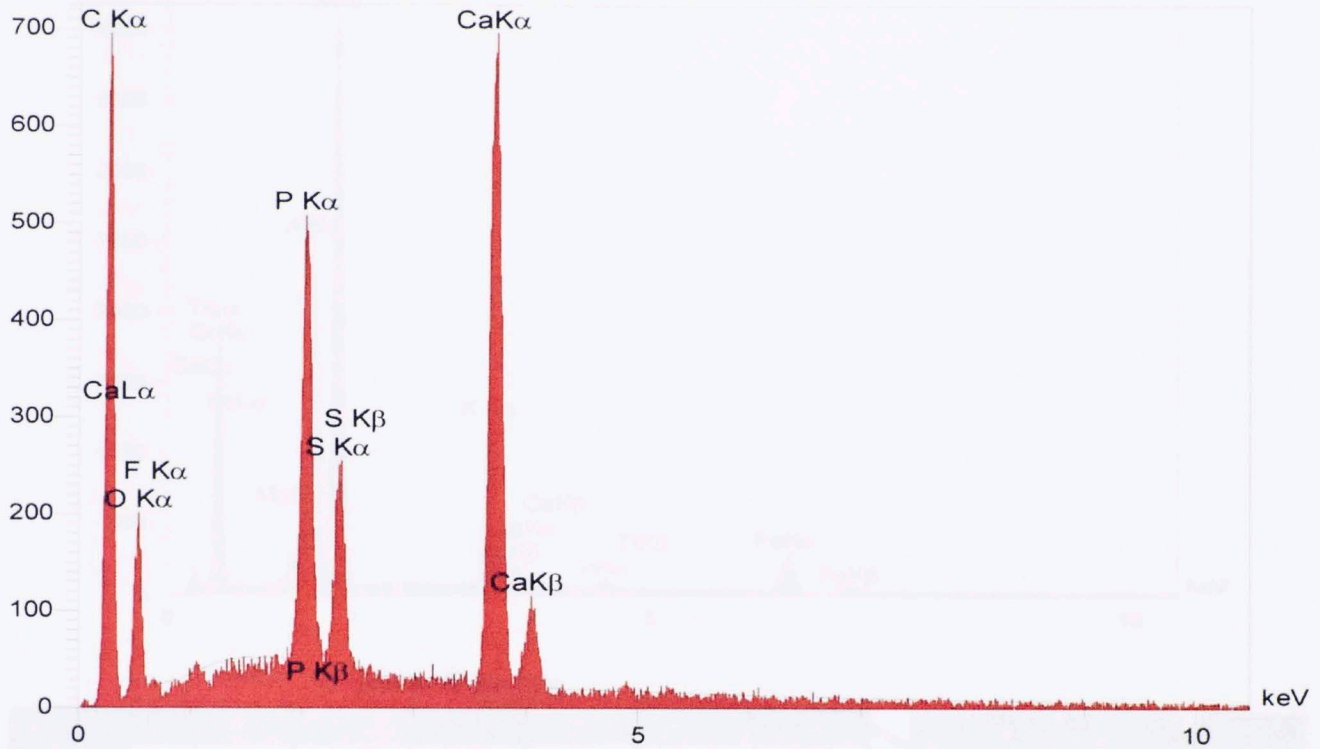


158 μm x 158 μm

Figure 47. EDXA of the Wyche-1, Woodford 145.3 ft sample within an organic stringer (black in BSE image) located in the clay matrix of the sample.

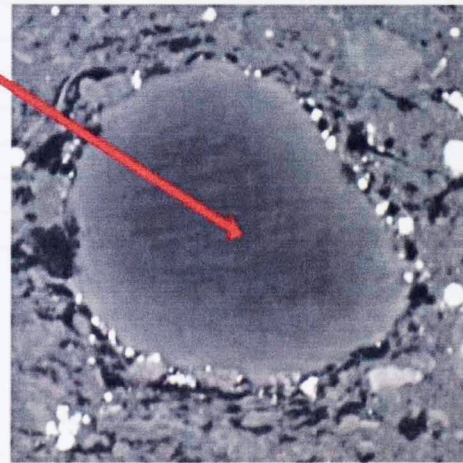
3.2.3.4 145.3 ft Blood-Red Organic Phosphate EDXA

Wyche-1 Well Woodford 145.3 ft (Organic-rich phosphate)



Measures & Results

Element	Line	Int	W%	A%
C	Ka	176.0	62.66	74.88
O	Ka	50.3	20.14	18.07
F	Ka	2.5	0.58	0.44
P	Ka	160.3	4.49	2.08
S	Ka	74.0	2.09	0.94
Ca	Ka	272.4	10.04	3.59
			100.00	100.00

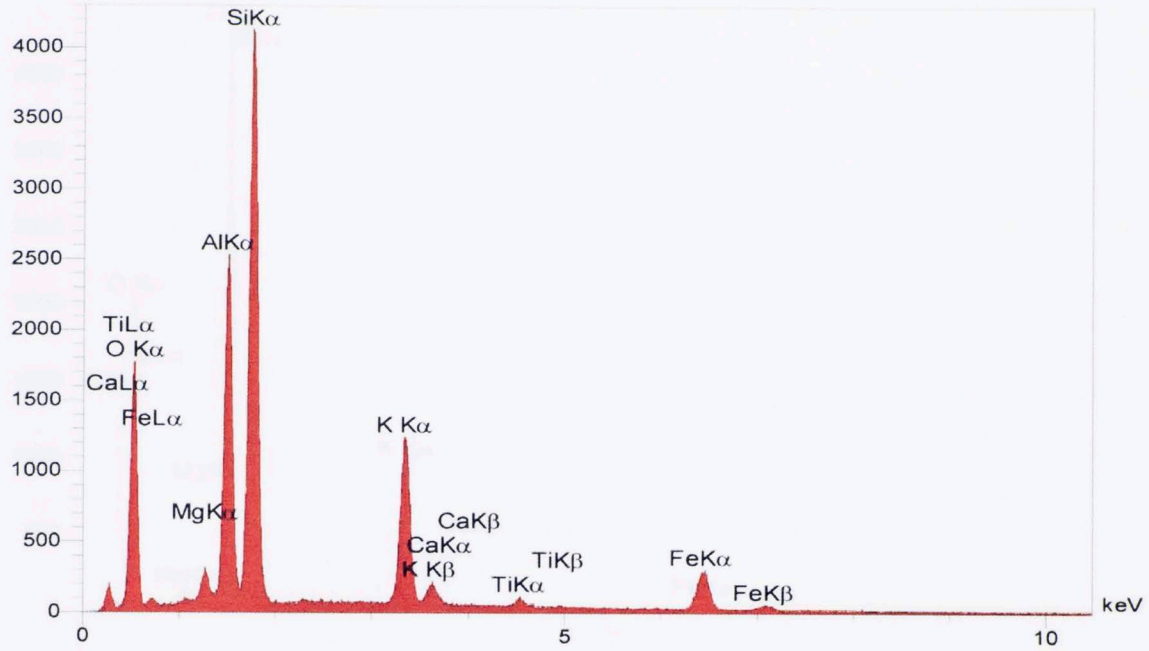


100 μ m x 100 μ m

Figure 48. EDXA of the Wyche-1, Woodford 145.3 ft sample within a blood-red (under the petrographic microscope) organic-rich phosphate. The core of the grain exhibits a more organic EDXA spectrum whereas the rim of the grain exhibits a more phosphatic EDXA spectrum.

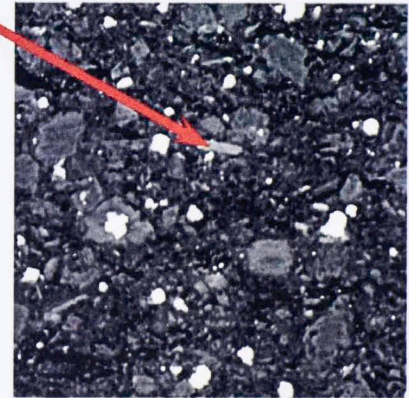
3.2.3.5 145.3 ft Mica EDXA

Wyche-1 Well Woodford 145.3 ft (Mica)



Measures & Results

Element	Line	Int	W%	A%	Formula	Ox%	Cat#
O			44.81	61.01		0.00	0.00
Mg	Ka	71.5	1.52	1.36	MgO	2.52	0.25
Al	Ka	815.3	13.85	11.18	Al ₂ O ₃	26.17	2.02
Si	Ka	1383.6	24.22	18.78	SiO ₂	51.81	3.39
K	Ka	468.8	9.24	5.15	K ₂ O	11.13	0.93
Ca	Ka	4.8	0.10	0.06	CaO	0.14	0.01
Ti	Ka	17.5	0.47	0.21	TiO ₂	0.78	0.04
Fe	Ka	134.1	5.80	2.26	FeO	7.46	0.41
			100.00	100.00		100.00	7.03

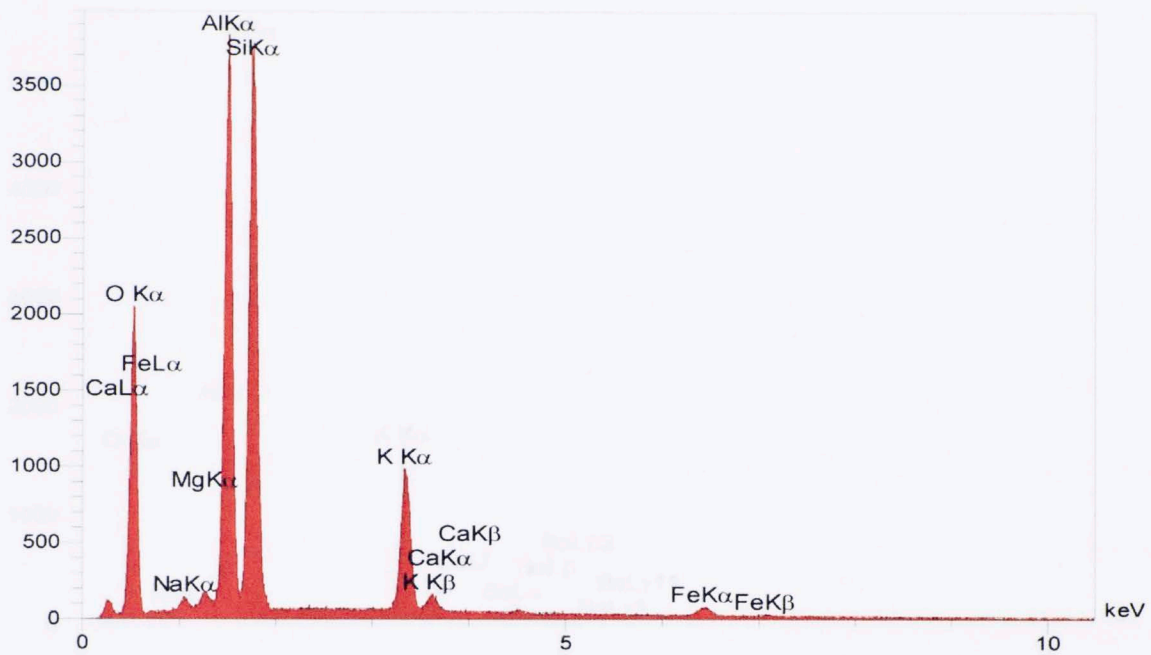


158 μ m x 158 μ m

Figure 49. EDXA of the Wyche-1, Woodford 145.3 ft sample within a mica grain (light gray in BSE image) located in the clay matrix of the sample.

3.2.3.6 145.3 ft Muscovite EDXA

Wyche-1 Well Woodford 145.3 ft (Muscovite)



Measures & Results

Element	Line	Int	W%	A%	Formula	Ox%	Cat#
O			46.75	61.35		0.00	0.00
Na	Ka	29.2	0.91	0.83	Na2O	1.23	0.15
Mg	Ka	34.7	0.70	0.61	MgO	1.17	0.11
Al	Ka	1225.9	19.96	15.53	Al2O3	37.72	2.79
Si	Ka	1251.2	23.09	17.26	SiO2	49.40	3.10
K	Ka	361.6	7.30	3.92	K2O	8.79	0.70
Ca	Ka	0.0	0.00	0.00	CaO	0.00	0.00
Ti	Ka	4.3	0.12	0.05	TiO2	0.19	0.01
Fe	Ka	26.5	1.17	0.44	FeO	1.50	0.08
			100.00	100.00		100.00	6.93

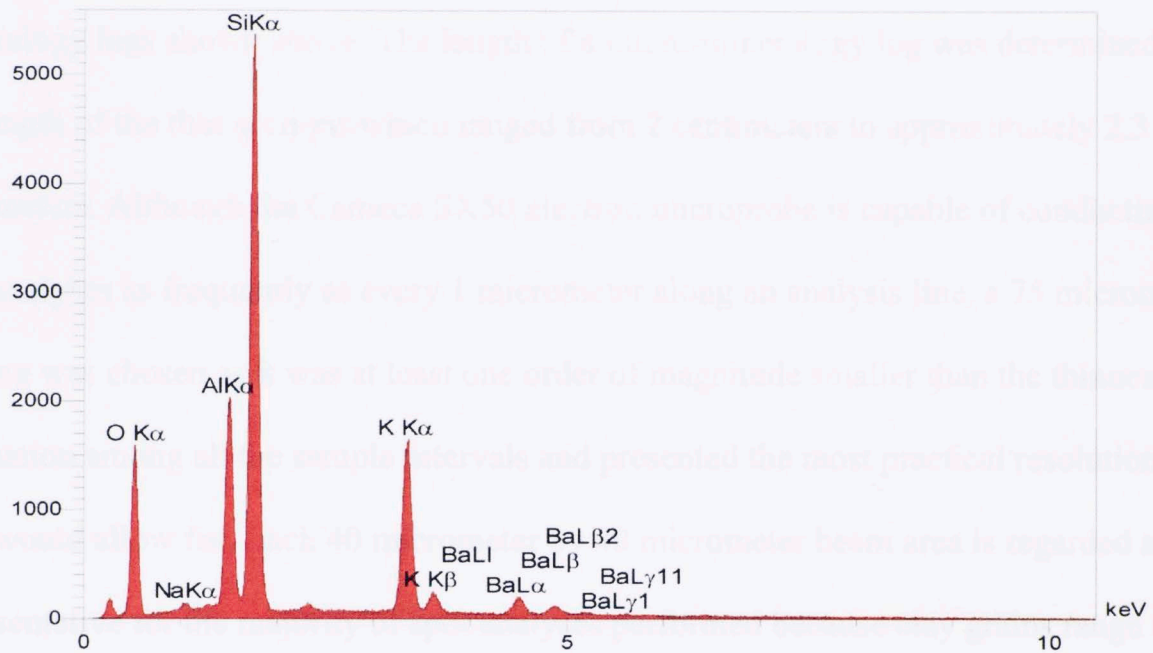


100 μ m x 100 μ m

Figure 50. EDXA of the Wyche-1, Woodford 145.3 ft sample within a muscovite grain (light gray in BSE image) located in the clay matrix of the sample. The mineral formula for muscovite is $K_2Al_4[Si_6Al_2O_{20}](OH,F)_4$.

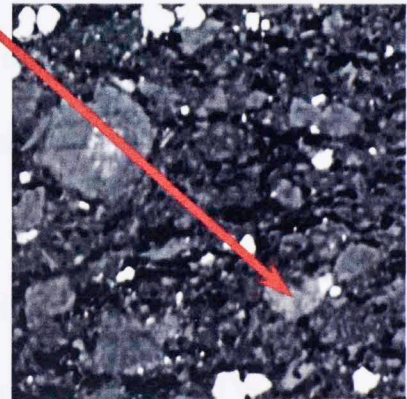
3.2.3.7 145.3 ft K-Feldspar EDXA

Wyche-1 Well Woodford 145.3 ft (K-Feldspar)



Measures & Results

Element	Line	Int	W%	A%	Formula	Ox%	Cat#
O			43.95	61.18		0.00	0.00
Na	Ka	35.3	1.04	1.00	Na2O	1.40	0.13
Al	Ka	684.4	10.47	8.64	Al2O3	19.78	1.13
Si	Ka	1813.3	27.47	21.78	SiO2	58.76	2.85
K	Ka	640.9	11.35	6.46	K2O	13.67	0.84
Ba	La	81.9	5.73	0.93	BaO	6.39	0.12
			100.00	100.00		100.00	5.08



100 μm x 100 μm

Figure 51. EDXA of the Wyche-1, Woodford 145.3 ft sample within a K-feldspar grain (light gray in BSE image) located in the clay matrix of the sample. The mineral formula for K-feldspar is $K(AlSi_3)O_8$.

3.3 WAVELENGTH DISPERSIVE X-RAY SPECTROMETRY (WDS) DATA

WDS was the principle quantitative tool employed to produce the micro-mineralogy logs shown above. The length of a micro-mineralogy log was determined by the length of the thin sections which ranged from 2 centimeters to approximately 2.3 centimeters. Although the Cameca SX50 electron microprobe is capable of conducting spot analyses as frequently as every 1 micrometer along an analysis line, a 75 micrometer spacing was chosen as it was at least one order of magnitude smaller than the thinnest lamination among all the sample intervals and presented the most practical resolution that time would allow for. Each 40 micrometer by 40 micrometer beam area is regarded as representative for the majority of spot analyses performed because clay grains range in diameter from nanometers to 4 micrometers and silt grains range in diameter from 4 micrometers to 62 micrometers (Potter et al., 1980). As some detritus and diagenetic mineral grains occur with diameters coarser than the beam area (tens to a few hundred micrometers in diameter), results should be quality controlled for such spot analyses that are not representative of a particular lamination, but rather a single coarse grain. Surface roughness was not regarded as a significant influence on the results of the WDS analytical transect lines due to the 2400 grit final surface polish completed on each sample.

Figure 52 paired with Table 2, Table 3, and Table 4 exhibit a calcite-clay laminated couplet from the 120.9 ft sample demonstrating the quantitative weight percent element, weight percent oxide, and calculated mineralogic fractionation results acquired from a WDS analytical transect line. Complete results for each sample can be found in Appendix A through Appendix I on the digital media attached to this thesis.

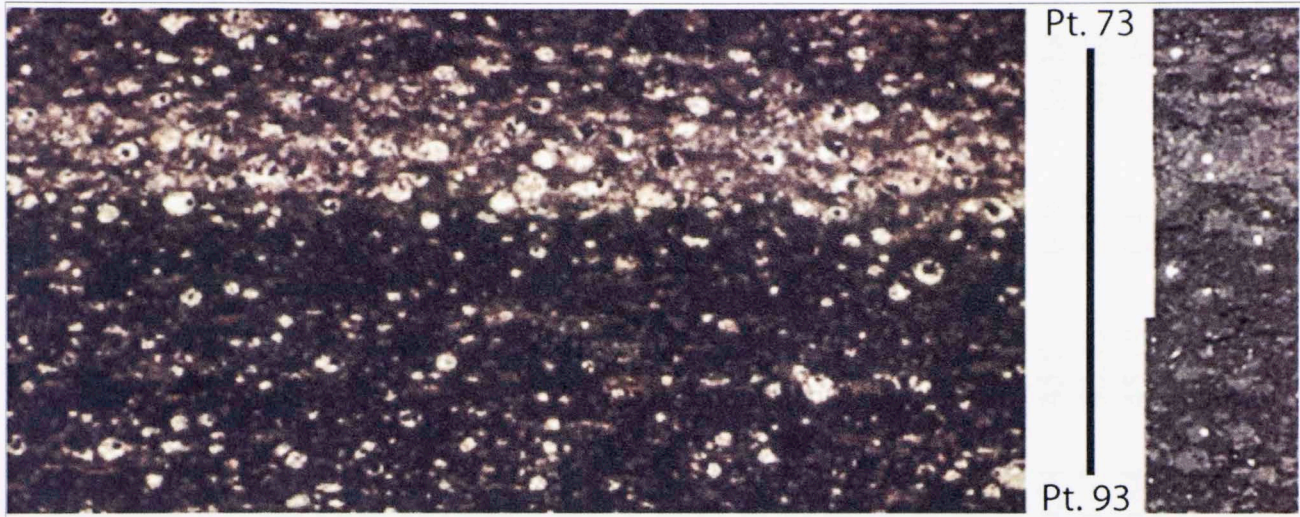


Figure 52. Crops of the scanned digital image of the 120.9 ft petrographic thin section (left) paired with its corresponding 120.9 ft electron microprobe thin section BSE image photomontage (right) showing the calcite-clay laminated couplet corresponding to the WDS data interval presented below.

3.3.1 120.9 FT SAMPLE CALCITE-CLAY COUPLETS WDS WEIGHT PERCENT

Table 2: WDS wt% results for calcite-clay couplets

Point	Depth (mm)	Si	Ti	P	Al	Fe	Mg	C
73	5800	1.16	0.00	0.00	0.55	0.21	0.15	7
74	5875	11.28	0.00	0.00	2.21	6.87	0.10	7
75	5950	20.14	0.00	0.00	4.25	8.39	0.20	10
76	6025	23.29	0.00	0.00	1.96	2.04	0.20	0
77	6100	22.72	0.00	0.00	0.51	0.15	0.14	16
78	6175	14.70	0.00	0.00	1.23	0.41	0.01	9
79	6250	20.11	0.00	0.00	0.70	0.46	0.20	11
80	6325	1.80	0.00	0.00	0.54	0.20	0.05	1.20
81	6400	20.46	0.00	0.00	0.69	0.74	0.20	12.00
82	6475	1.4	0.00	0.00	1.28	0.34	0.14	8.00
83	6550	18.20	0.00	0.00	2.17	1.71	0.19	1.4
84	6625	12.31	0.00	0.00	2.13	0.56	1.08	0.00
85	6700	19.60	0.00	0.00	2.31	0.90	0.41	0.20
86	6775	17.25	0.00	0.00	2.09	0.64	0.31	0.20
87	6850	16.10	0.00	0.00	2.07	0.68	0.25	0.20
88	6925	10.20	0.00	0.00	1.11	0.55	0.18	0.18
89	7000	12.20	0.00	0.00	2.50	0.95	0.20	0.20
90	7075	11.74	0.00	0.00	1.84	0.70	0.21	0.11
91	7150	17.99	0.00	0.00	1.48	0.29	0.16	0.12
92	7225	16.60	0.00	0.00	1.92	0.52	0.23	0.20
93	7300	17.23	0.00	0.00	2.26	0.45	0.20	0.20

3.3.1 120.9 FT SAMPLE CALCITE-CLAY COUPLET WDS WEIGHT PERCENT ELEMENT RESULT

Table 2. Wyche-1 well, WDS weight percent element result for one calcite-clay laminated couplet in the 120.9 ft sample.

Point	Depth (µm)	Si	Ti	P	Al	Fe	Mg	Ca	Na	K	O	S	Total
73	5400	32.65	0.02	0.00	0.85	0.27	0.15	7.96	0.10	0.29	41.41	0.26	83.95
74	5475	33.58	0.06	0.03	2.21	0.87	0.30	3.17	0.31	0.74	42.27	0.81	84.35
75	5550	29.14	0.00	0.01	0.32	0.38	2.26	10.51	0.07	0.11	39.32	0.12	82.24
76	5625	35.09	0.09	0.00	1.96	2.04	0.26	0.21	0.16	0.71	42.82	1.92	85.27
77	5700	25.75	0.02	0.02	0.53	0.16	0.14	16.13	0.07	0.18	36.48	0.10	79.57
78	5775	30.43	0.09	0.01	1.23	0.43	0.21	9.21	0.11	0.44	39.89	0.32	82.35
79	5850	26.11	0.03	0.00	0.70	0.46	0.20	14.85	0.14	0.20	36.68	0.35	79.72
80	5925	41.86	0.02	0.01	0.55	0.20	0.05	1.20	0.15	0.15	48.86	0.28	93.34
81	6000	28.06	0.03	0.01	0.99	0.74	0.20	12.03	0.11	0.34	38.14	0.70	81.34
82	6075	35.41	0.03	0.01	1.28	0.34	0.16	4.67	0.11	0.54	43.72	0.25	86.50
83	6150	34.21	0.08	0.00	2.17	1.71	0.28	1.47	0.15	0.87	42.45	1.47	84.85
84	6225	32.02	0.05	0.01	2.13	0.56	1.08	2.99	0.16	0.76	40.69	0.52	80.97
85	6300	34.50	0.15	0.01	2.81	0.90	0.41	0.27	0.18	1.11	42.84	0.68	83.86
86	6375	37.25	0.10	0.01	2.39	0.64	0.31	0.41	0.18	1.02	45.46	0.59	88.34
87	6450	36.39	0.06	0.00	2.07	0.68	0.28	0.21	0.17	0.88	44.04	0.63	85.41
88	6525	30.23	0.05	0.01	1.31	0.55	0.18	0.18	0.13	0.48	36.15	1.04	70.31
89	6600	33.46	0.66	0.01	2.50	0.95	0.39	0.27	0.21	0.97	41.69	0.82	81.92
90	6675	33.74	0.07	0.01	1.84	0.70	0.21	0.11	0.16	0.92	40.76	0.92	79.44
91	6750	37.99	0.04	0.01	1.48	0.29	0.18	0.12	0.13	0.54	45.03	0.38	86.18
92	6825	36.03	0.07	0.00	1.92	0.57	0.27	0.26	0.18	0.67	43.45	0.57	84.00
93	6900	37.22	0.12	0.00	2.26	0.45	0.30	0.33	0.19	0.84	45.19	0.44	87.36

3.3.2 120.9 FT SAMPLE CALCITE-CLAY COUPLET WDS WEIGHT PERCENT OXIDE RESULT

Table 3. Wyche-1 well, WDS weight percent oxide result for one calcite-clay laminated couplet in the 120.9 ft sample.

Point	Depth (µm)	SiO ₂	TiO ₂	P ₂ O ₅	Al ₂ O ₃	FeO*	MgO	CaO	Na ₂ O	K ₂ O	S ²⁻	Total
73	5400	69.85	0.03	0.00	1.61	0.34	0.25	11.14	0.13	0.35	0.26	92.69
74	5475	71.83	0.10	0.06	4.18	1.12	0.50	4.44	0.41	0.89	0.81	87.83
75	5550	62.33	0.00	0.01	0.60	0.49	3.74	14.70	0.10	0.14	0.12	93.77
76	5625	75.06	0.15	0.00	3.70	2.63	0.43	0.30	0.21	0.86	1.92	85.50
77	5700	55.09	0.03	0.05	1.00	0.21	0.23	22.57	0.09	0.21	0.10	97.28
78	5775	65.09	0.16	0.02	2.31	0.55	0.35	12.88	0.15	0.52	0.32	92.46
79	5850	55.86	0.05	0.01	1.33	0.59	0.33	20.78	0.19	0.24	0.35	96.02
80	5925	89.54	0.03	0.03	1.05	0.26	0.09	1.68	0.20	0.18	0.28	94.66
81	6000	60.04	0.04	0.02	1.87	0.95	0.34	16.83	0.15	0.41	0.70	94.54
82	6075	75.74	0.05	0.01	2.41	0.43	0.27	6.53	0.15	0.65	0.25	91.63
83	6150	73.18	0.13	0.00	4.11	2.19	0.46	2.05	0.21	1.04	1.47	86.46
84	6225	68.50	0.08	0.01	4.02	0.72	1.79	4.18	0.21	0.92	0.52	84.25
85	6300	73.82	0.25	0.02	5.30	1.16	0.68	0.37	0.24	1.33	0.68	84.15
86	6375	79.69	0.17	0.02	4.51	0.82	0.51	0.58	0.24	1.22	0.59	88.79
87	6450	77.84	0.10	0.00	3.91	0.87	0.47	0.30	0.23	1.06	0.63	85.64
88	6525	64.66	0.09	0.03	2.48	0.71	0.31	0.25	0.17	0.58	1.04	70.50
89	6600	71.57	1.10	0.02	4.72	1.22	0.65	0.38	0.28	1.17	0.82	82.22
90	6675	72.18	0.11	0.02	3.48	0.90	0.35	0.16	0.21	1.11	0.92	79.56
91	6750	81.27	0.06	0.01	2.79	0.38	0.29	0.17	0.17	0.65	0.38	86.32
92	6825	77.08	0.12	0.00	3.63	0.73	0.45	0.36	0.25	0.81	0.57	84.28
93	6900	79.63	0.21	0.00	4.27	0.58	0.49	0.46	0.26	1.02	0.44	87.72

3.3.3 120.9 FT SAMPLE CALCITE-CLAY COUPLET CALCULATED MINERALOGIC FRACTIONATION

Table 4. Wyche-1 well, calculated mineralogic fractionation for one calcite-clay laminated couplet in the 120.9 ft sample.

Point	Depth (µm)	% Clay	% Quartz	% Pyrite	% Dolomite	% Apatite	% Calcite	% Organics
73	5400	8.7	64.9	0.5	0.2	0.0	19.8	6.0
74	5475	22.6	59.0	1.5	0.0	0.1	7.8	9.0
75	5550	3.2	60.5	0.2	21.8	0.0	12.0	2.2
76	5625	20.0	63.7	3.6	0.0	0.0	0.5	12.2
77	5700	5.4	52.0	0.2	0.5	0.1	39.8	1.9
78	5775	12.5	58.0	0.6	0.2	0.0	22.8	5.9
79	5850	7.2	51.8	0.6	0.9	0.0	36.5	3.0
80	5925	5.7	86.3	0.5	0.0	0.1	2.9	4.5
81	6000	10.1	54.3	1.3	0.5	0.0	29.7	4.1
82	6075	13.1	68.3	0.5	0.0	0.0	11.6	6.5
83	6150	22.2	60.6	2.8	0.0	0.0	3.7	10.8
84	6225	21.7	56.1	1.0	7.4	0.0	2.6	11.1
85	6300	28.7	57.5	1.3	0.0	0.0	0.6	11.9
86	6375	24.4	65.8	1.1	0.0	0.0	1.0	7.7
87	6450	21.2	65.8	1.2	0.0	0.0	0.5	11.3
88	6525	13.4	57.0	1.9	0.0	0.1	0.4	27.2
89	6600	25.5	57.1	1.5	0.1	0.0	0.6	15.2
90	6675	18.8	61.5	1.7	0.0	0.0	0.2	17.7
91	6750	15.1	72.7	0.7	0.0	0.0	0.3	11.2
92	6825	19.6	65.9	1.1	0.0	0.0	0.6	12.8
93	6900	23.1	66.5	0.8	0.0	0.0	0.8	8.8

3.4 MICRO-MINERALOGY LOGS

After completing the WDS analytical transects, the resulting elemental oxide weight percent data was applied to the mineralogical equations discussed in Section 2.7 and sub-100 micrometer scale mineralogy logs were produced for each electron probe micro-analyzed thin section sample. These mineralogy logs were then correlated with their respective digitally-scanned petrographic thin section images as well as with their BSE photomontage images acquired in conjunction with the WDS analyses. The BSE image photomontages for each respective WDS analysis can be seen in appendices J, K, and L. Figure 53, Figure 54, and Figure 55 show the correlations of all three data types for the Wyche-1, 120.9 ft, 135.7 ft, and 145.3 ft samples respectively.

3.4.1 120.9 FT MICRO-MINERALOGY LOG

The Wyche-1, 120.9 ft micro-mineralogy log, correlated to its corresponding digitally-scanned petrographic thin section and BSE image photomontage taken along the WDS analytical transect, is shown in Figure 53. From bottom to top, Figure 53 shows an increase in calcite content with peaks identifying individual calcite laminations, an overall increase in quartz content corresponding to decreases in clay content, a subtle decrease in overall pyrite content, and decreases in organics also correspond to the decreases in clay content.

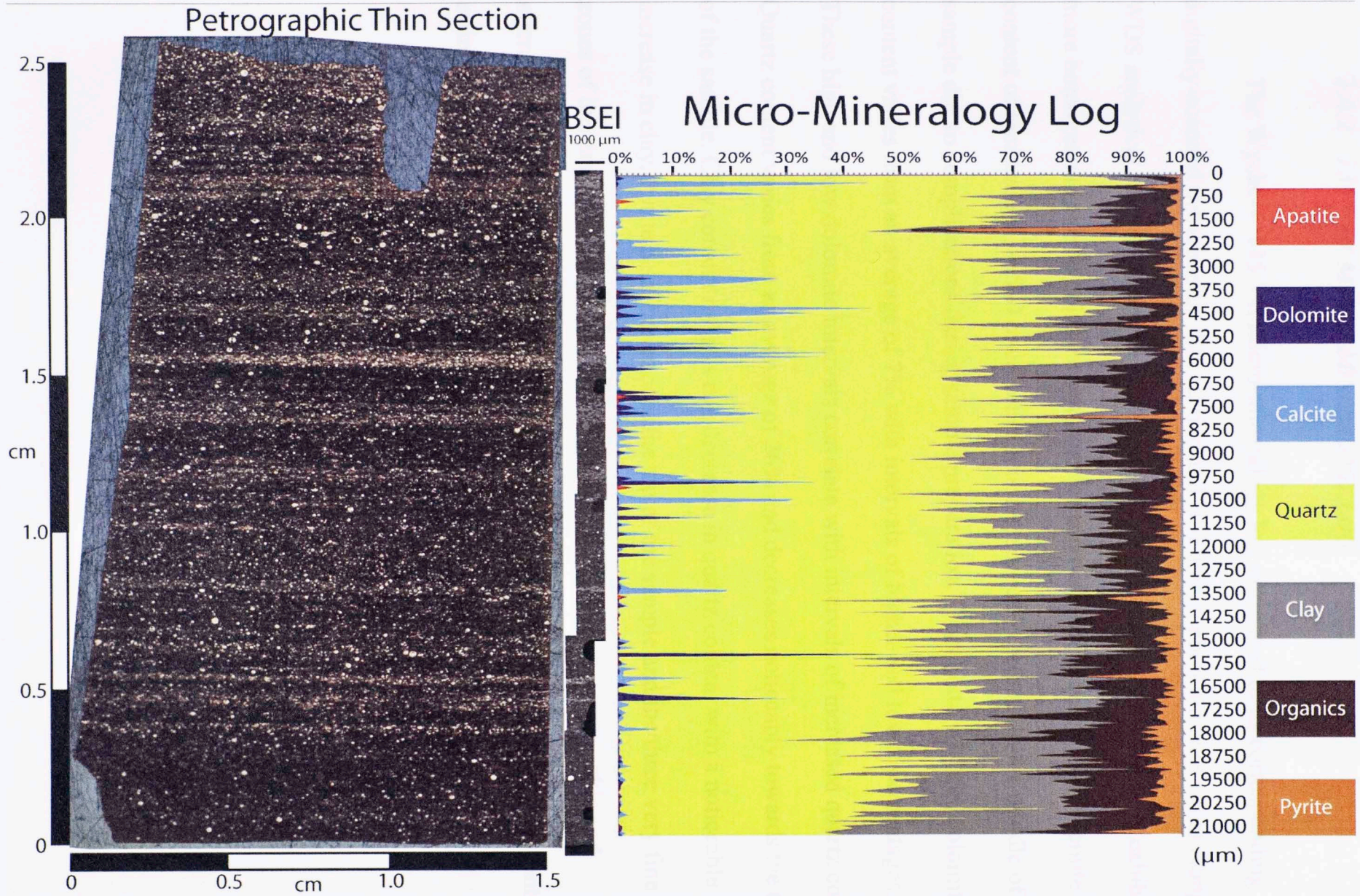


Figure 53. Wyche-1 well, Woodford 120.9 ft micro-mineralogy log from WDS analysis.

3.4.2 135.7 FT MICRO-MINERALOGY LOG

The Wyche-1, 135.7 ft micro-mineralogy log, correlated to its corresponding digitally-scanned petrographic thin section and BSE image photomontage taken along the WDS analytical transect, is shown in Figure 54. From bottom to top, Figure 54 exhibits a more homogenous overall behavior with subtle variations in the quartz and dolomite content of laminations. A 500 micrometer missing section is present in the middle of the sample due to complications during sample preparation. From bottom to top, dolomite content varies from an average of 7% with intervals of higher and lower percentages. These high and low dolomite intervals correlate with intervals of increased quartz content. Quartz content varies from an average of 26% and decreases noticeably towards the top of the sample. Clay content reflects this decrease in quartz content with a noticeable increase in clay. Pyrite also increases at the top of the sample and the three very fine zones of increased, coarser grained pyrite noted in the previous petrographic and microprobe imaging section are captured by the log. Finally, the organic carbon content estimate remains relatively unchanged with an average of 6%.

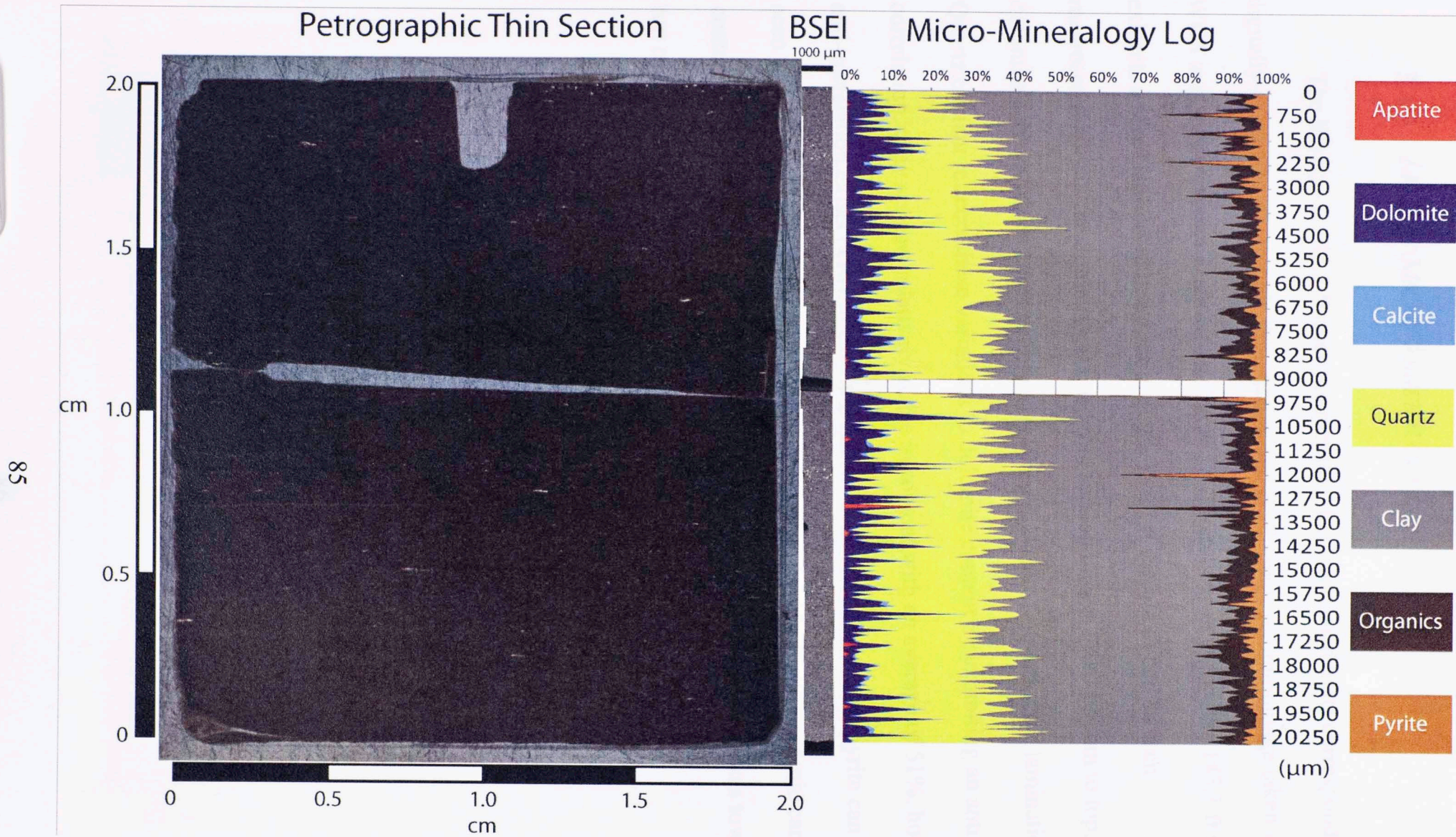


Figure 54. Wyche-1 well, Woodford 135.7 ft sample microprobe analysis.

3.4.3 145.3 FT MICRO-MINERALOGY LOG

The Wyche-1, 145.3 ft micro-mineralogy log, correlated to its corresponding digitally-scanned petrographic thin section and BSE image photomontage taken along the WDS analytical transect is shown in Figure 55. From bottom to top, the 145.3 ft sample exhibits a more laminated behavior than the 135.7 ft sample as can be seen macroscopically in the digitally-scanned thin section image. From bottom to top, dolomite content varies considerably, recording multiple, fine-dolomite laminations. Quartz content reflects these variations in dolomite content by exhibiting an anti-correlation. Clay appears relatively stable in content with an average of 51%, however, an anti-correlation exists between clay and quartz. Intervals of increased pyrite can also be seen with higher frequency as one moves up the sample. Finally, the organic carbon content estimate increases from the base, peaks in the middle, and decreases towards the top of the sample.

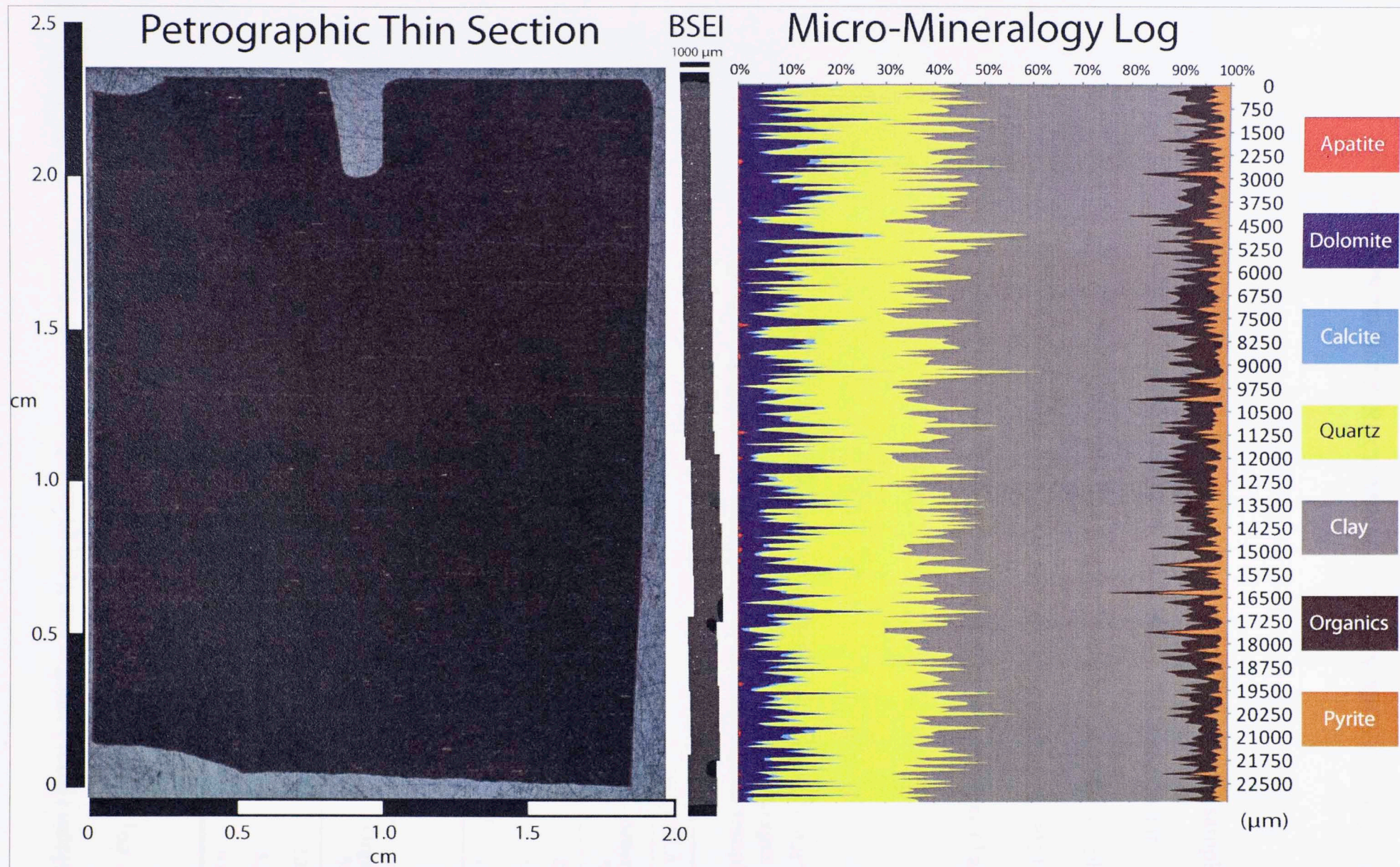


Figure 55. Wyche-1 well, Woodford 145.3 ft sample electron microprobe analysis.

3.5 COMPARISON TO BULK-ROCK MINERALOGY BY XRD FROM SIERRA (2011)

XRD bulk-rock mineralogy was performed by Sierra (2011) on core samples that correspond to the same sample intervals analyzed in this thesis. XRD analysis is accomplished by grinding rock samples into fine powder in order to acquire sample mineralogy without preferred orientation. The XRD mineralogy from Sierra (2011) (Table 5, top) offers a comparison to the WDS micro-mineralogy log averages (Table 5, bottom).

Table 5. Top: Sierra (2011) XRD bulk-sample mineralogy results (%) from "sister" core samples to those analyzed by electron microprobe in this thesis. Bottom: Averages of WDS micro-mineralogy per mineral phase in from each electron microprobe sample interval.

Sierra (2011) XRD bulk-sample mineralogy for samples 120.9 ft, 135.7 ft, and 145.3 ft:									
Depth (ft)	Depth (m)	Quartz %	K-spar %	Plag. %	Total Carb. %	Pyrite %	Sum Non-Clay	Sum Clay %	Amorphous %
120.9	36.85	53	3	0	5	3	65	12	21
135.7	41.36	36	2	2	11	3	53	32	15
145.3	44.28	32	2	2	7	3	47	38	15

Averages of WDS micro-mineralogy for samples 120.9 ft, 135.7 ft, and 145.3 ft:									
Depth (ft)	Depth (m)	Quartz %	Apatite %	Total Carb. %	Pyrite %	Sum Non-Clay	Clay %	Organics %	
120.9	36.85	59.7	0.1	5.9	3.1	68.8	20.4	10.9	
135.7	41.36	26.4	0.2	8.6	3.1	38.2	56.2	5.5	
145.3	44.28	27.8	0.2	12.0	2.5	42.5	51.2	6.4	

Discrepancies between the XRD and averaged WDS micro-mineralogy log values are present largely in the clay, quartz, amorphous (XRD), and organic (WDS) categories.

Clay values determined from the micro-mineralogy logs will include the minor plagioclase and K-feldspar phases shown in the XRD analyses and thus, clay from WDS will be overestimated. XRD analyses, however, have functional detection limits near 10 wt% for a particular mineral phase so minor/trace mineral abundances are suspect by XRD (Morgan, personal communication, 2010). Also, the XRD analyses likely overestimate the amorphous phases. Amorphous phases are those that lack characteristic crystalline structures or are too fine grained to yield definitive results (e.g., chalcedony, organics, organic-rich phosphates). As micro-fibrous chalcedony lacks crystal structure, it is quite possible that the XRD analyses included a significant percentage of SiO₂ into the amorphous category. In this way, SiO₂ as quartz percentages would be underrepresented and amorphous percentages would be overrepresented in the XRD results. Similarly, the main source of error in WDS mineralogic micro-logging resides in the organic estimate as elements not analyzed and minor mineral phases not calculated from the existing WDS elemental analyses reside in this remainder after calculated mineral phases are subtracted from 100 wt%. Thus, the organic percentage in the micro-mineralogy logs is overestimated.

As XRD analysis is the standard technique used to acquire mineralogy for most shale gas research investigations, the micro-scale resolution offered by micro-mineralogic logging presents a more detailed approach to fine-grain rock mineralogical analysis that includes the added benefit of preserving rock fabric for petrologic study by SEM.

3.6 WDS X-RAY INTENSITY MAPPING

The final approach towards characterizing fine-grained mineralogy in the Wyche-1 well with the electron microprobe was performed by X-ray intensity mapping on a calcite-clay laminated couplet. The resulting image data is presented in Figure 56.

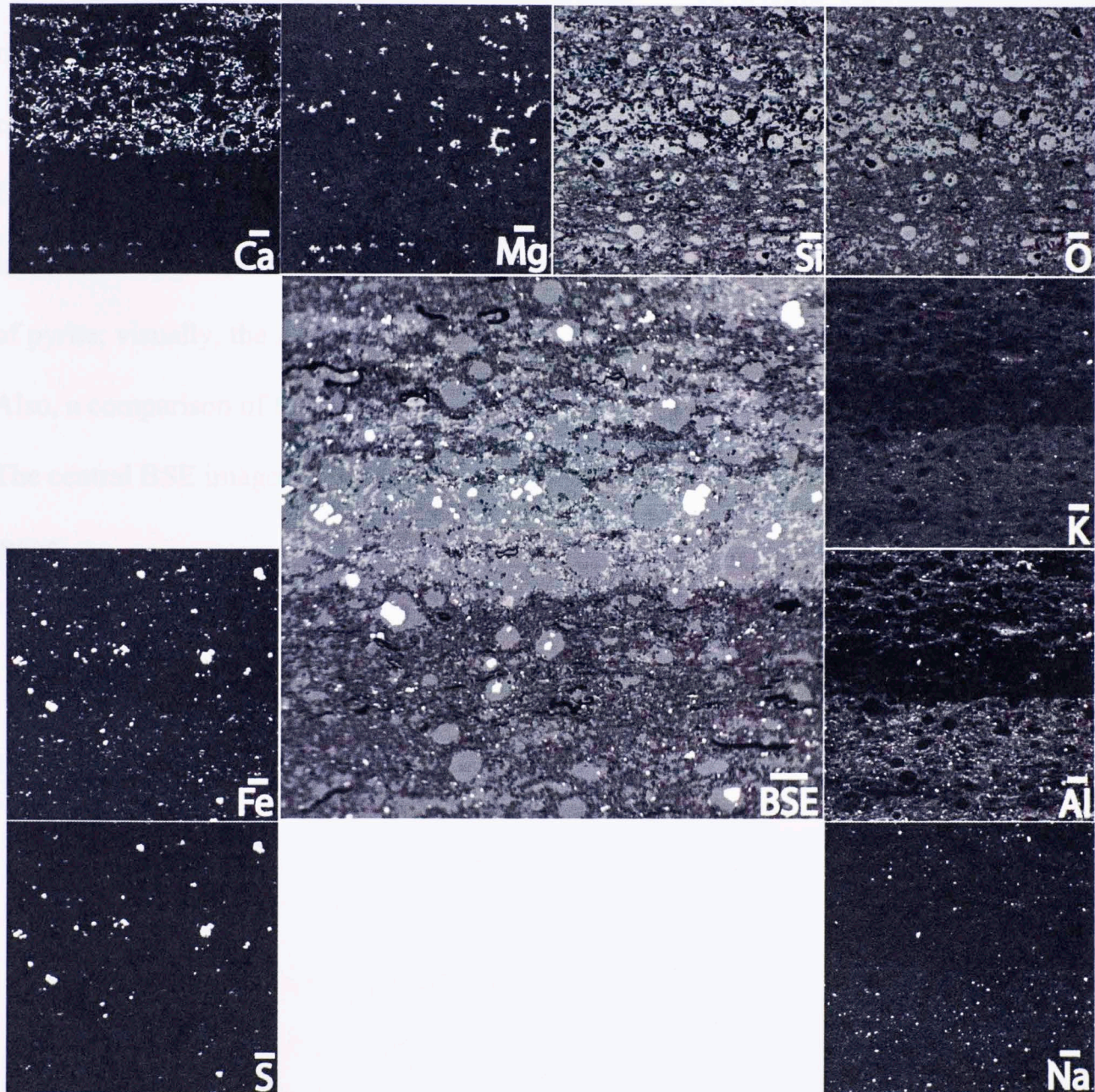


Figure 56. X-ray intensity maps of elements Ca, Mg, Si, O, Fe, S, K, Al, and Na coupled with a BSE image of a calcite-clay laminated couplet in the Wyche-1, 120.9 ft sample. All scale bars = 100 μm . The BSE image was acquired at a 1024 px by 1024 px resolution. The X-ray intensity maps were acquired at 512 px by 512 px resolutions.

With an understanding of the stoichiometric formulas for each mineral phase present in the sample, one can use the X-ray mapping intensity images to understand the behaviors of various mineral phases visually. For example, in Figure 56, the bright spots in the magnesium X-ray intensity map overlap well with the bright spots in the calcium X-ray intensity map as the bright spots in both images are probable locations of carbonate minerals. However, the bright spots in the magnesium map differentiate dolomite from calcite much like an alizarin-red stain in carbonate thin sections differentiates calcite from dolomite. Similarly, visually adding the Si and O X-ray intensity maps yields the locations of quartz; visually adding the Fe and S X-ray intensity maps yields the locations of pyrite; visually, the Al and K X-ray intensity maps show the locations of clay minerals. Also, a comparison of the Fe and S maps indicate that pyrite is the principal host for Fe. The central BSE image in Figure 56 is displayed for comparison to the X-ray intensity maps.




4. DISCUSSION

The micro-mineralogy logs as well as the semi-quantitative EDXA data, semi-qualitative BSE image data, and semi-qualitative X-ray intensity mapping data produced from the electron microprobe combined with traditional petrographic microscope examinations all performed in this thesis are the next important additions to the integrated and multi-scale reservoir characterization of gas shales. The sub-100 micrometer resolution offered by the electron microprobe allows for mineralogical evaluation of fine-grained rocks for micro-scale stratigraphic analysis and possible lamination-scale geomechanical modeling like that of Sierra (2011) performed on the sequence-stratigraphic, parasequence scale.

4.1 120.9 FT CALCITE-CLAY LAMINATED SAMPLE MICRO-STRATIGRAPHY

The 120.9 ft calcite-clay laminated sample is located at the base of the Upper Woodford Shale in the Wyche-1 core. Based on Wyche-1 well core descriptions by Nicole Buckner and work done for this thesis, the base of the Upper Woodford interval marks the start of upward increased calcareous laminations within the Wyche-1 core. Sample 120.9 ft shows this calcite-clay laminated couplet behavior both macroscopically in the digital thin section scan (Figure 14) and microscopically with each individual lamination recorded by the WDS micro-mineralogy log (Figure 53).


The abundance of organic matter, quartz- and pyrite-filled Tasmanites algal cysts as well as calcite laminations throughout the 120.9 ft sample, have important implications



for interpretations of organic productivity, diagenetic timing, rate of deposition, and the environment of deposition during the accumulation of the Upper Woodford unit.

First, the presence of so much organic matter (the sample averages 11% from micro-mineralogy log point analysis estimates) indicates that anoxic conditions prevailed at the time of deposition, thus preserving the organic matter as it rained down from more photic, oxygenated, and organically productive zones higher in the water column (Kirkland et al., 1992). In such conditions, sulfate reducing bacteria would have been the dominant microbial agents at work from the sea floor through the shallow sediment interval, influencing the precipitation of both pyrite (Kirkland et al., 1992; Schieber, 1996; Machel, 2001; Schieber and Baird, 2001) and quartz (Schieber, 1996) in spherical Tasmanites cysts after they were deposited on the sea floor.

The degradation of Tasmanites cyst organic matter by sulfate reducing bacteria likely emitted gases such as H_2S and CO_2 (Schieber, 1996; Machel, 2001). These gases helped to preserve the spherical shape of the Tasmanites cysts allowing diagenetic deposition of quartz and pyrite to completely fill cyst void space before compaction due to increased overburden could influence their shape (Schieber, 1996). The dominance of quartz-filled Tasmanites cysts in comparison to pyrite-filled cysts throughout the shale matrix in sample 120.9 ft is very likely due to abundant deposition of kinetically unstable, opal A radiolarian tests along with the algal cysts. Detailed radiolarian studies by Urban (1960), Schwartzapfel and Holdsworth (1996), as well as observations by Kirkland et al. (1992) have been conducted in Arbuckle Mountain and Criner Hills Woodford Shale outcrops between 30 to 50 miles southeast of the Wyche-1 well and indicate that an abundance of radiolarian species are present in coeval Woodford Shale intervals.



Recovered radiolarian specimens from those studies were typically associated only with phosphate and chert nodules that likely protected the opal-A radiolarian tests from rapid dissolution (Schieber, 1996). In fact, the presence of discrete quartz-filled Tasmanites cyst lamina, versus the much more abundant, fully-compacted, elongate and flattened Tasmanites cysts seen throughout different clay intervals of the Wyche-1 core, is evidence that the laminations enriched in quartz-filled cysts are intervals of increased radiolarian deposition. Opal-A radiolarian tests not incorporated into nodules most likely dissolved relatively soon after deposition, precipitating initially as chalcedony on the inner side of Tasmanites cyst organic walls and then as macro-quartz in the remaining cyst void space (Schieber, 1996). After a thick layer of chalcedony formed, the internal cyst void space became isolated from the soupy, pre-lithified shale matrix. This prevented any additional silica from entering the cyst through the porous organic wall, causing the remaining cyst void space to fill with macro- or single-grain quartz precipitates (Schieber, 1996). Thus, in order to allow for the preservation of so many spherical Tasmanites cysts like those seen in the 120.9 ft sample interval, diagenetic precipitation of quartz must have been very early after deposition, most likely in the upper 20 centimeters of the sediment column based on an assumed sedimentation rate of 10^{-3} mm/yr and a pre-compaction porosity of 60 to 70 percent (Schieber, 1996).

Likewise, for pyrite-filled Tasmanites spheres to preserve their shape throughout compaction, diagenetic pyrite precipitation would also have occurred relatively soon after cyst deposition and in the upper 20 centimeters of the sediment column (Schieber and Baird, 2001). Schieber (1996) and Schieber and Baird (2001) advocate pyrite formation in Tasmanites cysts first as small pyrite framboid growths that were then bonded together

by a second stage pyrite cement that filled and conformed to the morphology of the sphere. The anhedral pyrite found in dominantly pyrite-filled, spherical *Tasmanites* cysts (Figure 17a,b,d, Figure 18a, Figure 23a, and Figure 25a,b) of the 120.9 ft sample interval, as well as observations by Machel (2001) of multiple stage pyrite formation in bacterial sulfate reducing (BSR) environments, supports such an interpretation.

A range of quartz-pyrite ratios exist among partially- to completely-filled *Tasmanites* cysts in the 120.9 ft sample interval. The vast majority of cysts are quartz-filled with minor to major amounts of euhedral pyrite grains observed along the organic walls of the cysts, suspended within quartz-filled cysts, or combinations of both. In BSE examination of the microprobe thin section and petrographic examination of standard thin section, the depth of observation is very shallow due to the fact that the former detects electrons only from the upper few micrometers of the sample and the latter is too thin to observe significant three-dimensional morphologies of pyrite grains. Transmitted, plane-polarized light microscope examination of the thicker (approximately 50 micrometers) microprobe thin section allows three-dimensional morphologies of pyrite to be observed within the translucent, quartz-filled cysts. This examination led to the understanding that the pyrite grains, which formed in dominantly quartz-filled cysts, are euhedral and even occur within quartz growth rings (Figure 57).

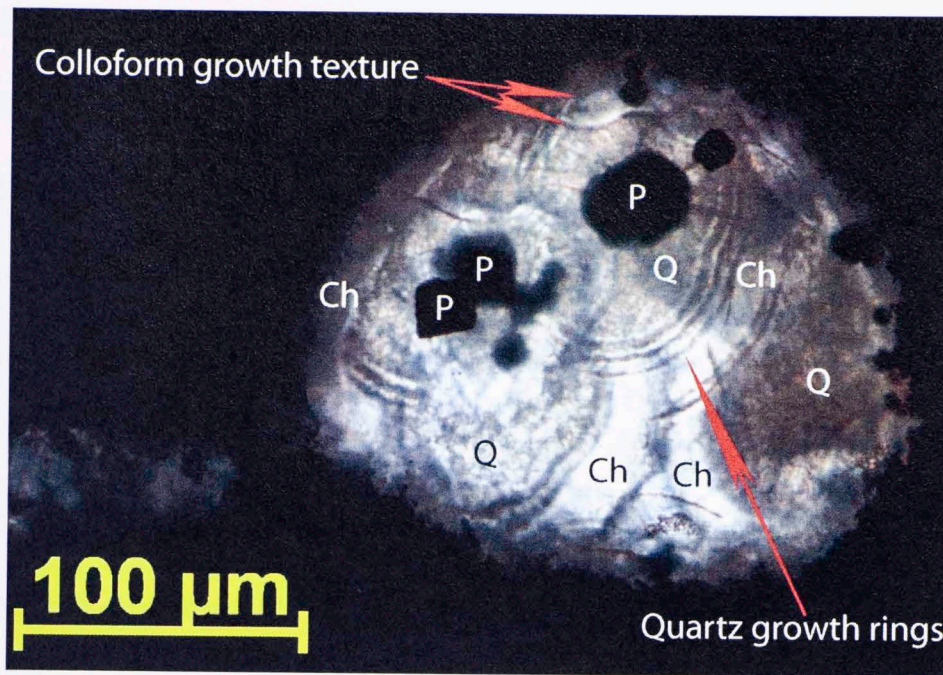


Figure 57. Photomicrograph of the 50 μm thick, electron microprobe thin section (PPL) showing quartz growth rings with euhedral pyrite grains at their center in a dominantly quartz-filled Tasmanites cyst. A colloform growth texture of the outer chalcedony rim is also visible in some parts of the grain. P = pyrite, Q = quartz, Ch = chalcedony.

This finding implies that initial rim chalcedony precipitated first followed by pyrite frambooid and secondary macro- or single-grain quartz. In Figure 57, the image suggests that secondary quartz grew in rings inward until the final pore space precipitated pyrite. However, other observations indicate pyrite growth can occur at any time during precipitation of chalcedony or other quartz phases. Although Schieber (1996) and Schieber and Baird (2001) advocate a geopetal growth pattern of pyrite fambooids inside Tasmanites cysts, no consistent geopetal pattern was observed regarding authigenic pyrite growth in the 120.9 ft sample interval. As pyrite is generally thought to precipitate instantaneously in a geologic sense, chemical factors during the deposition of this interval apparently delayed the growth of pyrite and caused chalcedony or quartz to be the earliest diagenetic mineral phase within the Tasmanites cysts in some cases (Schieber, 1996). Also, pyrite growth in contact with inner Tasmanites cyst organic walls may have been

due to the biodegradation of inner wall-attached organic matter and thus produced random orientations of fine pyrite grains throughout many different cysts.

Tasmanites cyst walls are chemically stable and resistant to bacterial decomposition, shown by their abundant preservation and nonreactive behavior with sodium hypochlorite and sodium hydroxide mixtures (Teppan, 1980; Schieber, 1996). I hypothesize here that another, more readily degraded algal-organic material was present in the Tasmanites cysts and that the volume of this organic material controlled the volume of pyritization within the cysts. Tappan (1980) discussed the life cycle of Tasmanites and how the ancient green algae originated as a motile quadriflagellate that transitioned into a spherical cyst with a thick, protective outer wall, which allowed new motile cells to develop during environmentally harsh conditions. The cyst then ruptured, allowing the new quadriflagellate cells to escape while the empty cyst rained through the water column to deposit on the sea floor (Tappan, 1980). A schematic cartoon of the Tasmanites life cycle from Tappan (1980) is shown in Figure 58. The thick portion of the cyst seen in parts 5, 7, and 8 of Figure 58 is a saucer shaped plastid that can be seen on edge view in part 6 (Tappan, 1980). Parts 7 and 8 show the quadriflagellate release sutures through the center of the cyst (Tappan, 1980).

Figure 58. Tasmanites growth cycle. (a) (b) (c) (d) (e) (f) (g) (h) (i) (j) (k) (l) (m) (n) (o) (p) (q) (r) (s) (t) (u) (v) (w) (x) (y) (z) (aa) (ab) (ac) (ad) (ae) (af) (ag) (ah) (ai) (aj) (ak) (al) (am) (an) (ao) (ap) (aq) (ar) (as) (at) (au) (av) (aw) (ax) (ay) (az) (ba) (bb) (bc) (bd) (be) (bf) (bg) (bh) (bi) (bj) (bk) (bl) (bm) (bn) (bo) (bp) (bq) (br) (bs) (bt) (bu) (bv) (bw) (bx) (by) (bz) (ca) (cb) (cc) (cd) (ce) (cf) (cg) (ch) (ci) (cj) (ck) (cl) (cm) (cn) (co) (cp) (cq) (cr) (cs) (ct) (cu) (cv) (cw) (cx) (cy) (cz) (da) (db) (dc) (dd) (de) (df) (dg) (dh) (di) (dj) (dk) (dl) (dm) (dn) (do) (dp) (dq) (dr) (ds) (dt) (du) (dv) (dw) (dx) (dy) (dz) (ea) (eb) (ec) (ed) (ee) (ef) (eg) (eh) (ei) (ej) (ek) (el) (em) (en) (eo) (ep) (eq) (er) (es) (et) (eu) (ev) (ew) (ex) (ey) (ez) (fa) (fb) (fc) (fd) (fe) (ff) (fg) (fh) (fi) (fj) (fk) (fl) (fm) (fn) (fo) (fp) (fq) (fr) (fs) (ft) (fu) (fv) (fw) (fx) (fy) (fz) (ga) (gb) (gc) (gd) (ge) (gf) (gg) (gh) (gi) (gj) (gk) (gl) (gm) (gn) (go) (gp) (gq) (gr) (gs) (gt) (gu) (gv) (gw) (gx) (gy) (gz) (ha) (hb) (hc) (hd) (he) (hf) (hg) (hh) (hi) (hj) (hk) (hl) (hm) (hn) (ho) (hp) (hq) (hr) (hs) (ht) (hu) (hv) (hw) (hx) (hy) (hz) (ia) (ib) (ic) (id) (ie) (if) (ig) (ih) (ii) (ij) (ik) (il) (im) (in) (io) (ip) (iq) (ir) (is) (it) (iu) (iv) (iw) (ix) (iy) (iz) (ja) (jb) (jc) (jd) (je) (jf) (jg) (jh) (ji) (jj) (jk) (jl) (jm) (jn) (jo) (jp) (jq) (jr) (js) (jt) (ju) (jv) (jw) (jx) (jy) (jz) (ka) (kb) (kc) (kd) (ke) (kf) (kg) (kh) (ki) (kj) (kk) (kl) (km) (kn) (ko) (kp) (kq) (kr) (ks) (kt) (ku) (kv) (kw) (kx) (ky) (kz) (la) (lb) (lc) (ld) (le) (lf) (lg) (lh) (li) (lj) (lk) (ll) (lm) (ln) (lo) (lp) (lq) (lr) (ls) (lt) (lu) (lv) (lw) (lx) (ly) (lz) (ma) (mb) (mc) (md) (me) (mf) (mg) (mh) (mi) (mj) (mk) (ml) (mm) (mn) (mo) (mp) (mq) (mr) (ms) (mt) (mu) (mv) (mw) (mx) (my) (mz) (na) (nb) (nc) (nd) (ne) (nf) (ng) (nh) (ni) (nj) (nk) (nl) (nm) (nn) (no) (np) (nq) (nr) (ns) (nt) (nu) (nv) (nw) (nx) (ny) (nz) (oa) (ob) (oc) (od) (oe) (of) (og) (oh) (oi) (oj) (ok) (ol) (om) (on) (oo) (op) (oq) (or) (os) (ot) (ou) (ov) (ow) (ox) (oy) (oz) (pa) (pb) (pc) (pd) (pe) (pf) (pg) (ph) (pi) (pj) (pk) (pl) (pm) (pn) (po) (pp) (pq) (pr) (ps) (pt) (pu) (pv) (pw) (px) (py) (pz) (qa) (qb) (qc) (qd) (qe) (qf) (qg) (qh) (qi) (qj) (qk) (ql) (qm) (qn) (qo) (qp) (qq) (qr) (qs) (qt) (qu) (qv) (qw) (qx) (qy) (qz) (ra) (rb) (rc) (rd) (re) (rf) (rg) (rh) (ri) (rj) (rk) (rl) (rm) (rn) (ro) (rp) (rq) (rr) (rs) (rt) (ru) (rv) (rw) (rx) (ry) (rz) (sa) (sb) (sc) (sd) (se) (sf) (sg) (sh) (si) (sj) (sk) (sl) (sm) (sn) (so) (sp) (sq) (sr) (ss) (st) (su) (sv) (sw) (sx) (sy) (sz) (ta) (tb) (tc) (td) (te) (tf) (tg) (th) (ti) (tj) (tk) (tl) (tm) (tn) (to) (tp) (tq) (tr) (ts) (tt) (tu) (tv) (tw) (tx) (ty) (tz) (ua) (ub) (uc) (ud) (ue) (uf) (ug) (uh) (ui) (uj) (uk) (ul) (um) (un) (uo) (up) (uq) (ur) (us) (ut) (uu) (uv) (uw) (ux) (uy) (uz) (va) (vb) (vc) (vd) (ve) (vf) (vg) (vh) (vi) (vj) (vk) (vl) (vm) (vn) (vo) (vp) (vq) (vr) (vs) (vt) (vu) (vv) (vw) (vx) (vy) (vz) (wa) (wb) (wc) (wd) (we) (wf) (wg) (wh) (wi) (wj) (wk) (wl) (wm) (wn) (wo) (wp) (wq) (wr) (ws) (wt) (wu) (wv) (ww) (wx) (wy) (wz) (xa) (xb) (xc) (xd) (xe) (xf) (xg) (xh) (xi) (xj) (xk) (xl) (xm) (xn) (xo) (xp) (xq) (xr) (xs) (xt) (xu) (xv) (xw) (xx) (xy) (xz) (ya) (yb) (yc) (yd) (ye) (yf) (yg) (yh) (yi) (yj) (yk) (yl) (ym) (yn) (yo) (yp) (yq) (yr) (ys) (yt) (yu) (yv) (yw) (yx) (yy) (yz) (za) (zb) (zc) (zd) (ze) (zf) (zg) (zh) (zi) (zj) (zk) (zl) (zm) (zn) (zo) (zp) (zq) (zr) (zs) (zt) (zu) (zv) (zw) (zx) (zy) (zz)

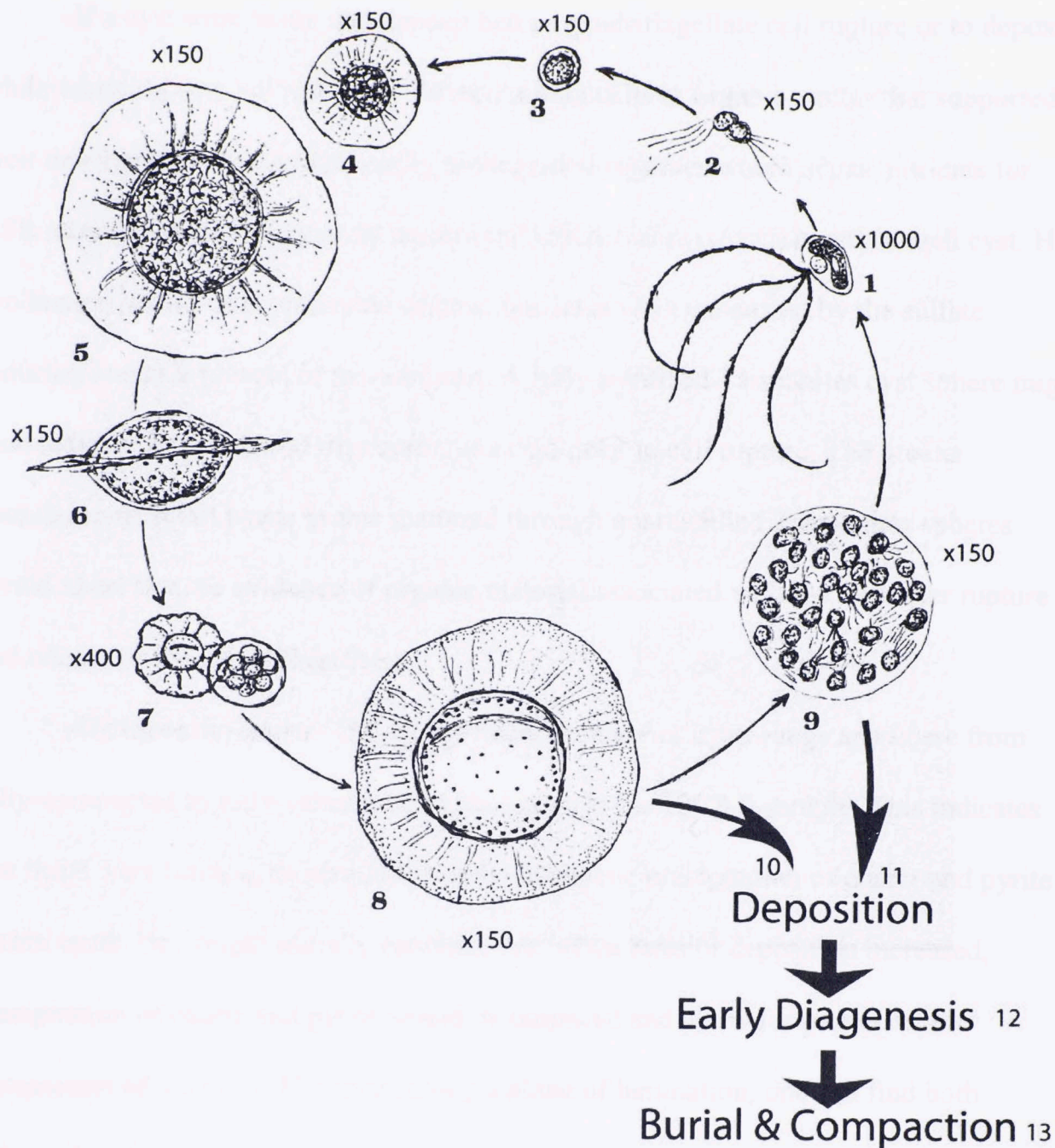


Figure 58. *Tasmanites* green algae life cycle modified from Tappan (1980). **1.** Motile quadriflagellate stage. **2.** Dividing motile cells. **3.** Start of cyst stage as cell loses motile parts and develops its thick, spherical wall. **4,5.** Mature cyst stage of various sizes. **6.** Cyst in edge view showing the saucer-shaped plastid. **7.** Release suture forms through the center of the cyst to release its inner cell wall that carries developing motile cells. **8.** Empty cyst showing release suture, outer wall pores, and saucer-shaped plastid in top-down view. **9.** Cyst inner wall that has grown to accommodate the division of more motile cells and the growth of their flagellum. These motile cells will ultimately burst this inner cyst wall and escape. **10.** Normal deposition of empty cysts. **11.** Deposition of quadriflagellate-filled cysts if death of the organism occurs before motile cell rupture. **12.** Inner cyst space fills with diagenetic quartz (from dissolved radiolarian opal A) and pyrite (due to bacterial sulfate reduction of inner cyst organics). **13.** Overburden buries cysts and compacts those that have not been completely filled with diagenetic minerals.

If a cyst were to die and deposit before quadriflagellate cell rupture or to deposit while retaining some of the newly formed motile cells or organic matter that supported their development, these more easily biodegraded organics would act as nutrients for BSR microbes and consequently control the volume of pyritization within each cyst. H_2S production would cease when the organic nutrients were exhausted by the sulfate reducing bacteria present in the substrate. A fully-pyritized Tasmanites cyst sphere might then indicate the death and deposition of a cyst prior to cell rupture. The greater abundance of small pyrite grains scattered through quartz-filled Tasmanites spheres would, therefore, be evidence of organic material associated with the cyst after rupture and release of the quadriflagellates.

Additionally, quartz- and pyrite-filled Tasmanites cysts range anywhere from fully-compacted to fully-spherical morphologies in the 120.9 ft sample. This indicates that there were limiting factors in the early diagenetic precipitation of quartz and pyrite within cysts. One might initially conclude that when rates of deposition increased, precipitation of quartz and pyrite would be outpaced and allow for partial to full compaction of the cysts. However, along a plane of lamination, one can find both spherical and compact morphologies. To reconcile this observation, an explanation to be considered is that some cysts were collapsed prior to deposition and burial. If rupture of a cyst due to quadriflagellate release was great enough, it is possible that the structural integrity of the flexible sphere would become compromised and collapse prior to deposition or with smaller amounts of overburden. However, this assumption is just a consideration to explain some possible conflicting morphologies along a similar plane of lamination. If a zone comprised of only fully-compacted cysts was observed, one could

either interpret an increased rate of deposition or a local deficiency in silica and/or sulfate such as a hiatus in radiolarian deposition or an interruption in bacterial sulfate reduction, respectively. This would prevent the precipitation of quartz and pyrite within cysts prior to burial and compaction. On the other hand, if a zone comprised of only diagenetically-filled spherical cysts was observed, one could interpret a decreased rate of deposition or a local influx in silica and/or sulfate such as increased radiolarian deposition due to a planktonic bloom or stimulated activity of BSR microbes, respectively. This would increase the precipitation of quartz and pyrite within cysts to a rate that would completely-fill cyst void space prior to reaching the critical overburden for cyst compaction. No such definitive fully-filled or fully-compacted zones, along planes of lamination, were observed in the 120.9 ft sample interval. Figure 59 shows a schematic summary of the deposition, early diagenesis, and burial/compaction processes for quartz- and pyrite-filled Tasmanites cyst end-members (*i.e.* only quartz- or only pyrite-filled Tasmanites cysts). It should be noted that combinations of both quartz and pyrite precipitation within mutual Tasmanites cysts is most commonly observed in the 120.9 ft sample interval.

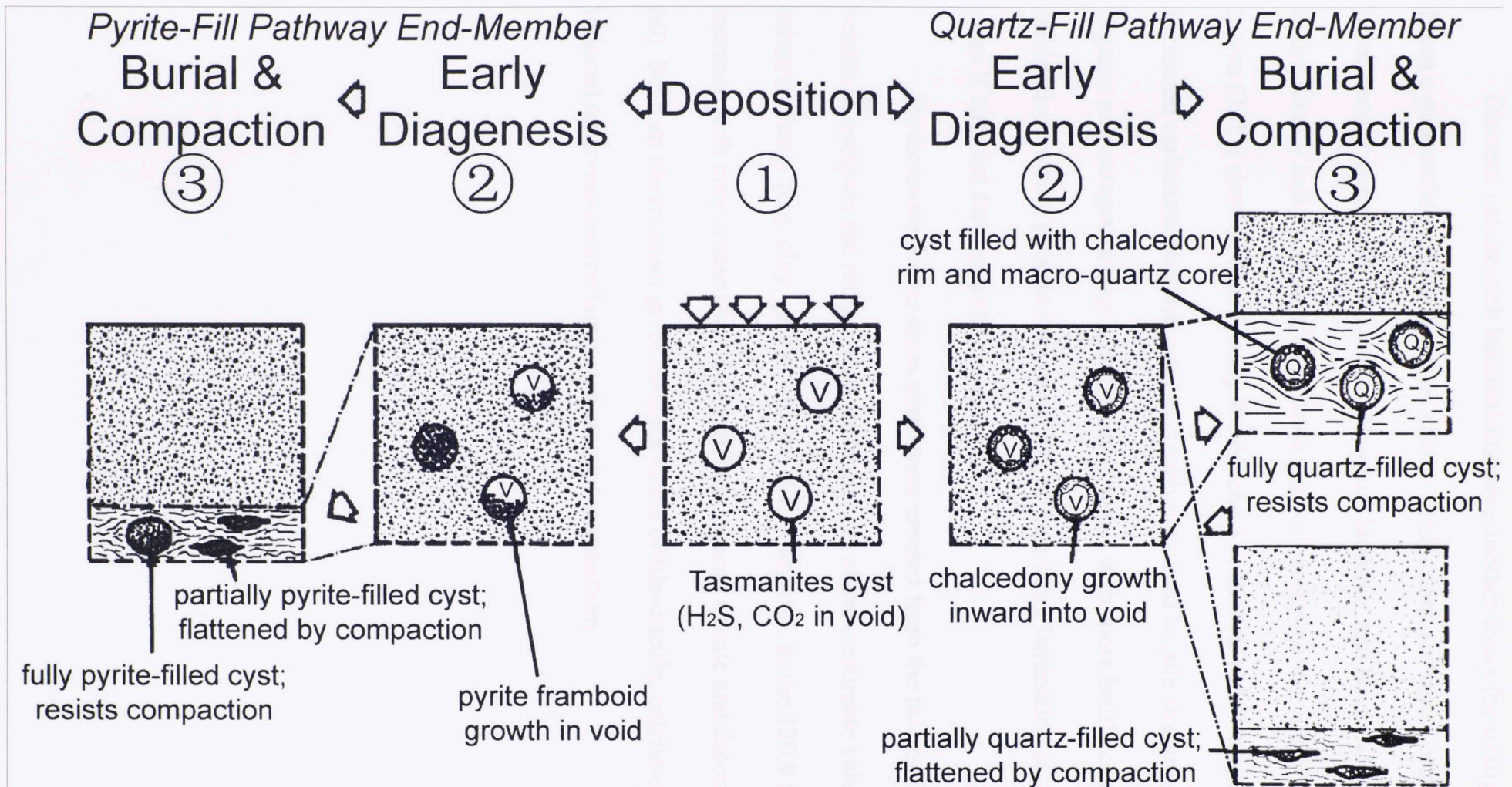


Figure 59. Schematic presentation of early diagenetic processes in quartz- and pyrite-filled Tasmanites algal cysts modified from Schieber (1996). **1.** Deposition of cysts on and into the soupy muds of the ocean-floor. **Quartz Pathway:** **2.** Chalcedony precipitates on the inner side of the cyst organic wall. **3.** Chalcedony precipitation stops and the remaining void space fills with macro-quartz. The cysts resist compaction and clays differentially compact around the cysts; chalcedony precipitation stops and the void space of the cyst allows for later compaction due to increased overburden. **Pyrite Pathway:** **2.** Pyrite framboids form in the cyst due to bacterial sulfate reduction of inner cyst organics. **3.** Cysts resist compaction if fully filled by pyrite; cysts compact if only partially filled by pyrite.

Discrete calcite-rich laminations were another focus for stratigraphic analysis. From a geomechanical perspective, calcite laminations are zones of relatively greater brittleness as compared to the more clay rich laminae, and have the potential to produce hydraulically induced fractures in shale gas well completions. Sierra et al. (2010) and Sierra (2011) showed that, among the Wyche-1, 120.9 ft, 135.7 ft, and 145.3 ft samples, increased carbonate content correlated with increased tensile strength. Thus, higher organic percentages in clay laminations coupled with more brittle calcite-cemented quartz laminations would present the possibility of becoming lamination scale source-reservoir pairs if targeted for hydraulic fracture.

Furthermore, linear cross plots were created from the micro-mineralogy log results to compare the relationships between the organic estimate values and other mineral phases (e.g. clay, quartz, calcite, and dolomite). In the 120.9 ft sample, organics increase with clay content and decrease with quartz, calcite and dolomite content (Figure 60). Such an observation gives strength to the brittle-ductile, calcite-clay, fracture induced reservoir-source laminated couplet supposition.

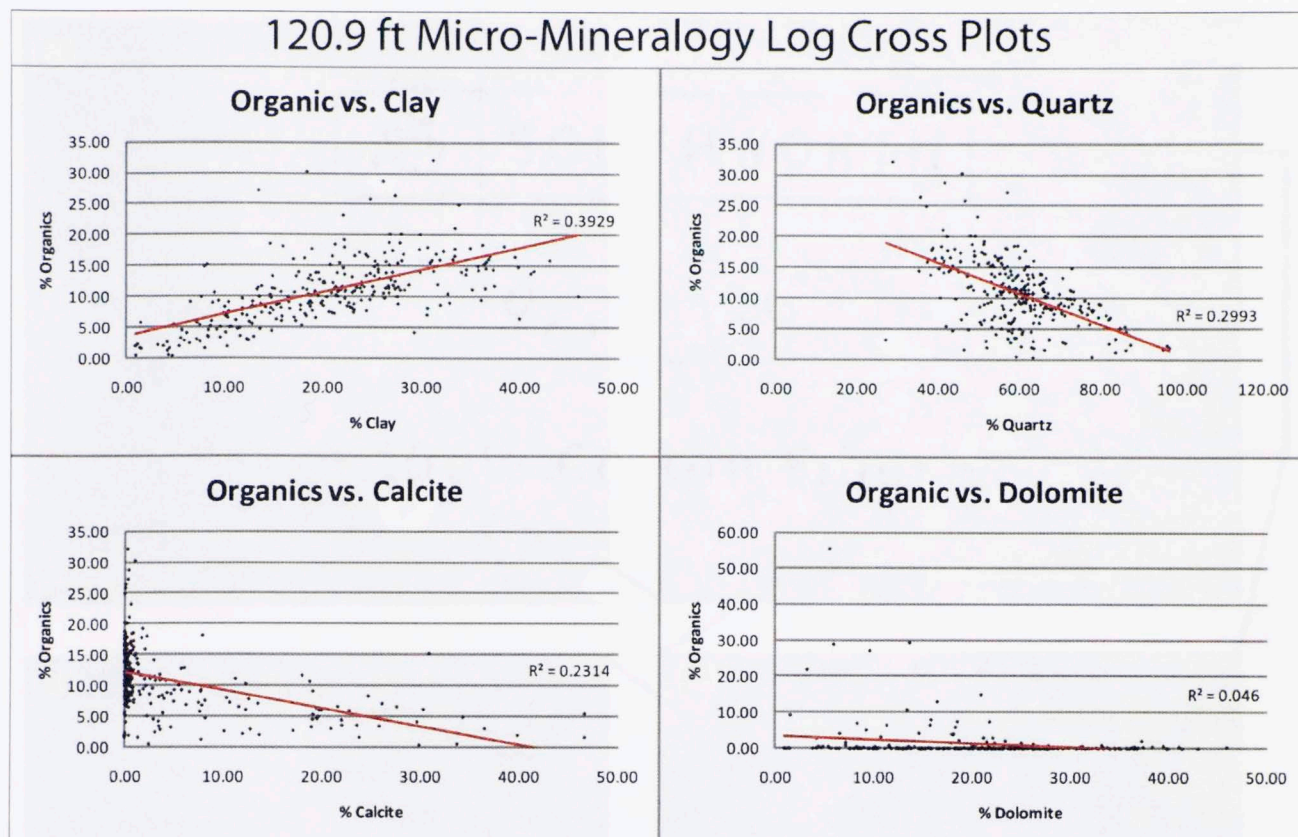


Figure 60. Linear cross plots from the 120.9 ft micro-mineralogy log results showing organics vs. clay, quartz, calcite, and dolomite.

Understanding the origin of the calcite is, therefore, important in order to predict the presence of calcite cemented zones from well-to-well in Devonian black shale hydrocarbon plays. Extensive study on the electron microprobe was devoted to documenting the nature of the calcite, which is generally spheroidal (circular), 10 to 20 micrometer in diameter calcite grains that can be singular or amalgamated into larger clusters that act as a cement between the quartz-filled Tasmanites cysts. Figure 61 shows the individual calcite grain and clustered calcite grain morphologies with increasingly higher magnification BSE images taken from within a calcite lamination.

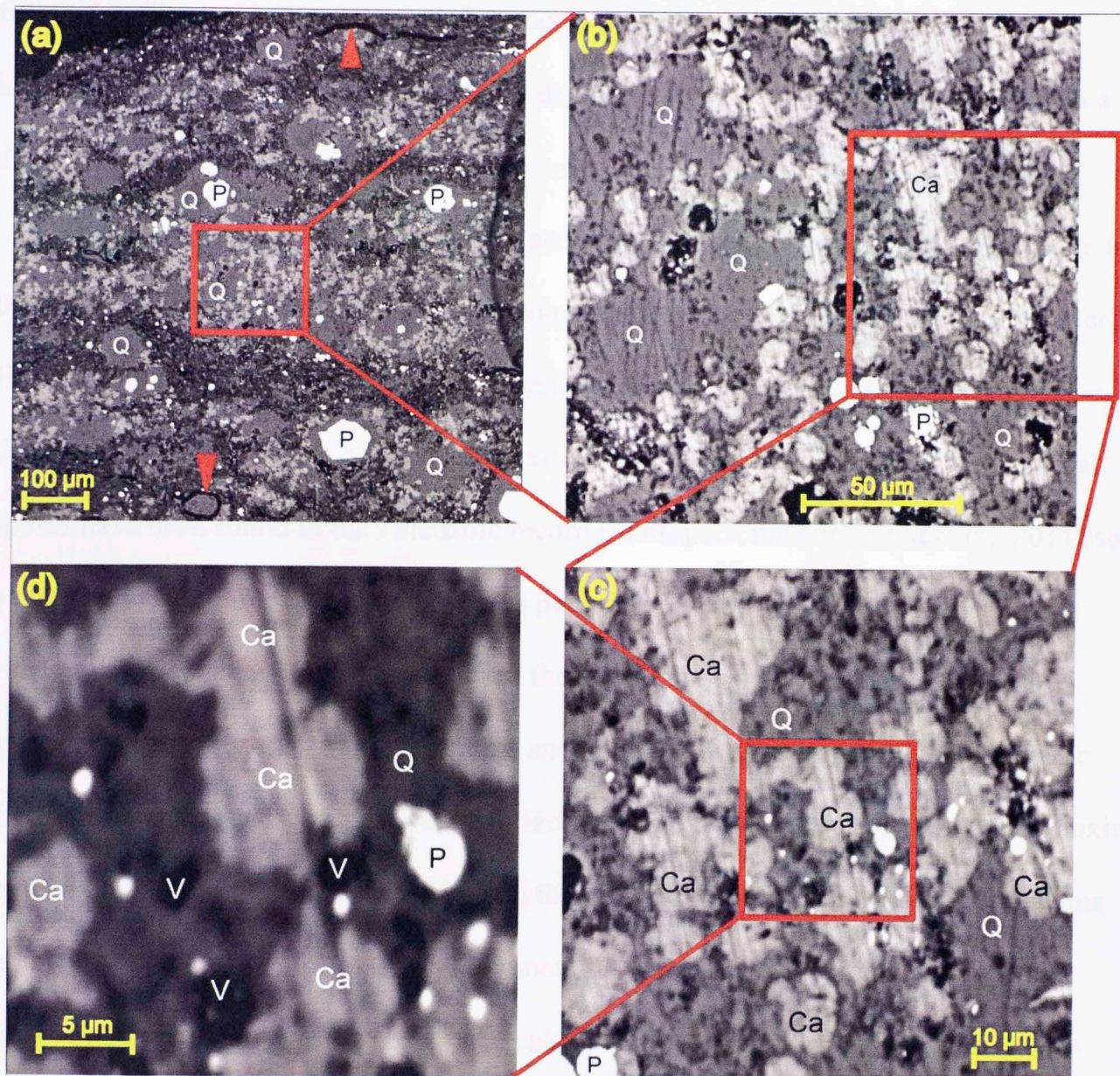


Figure 61. Increasingly higher magnification BSE images within a calcite lamination in the Wyche-1, 120.9 ft, electron microprobe thin section showing the calcite grain morphology and cementation behavior of the quartz grains. P = pyrite, Q = quartz, Ca = calcite, V = void space, and the red arrows in (a) show Tasmanites cyst organic walls (not organic stringers of unknown origin).

After both photomicrograph and BSE image examination, the origin of the calcite is still unclear, but due to the dominant spherical morphologies of the grains and their affinity for the quartz-filled remains of Tasmanites cysts, I suggest that they are calcareous algae or coral spore deposits. Figure 18a shows a relatively large calcite grain that has compacted only the center of a Tasmanites, creating an H-shaped cyst with pyrite

filling the right and left uncompacted portions. Such an observation supports a biogenically derived depositional (raining down from upper photic zones), rather than a diagenetic, origin of the calcite.

Although calcareous algal species are present in the Devonian, their abundance in the Paleozoic era is limited and research concerning such organisms is sparse. However, Harris (2011) documented calcareous dasycladacean algae with 10 micrometer grain diameters in the Woodford Shale of the west Texas Permian basin and calcareous coral spores have been found in the Paleozoic record (Slatt, personal communication, 2011) so a planktonic origin for the calcite grains is plausible. If the calcite grains do represent either a calcareous-algal or -coral species, the laminations may record increases in organic productivity such as algal blooms and coral spore releases, or possibly oceanic mixing events that caused sensitive, water-zoned algae to become trapped in more anoxic waters. Events of this nature would lead to the deposition of these calcareous organisms in sufficient quantity to form discrete laminations. After burial, these biogenic calcite grains underwent diagenesis to become a calcite cement between the quartz-filled Tasmanites cysts.

4.2 135.7 FT DOLOMITIC SAMPLE MICRO-STRATIGRAPHY

The 135.7 ft interval is the most homogeneous interval among the three samples analyzed, although some very fine scale and subtle changes were observed with the petrographic microscope, BSE image photomontage, and the micro-mineralogy log. Silt-sized dolomite grains that are disseminated throughout the illite matrix are interpreted as

either detrital input from the subaerial exposure of older dolomite formations on the shallower-shelf during periods of Late Devonian eustatic sea-level fall (Sandburg et al., 2002) or the resedimented detritus of contemporaneously formed, shallow water dolomite from episodic, updip bottom flows (Comer, 2009). Sporadic fine-grained detrital apatite and one very coarse, wedge-shaped apatite grain (40 micrometers by 400 micrometers) were discovered (Figure 42) indicating anoxic conditions (Slatt et al., 2009). Organic components are abundant in the sample and are dominated by dark-brown to opaque organic stringers of uncertain origin. Tasmanites cysts are present, but not to the extent present in the 120.9 ft sample and are generally compacted. Radiolarian deposition and dissolution is speculated to be absent or limited in this interval, probably because silica was not available in great enough abundance to fill the cyst void spaces.

A noticeable exception in the 135.7 ft thin section is a thin, millimeter-sized lamination of quartz-filled cysts shown at the very top right portion of the digital thin section scan (Figure 26) and by photomicrograph in Figure 29. The quartz-filled cysts show no signs of preserved organic walls and exhibit dominant filling of their cores by pyrite. This thin interval of Tasmanites cysts has a diffuse lower edge with cyst abundance increasing upward, thus appearing to represent an increase in both Tasmanites cyst and radiolarian test deposition. This observation is speculated to be either a planktonic blooming event or an oceanic mixing event where lower zones of anoxic water invaded upper zones of more oxygenated water resulting in the increased death and deposition of planktonic species.

Another interesting observation in the 135.7 ft sample are quartz lenses that resemble microquartz cementation or recrystallization. Their morphologies resemble

compressed Tasmanites cysts and are speculated to be recrystallized organic cyst walls (Figure 28).

Finally, three thinly-laminated zones of increased pyrite abundance are clearly observed in petrographic micrographs (Figure 27a,c), BSE images (Figure 27b,d), the BSE image photomontage (Appendix K), and the micro-mineralogy log (Figure 54). The pyrite grains in these intervals are coarser and more euhedral in form than the typical, sub-10 micrometer pyrite framboids that are disseminated throughout the thin section. The significance of these laminations is not known.

4.3 145.3 FT DOLOMITIC SAMPLE MICRO-STRATIGRAPHY

The 145.3 ft interval is less distinctly laminated than the 120.9ft interval, but has more pronounced lamination than the 135.7 ft interval. Lamination in the 145.3 ft sample interval can be observed macroscopically in the digitally-scanned thin section image (Figure 30), the BSE image photomontage (Appendix L), as well as the micro-mineralogy log (Figure 55). The silt-sized dolomite grains that are disseminated throughout the illite-clay matrix are also interpreted as either detrital input from the subaerial exposure of older dolomite formations on the shallower-shelf during periods of Late Devonian eustatic sea-level fall (Sandburg et al., 2002) or the resedimented detritus of contemporaneously formed, shallow water dolomite from episodic, updip bottom flows (Comer, 2009). No completely-filled Tasmanites cysts were observed in the sample, although fully-compacted cysts were found in more abundance than in the 135.7 ft

interval (Figure 33c,d) with the overall organic component appearing dominated by dark-brown to opaque organic stringers of unknown origin (Figure 33a,b).

Thin laminations of detrital dolomite grains can be seen throughout the 145.3 ft sample interval (Figure 31) and likely represent cyclic influxes of increased detrital material into a quiet sea having a lack of sea floor currents and turbating organisms (Kirkland et al., 1992). As these distinct laminations are sporadic throughout the 145.3 ft sample interval, I interpret that these 2-4 grain thick laminations record a brief influx in detrital dolomite grains over time periods of a few years or less.

Pyrite in the 145.3 ft sample interval is predominantly framboidal, ranging in diameter from sub-10 micrometers up to 100 micrometers. The coarser framboids are disseminated less frequently throughout the matrix. Examples of two such coarse framboids can be seen in Figure 32a and b.

In contrast to the 135.7 ft sample, lenses of fine grains, comprised of both microcrystalline dolomite and quartz, with morphologies often resembling compressed Tasmanites cysts, are present in the 145.3 ft sample interval (Figure 62a,b). These features are interpreted as diagenetic replacements of compacted Tasmanites cyst organic walls.

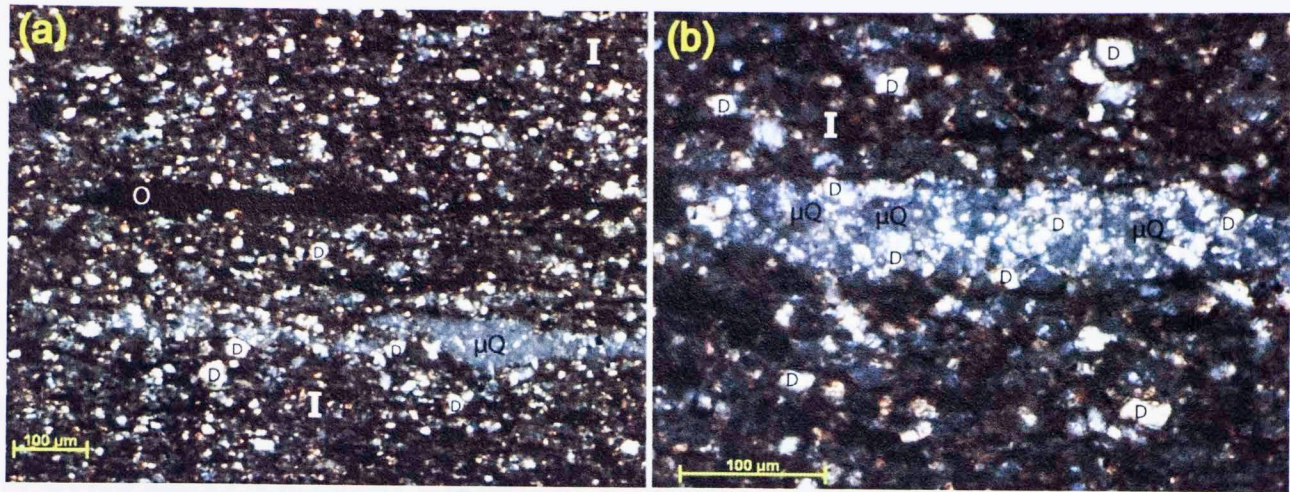


Figure 62. (a) Photomicrograph (XPL) of the 145.3 ft optical thin section showing a long, dark-brown organic lense (center) and a microquartz-dolomite mixed lense. (b) Photomicrograph (XPL) of the 145.3 ft optical thin section showing a lens of mixed microquartz and dolomite. D = dolomite, μ Q = microquartz, O = organic, and I = illite.

Finally, as compared to the other samples, the presence of apatite, while still minor, was more abundant in the 145.3 ft sample interval. Generally, these detrital apatite grains are approximately 20 to 40 micrometers in length with rectangular and wedge-like shapes. The apatite grains are speculated to be biogenic bone or scale fragments from ancient fish. Increased apatite is a probable indicator of increased euxinic conditions, which correlates to a lack of bioturbations in the 135.7 ft and 145.3 ft sample intervals (Slatt et al., 2009), however, organic productivity in the upper oxygenated zones of the water column must have been limited when compared to the 120.9 ft sample as micro-mineralogy log organic content in the dolomitic samples is significantly less even when considering the additional preservation capabilities of more anoxic bottom waters.

4.4 MICRO-MINERALOGY LOG AS AN ANALOG TO THE ECS TOOL AND BSE

IMAGE PHOTOMONTAGE AS ANALOG TO BOREHOLE IMAGING TOOLS

Service companies performing wireline logging of openhole wellbores often offer tools and interpretive software that can obtain lithology and modal mineralogy for formations of interest. For example, Schlumberger's Elemental Capture Spectroscopy (ECS) log provides the basic mineralogy of a wellbore, but with a limiting vertical resolution of 1.5 ft. With such a limitation in vertical resolution, small scale changes such as thin beds or, as is common in shale formations, millimeter to sub-millimeter laminations, will readily go unnoticed. Many industry and academic researchers opt to perform X-ray Diffraction (XRD), X-ray Fluorescence (XRF), or Fourier Transform Infrared Spectroscopy (FTIR) analyses from recovered cuttings, core, and sidewall core samples to obtain mineralogy, however, these techniques require the samples be ground into powders and often have detection limits as high as ten percent for a single mineral phase (Morgan, personal communication, 2010). Thus, the precision of such results is questionable and results from sister samples often show a range of values (Sierra, personal communication, 2010).

The electron microprobe WDS micro-mineralogy log method presented in this thesis offers an alternative technique that can substantially increase the vertical resolution, precision, and accuracy of cutting, core, and sidewall core sample mineralogy while preserving the in-situ fabric of the sample for further petrographic and SEM imaging. In this way, the micro-mineralogy log becomes an analog to a high-resolution ECS tool and the BSE image photomontage, acquired with the WDS analytical transect, acts as a high-resolution analog to lower vertical resolution borehole imaging tools. Figure 63 offers a

side-by-side comparison of Wyche-1 well ECS and FMI log excerpts, from 117 ft (35.66 m) to 150 ft (45.72 m), as well as blow-ups of the micro-mineralogy logs performed in this thesis, pointing to their respective sample locations in the FMI log. This comparison illustrates the vast difference in scales between wireline logging resolutions and that of the micro-mineralogy log results acquired with an electron microprobe.



Figure 63. Side-by-side comparison of scales between the ECS, FMI, and micro-mineralogy logs.

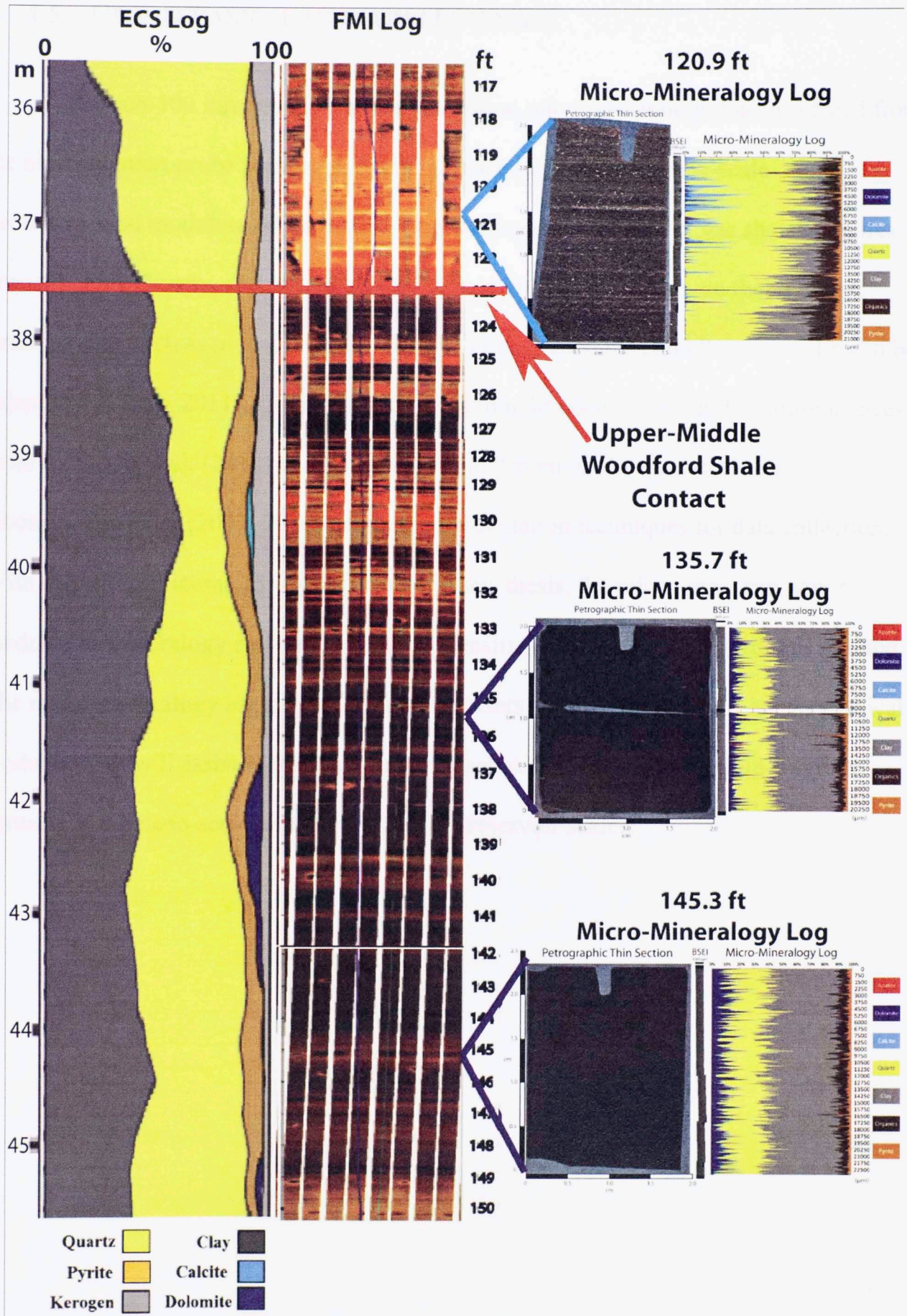


Figure 63. Side-by-side comparison of scales between the ECS, FMI, and micro-mineralogy logs.

4.5 GEOMECHANICAL MODELING POTENTIAL

The sub-100 micrometer vertical resolution micro-mineralogy logs produced from the electron microprobe present an exciting new potential for the fine-scale geomechanical modeling of gas shales. Geomechanical modeling of gas shales requires porosity, bulk density, and mineralogy of a shale interval be known, so that dynamic stress moduli such as p- and s-wave velocity, Youngs modulus, and Poissons ratio can be calculated (Sierra, 2011). Geomechanical modeling has been done on the parasequence-scale by Sierra et al. (2010) and Sierra (2011) and even on the nano-scale by Abousleiman et al. (2009; 2010) using nano-indentation techniques for data collection. With the micro-mineralogy logs presented in this thesis, the micro-scale can now be modeled as mineralogy and calculated bulk densities can be generated with this method. The micro-mineralogy log method ultimately offers yet another scale for geomechanical modeling that will assist in the upscaling of reservoir properties from grain-to-grain contacts at the nano-scale all the way to shale-reservoir scales.

5. CONCLUSIONS

- Using three samples from the Wyche-1, Woodford Shale, behind outcrop/quarry core as proof of concept examples, this study demonstrated that the electron microprobe can be used to generate high vertical resolution (sub-100 micrometers) micro-mineralogy logs to be used for micro-stratigraphic analysis and potentially for geomechanical modeling.
- Overlapping BSE images that are spliced together with automated photo-stitching software can be used in conjunction with the quantitative WDS analytical transects and qualitative photomicrographs to further enhance micro-stratigraphic interpretations.
- The presence of compacted, partially-filled, and completely-filled palynomorphs such as Tasmanites algal cysts are potential indicators for: (1) relative rates of deposition, (2) relative timing between the formation of diagenetic quartz and pyrite in Tasmanites cysts, (3) the presence of biogenic silica deposition from species such as radiolarians that would normally dissolve and leave no record in a shale matrix, and (4) deposition of palynomorphs due to oceanic mixing events of lower anoxic water zones and upper oxygenated water zones.
- Micro-mineralogy logs can be used on core and cutting samples to resolve mineralogical differences between individual laminations. Micro-mineralogy logs are analogous to ECS logs run in boreholes that are limited to resolving mineralogical differences of thicker strata.

- Micro-mineralogy logs offer more precise and higher resolution mineralogies than bulk-rock methods such as XRD and XRF.
- Semi-quantitative BSE image photomontages that are acquired in conjunction with micro-mineralogy logs act as high vertical resolution image logs that differentiate between laminations. BSE image photomontages are analogous to various borehole image logs that are limited to resolving differences between beds and formation units.
- Acquire sample conductivity measurements from the electron microprobe when performing WDS analytical transect lines for later comparison to FMI resistivity logs when available.
- Use available total organic carbon (TOC) values to quality control organic content estimates from micro-mineralogic logging on corresponding sample intervals.
- Using image analysis software, threshold BSE gray-scale images in order to estimate organic content percentages. Organics appear as black pixels in BSE images. BSE image derived organic content estimates can be used to quality control micro-mineralogic log derived organic content estimates.
- Incorporate the micro-mineralogic logging method into standard laboratory analysis suites for cores, sidewall cores, and cuttings from gas shale boreholes.

6. RECOMMENDATIONS FOR FUTURE WORK

- Perform geomechanical modeling using mineralogy acquired from micro-mineralogic logging for comparison to geomechanical experimental results carried out on corresponding core sample intervals.
- Perform micro-mineralogic logging along entire core or select core intervals to develop micro-sequence stratigraphic frameworks.
- Acquire sample conductivity measurements from the electron microprobe when performing WDS analytical transect lines for later comparison to FMI resistivity logs when available.
- Use available total organic carbon (TOC) values to quality control organic content estimates from micro-mineralogic logging on corresponding sample intervals.
- Using image analysis software, threshold BSE gray-scale images in order to estimate organic content percentages. Organics appear as black pixels in BSE images. These BSE image derived organic content estimates can be used to quality control micro-mineralogy log derived organic content estimates.
- Incorporate the micro-mineralogic logging method into standard laboratory analysis suites for cores, sidewall cores, and cuttings from gas shale boreholes.

REFERENCES

- Abousleiman, Y. N., Tran, M., Hoang, S., Ortega, A., and Ulm, F. (2009) GeoMechanics Field Characterization of the Two Prolific U.S. Mid-West Gas Plays with Advanced Wire-Line Logging Tools. *SPE Annual Technical Conference*. SPE 124428. New Orleans, LA: Society of Petroleum Engineers.
- Abousleiman, Y. N., Tran, M., Hoang, S., Ortega, A., and Ulm, F. (2010) Geomechanics Field Characterization of Woodford Shale and Barnett Shale with Advanced Logging Tools and Nano-Indentation on Drilling Cuttings. *The Leading Edge*, 29, p.730-736.
- Blakey, R. (2011). *Paleogeography and Geologic Evolution of North America*. <http://jan.ucc.nau.edu>. Accessed May, 2011.
- Cardott, B. J. (2007) *Overview of Woodford Gas-Shale Play in Oklahoma*. Woodford Gas Shale Conference, May 23, 2007. Oklahoma Geological Survey. <http://www.ogs.ou.edu/pdf/WoodfordOverview.pdf>, accessed May 18, 2011.
- Cardott, B. J. (2009) *Woodford Gas-Shale Plays of Oklahoma*. Louisiana Oil and Gas Symposium, May 20, 2009. Oklahoma Geological Survey. <http://www.ogs.ou.edu/fossilfuels/pdf/LAoilgas2009.pdf>; accessed on May 29, 2011.
- Comer, J. B. (1992) Organic Geochemistry and Paleogeography of Upper Devonian Formations in Oklahoma and Northwestern Arkansas. In Johnson and Cardott (eds.) Source Rocks in the Southern Midcontinent, 1990 Symposium. *Oklahoma Geological Survey Circular* 93, 70-93.

- Comer, J. B. (2005) Facies Distributions and Hydrocarbon Production Potential of Woodford Shale in the Southern Midcontinent. In Cardott (ed.) Unconventional Energy Resources in the Southern Midcontinent, 2004 Symposium. *Oklahoma Geological Survey Circular* 110, 51-62.
- Comer, J. B. (2008a) Reservoir Characteristics and Production Potential of the Woodford Shale. *World Oil* **229**(8).
- Comer, J. B. (2008b) *Woodford Shale in Southern Midcontinent, USA - Transgressive System Tract Marine Source Rocks on an Arid Passive Continental Margin with Persistent Ocean Upwelling*. American Association of Petroleum Geologists Annual Convention, San Antonio, Texas. Poster presentation, in pdf.
- Comer, J. B. (2009) The Forms of quartz and Dolomite in Woodford Shale of the Southern Midcontinent, USA: Indicators of Paleoclimate, Paleogeography, Paleooceanography, and Depositional Processes. AAPG 2009 Mid-Continent Section Meeting Abstract , Tulsa, Oklahoma.
- Deer, W. A., Howie, R. A., and Zussman, J. (1985) An Introduction to the Rock Forming Minerals. 15th Impression. Longman Group Limited. England.
- Energy Information Administration (EIA) (2011a) Shale Gas is a Global Phenomenon. *Today in Energy*, <http://www.eia.gov/todayinenergy/detail.cfm?id=811>, accessed May 30, 2011.
- Energy Information Administration (EIA) (2011b) *Lower 48 States Shale Gas Plays*. http://www.eia.gov/oil_gas/rpd/shale_gas.pdf, accessed May 30, 2011.
- Goldstein, J. I., Newbury, D. E., Echlin, P., Joy, D. C., Roming, Jr., A.D., Lyman, C. E., Fiori, C., and Lifshin, E. (1992) Scanning Electron Microscopy and X-Ray

- Microanalysis: *A Text for Biologists, Materials Scientists, and Geologists*. 2nd Edition. Plenum Press. New York, USA.
- Harris, N. B., Hemmesch, N. T., Mnich, C. A., Khodir, A., and Miskimins, J. (2011) Why Stratigraphy and Sedimentology in Shales are Important: An Example from the Woodford Shale, Permian Basin, West Texas. PowerPoint presentation. <http://www.empr.gov.bc.ca/OG/oilandgas/petroleumgeology/UnconventionalGas/Documents/N%20Harris.pdf>; accessed June 13, 2011.
- Hass, W. H. and Huddle, J. W. (1965) Late Devonian and Early Mississippian age of the Woodford Shale in Oklahoma, as Determined by Conodonts. *U.S. Geological Survey Professional Paper 525-D*, 125-132.
- Hover, V. C., Peacor, D. R., and Walter, L. M. (1996) Relationship Between Organic Matter and Authigenic Illite/Smectite in Devonian Black Shales, Michigan and Illinois Basins, USA. Society for Sedimentary Geology (SEPM), Special Publication 55, p. 73-83.
- Johnson, K. S. and Cardott, B. J. (1992) Geologic Framework and Hydrocarbon Source Rocks of Oklahoma. In Johnson and Cardott (eds.) Source Rocks in the Southern Midcontinent, 1990 symposium. *Oklahoma Geological Survey Circular 93*, 21-37.
- Johnson, K. S., Amsden, T. W., Denison, R. E., Dutton, S. P., Goldstein, A. G., Rascoe Jr., B., Sutherland, P. K., and Thompson, C. M. (1989) Geology of the Southern Midcontinent. *Oklahoma Geological Survey Special Publication 89-2*, 1-53.
- Kirkland, D. W., Denison, R. E., Summers, D. M., and Gormly, J. R. (1992) Geology and Organic Geochemistry of the Woodford Shale in the Criner Hills and Western Arbuckle Mountains, Oklahoma. In Johnson and Cardott (eds.) Source Rocks in

- the Southern Midcontinent, 1990 symposium. *Oklahoma Geological Survey Circular* 93, 38-69.
- Krinsley, D. H., Pye, K., Boggs Jr., S., and Tovey, N. K. (1998) Backscattered Scanning Electron Microscopy and Image Analysis of Sediments and Sedimentary Rocks. Cambridge University Press. New York, USA.
- Lambert, M. W. (1993) Internal Stratigraphy and Organic Facies of the Devonian-Mississippian Chattanooga (Woodford) Shale in Oklahoma and Kansas. In Katz and Pratt (eds.) Source Rocks in a Sequence Stratigraphic Framework. *American Association of Petroleum Geologists Studies in Geology* 37, 163-176.
- Machel, H. G. (2001) Bacterial and Thermochemical Sulfate Reduction in Diagenetic Settings - Old and New Insights. *Sedimentary Geology* 140, p. 143-175.
- Miceli, A. (2010) *Geochemical Characterization of the Woodford Shale, Central and Southeastern Oklahoma*. Master of Science Thesis, The University of Oklahoma, pp. 134.
- Morgan, G. (2010) personal communication.
- O'Brien, N. R. and Slatt, R. M. (1990) Argillaceous Rock Atlas. Springer-Verlag New York Inc. New York, USA.
- Perry, W. J. (1995) USGS 1995 National Oil and Gas Assessment - Arkoma Basin Province. United States Geological Survey 62.
- Portas, R. (2009) *Characterization and Origin of Fracture Patterns in the Woodford Shale in Southeastern Oklahoma for Application to Exploration and Development*. Master of Science Thesis, The University of Oklahoma, pp. 110.

- Potter, P. E., Maynard, J. B., Pryor, W. A. (1980) *Sedimentology of Shale: Study Guide and Reference Source*. Springer-Verlag. New York, USA.
- Reed, S. J. B. (2005) *Electron Microprobe Analysis and Scanning Electron Microscopy in Geology*. 2nd Edition. Cambridge University Press. New York, USA.
- Sandburg, C. A., Morrow, J. R., and Ziegler, W. (2002) Late Devonian Sea-Level Changes, Catastrophic Events and Mass Extinctions: Impacts and Beyond. *Geological Society of America Special Paper* 356, 473-487.
- Schieber, J. (1996) Early Diagenetic Silica Deposition in Algal Cysts and Spores: A Source of Sand in Black Shales? *Journal of Sedimentary Research*, **66**(1), p. 175-183.
- Schieber, J. and Baird, G. (2001) On the Significance of Pyrite Spheres in Devonian Black Shales of North America. *Journal of Sedimentary Research*, **71**(1), p. 155-166.
- Schlumberger (2000) Elemental Capture Spectroscopy Sonde. Chapter from Schlumberger text: 4.4 Evaluation Services - Integrated Platform. Courtesy of Bob Davis, Schlumberger Limited.
- Schwartzapfel, J. A. and Holdsworth, B. K. (1996) Upper Devonian and Mississippian Radiolarian Zonation and Biostratigraphy of the Woodford, Sycamore, Caney, and Goddard Formations, Oklahoma. *Cushman Foundation for Foraminiferal Research Special Publication* **33**, pp. 275.
- Sierra, R. (2010) Personal communication.

- Sierra, R. (2011) *Integrated Geomechanics and Geological Characterization of the Devonian-Mississippian Woodford Shale*. Master of Science Thesis, The University of Oklahoma, pp. 110.
- Sierra, R., Tran, M. H., Abousleiman, Y. N., and Slatt, R. M. (2010) Woodford Shale Mechanical Properties and the Impacts of Lithofacies. *American Rock Mechanics Association* 10-461.
- Slatt, R. M. (2011) personal communication.
- Slatt, R. M., Buckner, N., Abousleiman, Y., Sierra, R., Philp, P., Miceli-Romero, A., Portas, R., O'Brien, N., Tran, M., Davis, R., and Wawrzyniec, T. (2010) Outcrop/Behind Outcrop (Quarry), Multiscale Characterization of the Woodford Gas Shale, Oklahoma, in Breyer ed., *Shale Reservoirs—Giant Resources for the 21st century*, AAPG Memoir 97, p. 1-21.
- Slatt, R. M., Singh, P., Philp, R. P., Marfurt, K. J., Abousleiman, Y., O'Brien, N. R., Eslinger, E. V. (2009) Workflow for Stratigraphic Characterization of Unconventional Gas Shales: *Gulf Coast Association of Geological Societies Transactions*, **59**, p. 699-710.
- Tappan, H. (1980) *The Paleobiology of Plant Protists*. W.H. Freeman and Company. San Francisco, USA. pp. 1028.
- Urban, J. B. (1960) *Microfossils of the Woodford Shale (Devonian) of Oklahoma*. Master of Science Thesis, The University of Oklahoma, pp. 77.
- Vardilos, G. (2010) personal communication.

Von Almen, W. F. (1970) *Palynomorphs of the Woodford Shale of South Central Oklahoma with Observations on their Significance in Zonation and Paleocology*. Doctor of Philosophy Dissertation, Michigan State University, pp. 222.

Webster, R. E. (1977) Evolution of a Major Petroleum Province: The Southern Oklahoma Aulacogen. *Compass*, **54**(3), 59-71.

Wickstrom, C. W. (2008) *Woodford Shale Gas in Oklahoma*. AAPG Annual Convention, San Antonio, Texas, April 20-23, 2008. Spyglass Energy Group, LLC, Tulsa, Oklahoma.

APPENDICES ON DIGITAL MEDIA

APPENDIX A	120.9 FT SAMPLE WDS WEIGHT PERCENT ELEMENT RESULT
APPENDIX B	120.9 FT SAMPLE WDS WEIGHT PERCENT OXIDE RESULT
APPENDIX C	120.9 FT SAMPLE WDS CALCULATED MINERALOGIC FRACTIONATION
APPENDIX D	135.7 FT SAMPLE WDS WEIGHT PERCENT ELEMENT RESULT
APPENDIX E	135.7 FT SAMPLE WDS WEIGHT PERCENT OXIDE RESULT
APPENDIX F	135.7 FT SAMPLE WDS CALCULATED MINERALOGIC FRACTIONATION
APPENDIX G	145.3 FT SAMPLE WDS WEIGHT PERCENT ELEMENT RESULT
APPENDIX H	145.3 FT SAMPLE WDS WEIGHT PERCENT OXIDE RESULT
APPENDIX I	145.3 FT SAMPLE WDS CALCULATED MINERALOGIC FRACTIONATION
APPENDIX J	120.9 FT BSE IMAGE PHOTOMONTAGE
APPENDIX K	135.7 FT BSE IMAGE PHOTOMONTAGE
APPENDIX L	145.3 FT BSE IMAGE PHOTOMONTAGE



APPENDIX M 120.9 FT HIGH-RESOLUTION DIGITAL THIN SECTION SCAN

APPENDIX N 135.7 FT HIGH-RESOLUTION DIGITAL THIN SECTION SCAN

APPENDIX O 145.3 FT HIGH-RESOLUTION DIGITAL THIN SECTION SCAN

This volume is the property of the University of Oklahoma, but the literary rights of the author are a separate property and must be respected. Passages must not be copied or closely paraphrased without the previous written consent of the author. If the reader obtains any assistance from this volume, he must give proper credit in his own work.

I grant the University of Oklahoma Libraries permission to make a copy of my thesis upon the request of individuals or libraries. This permission is granted with the understanding that a copy will be provided for research purposes only, and that requestors will be informed of these restrictions.

NAME _____

DATE _____

A library which borrows this thesis for use by its patrons is expected to secure the signature of each user.

This thesis by MATTHEW W. TOTTEN JR. has been used by the following persons, whose signatures attest their acceptance of the above restrictions.

NAME AND ADDRESS

DATE